Max-Planck-Institut
für Mathematik
in den Naturwissenschaften
Leipzig

Recent analytical developments in micromagnetics

(revised version: August 2005)

by

Antonio DeSimone, Robert V. Kohn, Stefan Müller, and Felix Otto

Preprint no.: 80 2004

Recent analytical developments in micromagnetics

Antonio DeSimone[*], Robert V. Kohn[†], Stefan Müller[‡], Felix Otto[§]

October 25, 2004

Contents

---

[*] SISSA-International School for Advanced Studies, Trieste, Italy, desimone@sissa.it

[†] Courant Institute of Mathematical Sciences, New York University, USA, kohn@cims.nyu.edu

[‡] Max–Planck–Institut für Mathematik in den Naturwissenschaften, Leipzig, Germany, sm@mis.mpg.de

[§] Institut für Angewandte Mathematik, Universität Bonn, Germany, otto@iam.uni-bonn.de

1 Introduction

Micromagnetics is a strikingly simple and remarkably powerful theory. At its core is the micromagnetic energy, whose local minima represent the stable magnetization patterns of a ferromagnetic body. This theory is now routinely used for the analysis and design of magnetic devices. It explains observations on many length scales, from nanometers to microns. It also explains magnetic hysteresis, through the multiplicity of local minima.

Micromagnetics has mainly been applied in two alternative ways. Before the advent of computing, analytical solutions were obtained by minimizing the energy over a suitable class of trial fields; a classic example is the Stoner-Wohlfarth theory of magnetic switching [108]. Since the advent of computing, micromagnetics has mainly been applied numerically. Simulation has been very successful, giving detailed information about pattern formation and hysteresis in samples up to about a micron in size.

Both these approaches have limitations. When we minimize the energy over a restricted class of magnetizations, the answer is limited by the correctness of the ansatz. Many analytical solutions are now known to be wrong (though still informative), because the true solution – observed numerically and/or experimentally – does not match the ansatz. For example, the Stoner-Wohlfarth theory matches experiment only for the smallest nanoscale particles. Numerical simulation is free from this difficulty; it is, in fact, the ideal tool for answering specific questions about submicron-scale phenomena. However we seek *understanding* as well as answers. For example, why do we see boundary vortices but not interior vortices at some length scales? And what determines the familiar pattern of a cross-tie wall? Simulation alone cannot answer such questions. Moreover simulation is limited to relatively small ferromagnets. Owing to the presence of small length scales (domain walls, Bloch lines) and the nonlocal character of the energy (dipolar interaction), fully-resolved computations are limited – even using the most powerful computers – to dimensions on the order of a few microns or less.

Thus the understanding and utilization of micromagnetics has remained a challenge. Recently two new approaches have begun to emerge:

(a) identifying the scaling law of the minimum energy, and the character of magnetization patterns that achieve it; and

(b) identifying simpler models, valid in appropriate regimes, whose behavior is easier to understand or simulate.

This review article provides an introduction to these new methods, and a survey of the insight they provide.

The new approaches are both based on asymptotic analysis. They take advantage of the presence of small nondimensional ratios, for example exchange length or film thickness divided by diameter. The asymptotic analysis assumes that some or all of these ratios tend to zero, with specified relations between them. The existence of more than one nondimensional parameter makes the problem rich, since there are several distinct regimes. By identifying and exploring them we obtain a sort of "phase diagram."

The new approaches are mathematically rigorous. To identify the scaling law of the minimum energy one must prove matching upper and lower bounds. The upper bound is usually familiar – obtained by the classical method of minimizing the energy over a suitable class of trial fields. The lower bound, however, is usually unfamiliar. By proving an ansatz-independent lower bound that matches an ansatz-dependent upper bound, we effectively prove the correctness (or at least the adequacy) of the ansatz. In some settings we get the energy scaling law but not the optimal prefactor. In other settings we identify the prefactor as well, as the minimum value of a suitable "asymptotic problem."

Some readers may wonder how one can ever hope to prove an ansatz-independent bound. For convex variational problems the answer is familiar: every test field for the dual problem gives a lower bound. For nonconvex problems there is no such universal tool. Most of our examples use the presence of a small parameter and draw from the theory of Γ-convergence.

The goal of analysis is not to avoid simulation, but to maximize its utility. This is especially clear in Section 5, where the focus is on relatively large thin films. Fully-resolved simulations are simply not possible in this regime. Our asymptotic problem, on the other hand, is accessible numerically. It uniquely determines the magnetic charge. Moreover, there is a naturally associated domain structure, which appears to be the ground state.

The achievements surveyed in this article include:

(1) *A systematic analysis of soft thin films* (Section 4). We identify five distinct regimes corresponding to different relationships between the thickness, diameter, and Bloch line width. For each regime we identify an asymptotic variational problem. Its solution determines the ground-state magnetization pattern, and the leading–order behavior of the energy. This topic encompasses work by Gioia & James [56], Moser [94, 95], and Kohn & Slastikov [80].

(2) *Nonhysteretic behavior in large thin films* (Section 5). For relatively

large thin films, which have many local minima and plenty of hysteresis, our asymptotic variational problem is degenerate but convex. As a result it determines certain quantities – in particular the magnetic charge and the region of field penetration – uniquely. We conclude that although a large thin film has many stable magnetization patterns and lots of hysteresis, some quantities (namely, those determined by the asymptotic problem) should be free of hysteresis. This topic encompasses our recent papers [38, 40, 41].

(3) *The internal structure of a cross-tie wall* (Section 6.5). The cross-tie wall is a special type of domain wall seen in thin films. It is interesting due to its non-one–dimensional character, involving a periodic arrangement of vortices. The recent work of Alouges, Rivière, and Serfaty [7] uses matching upper and lower bounds to give the first analytical explanation of its structure.

(4) *The internal structure and stability of a Néel wall* (Sections 6.2, 6.3, 6.4, and 6.6). The one–dimensional Néel wall, seen in extremely thin films, is interesting due to its core-and-tail structure. Dipolar effects play a major role, so the variational problem for the wall profile is strongly nonlocal. The recent work of Melcher [89, 90] uses matching upper and lower bounds to identify the structure of the tail. The energy of a one–dimensional Néel wall is greater than that of a cross-tie wall, so it must be a local not global minimum; the recent work of DeSimone, Knüpfer, and Otto [42] explains why. In thicker films the asymmetric Bloch wall has lower energy, and [98] proves that no other structure can do significantly better.

(5) *Nucleation of domain structure in a soft thin strip* (Section 8.1). Under a sufficiently large applied field the magnetization of a strip is saturated and unique. As the applied field is reduced, the magnetization remains in a local minimum until one reaches the critical field, where an instability (bifurcation) occurs. The outcome of this instability is the formation of magnetic domains. Until recently, the spatial structure of the instability was thought to be limited to coherent rotation, curling, or smooth buckling. New work by Cantero-Álvarez and Otto [20, 21, 22] has shown the existence of a fourth alternative – “oscillatory buckling” – which is probably the origin of the “concertina” domain structure. This development demonstrates the value of seeking lower as well as upper bounds: the proof of the lower bound may point to existence of a previously-unnoticed regime.

Micromagnetics was first formulated as a model over 60 years ago, but it remains in its infancy mathematically. The associated challenges are of course opportunities. In some areas, the recent analytical progress has taken advantage of apparently unrelated mathematical developments, for example the theory of Landau-Ginzburg vortices and the framework of Γ-convergence. In other areas micromagnetics is driving the development of entirely new methods – for example techniques for proving ansatz-independent lower bounds.

As the reader has probably noticed by now, our story is coherent but not very orderly – and certainly not finished. The goal of this paper is not to review all of micromagnetics, but rather to give an overview of our recent work. We have included some closely related topics, including in Section 7 a fairly extensive survey of related mathematical tools and results. However we have omitted many important topics – for example Landau-Lifshitz-Gilbert dynamics – and we have barely scratched the surface concerning thermally-activated switching. For some recent progress in these areas see [74, 78, 79, 87].

The paper begins, in Sections 2 and 3, with a brief introduction to micromagnetics and a discussion of the small-particle and large-body limits. Section 4 identifies five distinct thin-film regimes, discussing for each the form of the limiting energy and what it tells us about the associated magnetization. Section 5 discusses one of those regimes – corresponding to relatively large thin films – in greater depth. Section 6 assembles various results on domain wall structures in thin films. Section 7 discusses some related mathematical problems, drawing connections with micromagnetics and setting our work in its natural mathematical context. All the preceding sections address local or global energy minimization. Section 8 is different: it addresses the nucleation of domain structure, and the relevance of saddle points for thermally-activated switching.

2 The energy functional and pattern formation

In this section we briefly describe the energy functional of micromagnetics, thereby introducing also the notation used in the rest of this article. We will mostly use the partially non-dimensionalized form (2.17) in which the energy functional has units of volume and the important material parameters are the non-dimensional quality factor Q and the Bloch-line-width d, which has dimensions of length. In the last subsection we discuss briefly how the competition of the different terms in the energy leads to the formation of the complex magnetization patterns observed in experiment.

2.1 Formulation in S.I. units

The energy functional of micromagnetics is given, in S.I. units, by the following expression:

$$\mathbb{E}(J) = \int_\Omega A|\nabla m|^2 + \int_\Omega K_a \varphi(m) + \frac{\mu_0}{2}\int_{\mathbb{R}^3} |\mathbb{H}_{ind}|^2 - \int_\Omega \mathbb{H}_{ext}\cdot J. \tag{2.1}$$

Here $\Omega \subset \mathbb{R}^3$ is the region of space occupied by a ferromagnetic body and J is the magnetization density i.e., a vector field of constant length inside Ω, and extended by zero to $\mathbb{R}^3$

$$|J(x)| = \begin{cases} J_s & \text{in } \Omega, \\ 0 & \text{in } \mathbb{R}^3\setminus\Omega. \end{cases} \tag{2.2}$$

The positive scalar J_s is called saturation magnetization. At fixed temperature, it is a material constant so that the (rescaled) magnetization

$$m := \frac{J}{J_s} \tag{2.3}$$

satisfies

$$|m(x)| = \begin{cases} 1 & \text{in } \Omega, \\ 0 & \text{in } \mathbb{R}^3\setminus\Omega. \end{cases} \tag{2.4}$$

The four summands in (2.1) are called exchange energy, anisotropy energy, magnetostatic (or demagnetizing or stray field) energy, Zeeman energy (or external field energy), respectively.

The vector field $\mathbb{H}_{ext}$ is an applied magnetic field, the constant μ_0 is the magnetic permeability of vacuum while $\mathbb{H}_{ind}$ is the magnetic field generated by the magnetized body Ω (also called induced, or demagnetizing, or stray field). This is obtained from J by solving Maxwell's equations of magnetostatics

$$\begin{cases} \text{curl } \mathbb{H}_{ind} = 0, \\ \text{div}(\mu_0 \mathbb{H}_{ind} + J) = 0, \end{cases} \quad \text{in } \mathbb{R}^3. \tag{2.5}$$

¿From $(2.5)_1$ we deduce the existence of a scalar potential $\mathbb{U}$ for $\mathbb{H}_{ind}$

$$\mathbb{H}_{ind} = -\nabla \mathbb{U}, \tag{2.6}$$

which, in view of $(2.5)_2$ satisfies

$$\Delta \mathbb{U} = \text{div}\, \frac{J}{\mu_0}. \tag{2.7}$$

The last two identities can be summarized by

$$\mathbb{H}_{ind} = -\nabla \left(\Delta^{-1} \text{div}\, \frac{J}{\mu_0} \right), \tag{2.8}$$

which shows that $\text{div}\, J$ is the source of $\mathbb{H}_{ind}$, and hence the magnetostatic energy is minimized by divergence-free magnetization patterns. Since $(2.5)_2$ holds in the sense of distributions

$$\int_{\mathbb{R}^3} \mathbb{H}_{ind} \cdot \nabla \varphi = -\int_{\Omega} J \cdot \nabla \varphi, \quad \forall \varphi \in C_0^{\infty}(\mathbb{R}^3), \tag{2.9}$$

the divergence of J may consist of two components which, by the electrostatic analogy, are called volume charges and surface charges. For a smooth J their densities are given, respectively, by $\text{div}\, J$ (at points of Ω) and $-J \cdot \nu$ (at a point of the boundary $\partial\Omega$ of Ω where the outer unit normal is ν). For a discontinuous J, a similar surface contribution arises also at all surfaces of discontinuity inside Ω across which the flux $J \cdot \nu$ of J is discontinuous. Thus, magnetization fields with vanishing magnetostatic energy describe domain patterns that achieve flux closure.

The positive scalars A and K_a in (2.1) are material parameters which we will assume to be constant, for simplicity. They are called the exchange constant and the (magnetocrystalline) anisotropy constant. The energy density φ is a non-negative function called the anisotropy energy density. It is typically a polynomial, with the symmetry properties inherited from those of the underlying crystalline lattice. The zeroes of φ form the set of preferred directions of magnetization (easy axes).

$$\mathcal{K} := \varphi^{-1}(\{0\}) \tag{2.10}$$

For a uniaxial material (the typical example we will use in our discussion), there exists a distinguished axis identified through a unit vector e, and φ and $\mathcal{K}$ are given respectively by

$$\varphi_{uni}(m) = 1 - (m \cdot e)^2 \tag{2.11}$$

$$\mathcal{K}_{uni} = \{+e, -e\} \tag{2.12}$$

Other expressions are of course possible, either for uniaxial materials (case of an easy plane, higher order polynomials, etc.) or for materials with a different crystallographic symmetry, but we do not need to discuss them in detail.

According to micromagnetics, stable magnetization patterns on a body Ω are described by minimizers (global or local) of the energy functional (2.1). This is a nonconvex nonlocal variational problem in view of the nonconvex pointwise constraint $|J| = J_s$ in Ω and of the nonlocal differential constraint linking $\mathbb{H}_{ind}$ with J.

2.2 Non-dimensional formulations and material parameters

In our developments, we will focus on partially or fully nondimensional versions of (2.1). For example, let

$$K_d = \frac{J_s^2}{2\mu_0} \tag{2.13}$$

and define

$$E(m) := \frac{\mathbb{E}(J)}{K_d}. \tag{2.14}$$

Setting

$$H_{ext} = \frac{\mu_0 \mathbb{H}_{ext}}{J_s}, \quad U = \frac{\mu_0 \mathbb{U}}{J_s} \tag{2.15}$$

$$H_{ind} = \frac{\mu_0 \mathbb{H}_{ind}}{J_s} = -\nabla U = -\nabla(\Delta^{-1} \operatorname{div} \ m) \tag{2.16}$$

we obtain

$$E(m) = d^2 \int_\Omega |\nabla m|^2 + Q \int_\Omega \varphi(m) + \int_{\mathbb{R}^3} |\nabla U|^2 - 2 \int_\Omega H_{ext} \cdot m\,. \tag{2.17}$$

This is the form of the energy functional we will use most frequently. Here the 'energy' $E(m)$ has the dimensions of volume (since K_d is an energy density). There are two important material parameters in (2.17). The so-called quality factor

$$Q = \frac{K_a}{K_d} \tag{2.18}$$

measures the strength of the anisotropy energy relative to that of the stray field. It is a nondimensional quantity, and it separates ferromagnetic materials into two broad classes: soft materials, for which $Q < 1$, and hard materials ($Q > 1$). The exchange length associated with the stray field energy

$$d = d_{BL} = \left(\frac{A}{K_d}\right)^{\frac{1}{2}} \tag{2.19}$$

measures the relative strength of the exchange and magnetostatic energies. It has dimensions of length, and it is also called Bloch line-width, and denoted with d_{BL}, for reasons that will become clear later, see (7.20).

In terms of the rescaled fields m, U, H_{ind}, equations (2.7), (2.9) are written as

$$\Delta U = \text{div} \quad m \tag{2.20}$$

or, in weak form, as

$$\int_{\mathbb{R}^3} \nabla U \cdot \nabla\varphi = -\int_{\mathbb{R}^3} H_{ind} \cdot \nabla\varphi = \int_\Omega m \cdot \nabla\varphi. \quad \forall\varphi \in C_0^\infty(\mathbb{R}^3). \tag{2.21}$$

Another interesting partial nondimensionalization of (2.1) is obtained by dividing $\mathbb{E}$ by K_a

$$I(m) := \frac{\mathbb{E}(J)}{K_a} = \frac{E(m)}{Q} \tag{2.22}$$

hence obtaining

$$I(m) = d_{BW}^2 \int_\Omega |\nabla m|^2 + \int_\Omega \varphi(m) + \frac{1}{Q}\int_{\mathbb{R}^3} |\nabla U|^2 - \frac{2}{Q}\int_\Omega H_{ext} \cdot m \tag{2.23}$$

The material parameter

$$d_{BW} = \frac{d_{BL}}{Q^{1/2}} = \left(\frac{A}{K_a}\right)^{\frac{1}{2}} \tag{2.24}$$

Material	Q	$d_{BL}(nm)$	$d_{BW}(nm)$
Permalloy	2.5×10^{-4}	5	316
α-Iron	2.5×10^{-2}	3.7	23
$SmCo_5$	38	5.2	0.8
$Ne_2Fe_{14}B$	4.9	2.7	1.2
Co	0.3	3.8	7

Table 1: Material parameter values for some common ferromagnetic materials

is the exchange length associated with the anisotropy energy. It is also called Bloch wall-width, for reasons that will become clear later, see (7.18). It has dimensions of length, and it measures the strength of the exchange energy relative to that of the anisotropy energy.

It is instructive to look at the values of the material parameters appearing in (2.17) and (2.22) for some concrete examples, see Table 1. The wide range of variability of the quality factor Q, which spans six orders of magnitude, is immediately apparent. By contrast, for the same set of materials, the exchange length d_{BL} only varies by a factor two.

2.3 Pattern selection as a result of energetic competition

Pattern selection is controlled by the interaction of the energy terms in (2.17) as a compromise among conflicting trends. The most immediate example of such conflicts is the competition between exchange and magnetostatic energies. For m constant, eq. (2.20) is written more explicitly as

$$\Delta U = -(m \cdot \nu)(x)\, d\sigma \tag{2.25}$$

where ν is the outer unit normal to the boundary $\partial\Omega$ of Ω, and $d\sigma$ is the surface measure. This shows that a constant magnetization always generates a nonzero magnetostatic energy if Ω is not an infinite cylinder with axis parallel to m. In other words, exchange energy and magnetostatic energy can never simultaneously achieve their minimal value zero. Actually, for soft materials, the competition between exchange and magnetostatic is the most fundamenental driving force behind formation of domain patterns, at least in the absence of an external field.

More generally, the features of the observed domain patterns are decided by the relative strength of all four summands in (2.1), and hence they depend on the values of the material parameters affecting them. The variability of these numbers over wide ranges explains the great variability and richness of observed configurations, see Figures 1 to 4. Essentially, understanding these patterns means understanding the interaction among the various summands in (2.1).

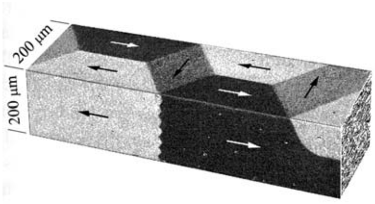

Figure 1: Iron whiskers. Reproduced with permission from Hubert and Schäfer, Magnetic Domains, Springer 1998

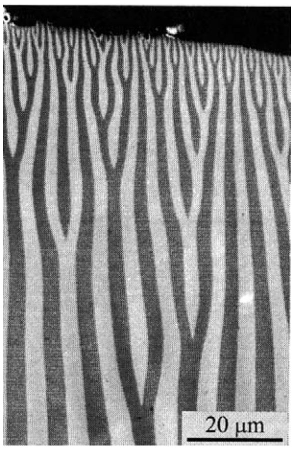

Figure 2: NdFeB domain patterns. Reproduced with permission from Hubert and Schäfer, Magnetic Domains, Springer 1998

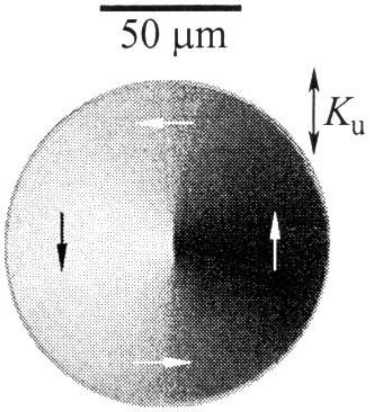

Figure 3: Permalloy film with circular cross–section. Reproduced with permission from Hubert and Schäfer, Magnetic Domains, Springer 1998

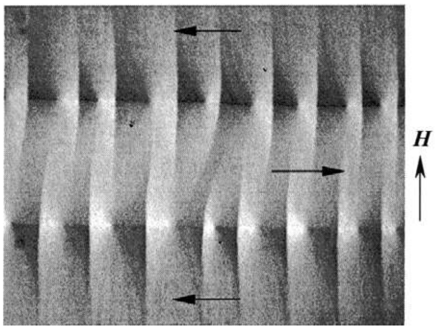

Figure 4: A cross–tie wall in a Permalloy film. Reproduced with permission from Hubert and Schäfer, Magnetic Domains, Springer 1998

3 Bulk scalings

Consider a magnetic particle of fixed shape, e.g. a cubic particle. In this section we study how the minimizers of the micromagnetic energy (2.17) depend on the size of the particle. We will see that certain models that are often thought of as alternatives to the micromagnetic approach actually arise as rigorous limits of the micromagnetic formulation. Specifically, Stoner-Wohlfarth theory corresponds to the small particle limit and Néel's theory of magnetic phases arises in the large particle limit.

The right notion of convergence is the so called Γ-convergence of the corresponding energy functionals. This notion is explained in more detail in Section 10. The main point is that Γ-convergence of the energy functionals is essentially equivalent to the convergence of the corresponding minimizing magnetizations, which are our main object of interest.

The limits above correspond to the competition of two length scales, namely a material dependent scale (such as the Bloch line-width d) and the size of the magnetic particle. In the next section we will also discuss thin magnetic films, which involve three length scales: the material scale d, the typical thickness t and the typical lateral dimension l. In order to establish a consistent notation we consider from the beginning both t and l, but in this section the aspect ratio

$$\tau = \frac{t}{l} \tag{3.1}$$

will be kept fixed, while in the later sections we will be interested in the limit $\tau \to 0$. We consider for simplicity the case that the body Ω is a prism

$$\Omega = \Omega' \times (0, t) \tag{3.2}$$

of height t and we denote by l a typical length of the base Ω'. As an example one could take a square base, i.e. $\Omega' = (0, l)^2 \times (0, t)$. For $\tau = 1$, Ω is a cubic particle of size l.

The change of variables $x \mapsto \bar{x} = \frac{x}{l} \in \omega$ rescales Ω to a set $\omega = \omega' \times (0, \tau)$, where ω' has size of order one, and it reduces the energy functional (2.17) to a fully non-dimensional form

$$e(m) = \kappa^2 \int_\omega |\nabla m|^2 + Q \int_\omega \varphi(m) + \int_{\mathbb{R}^3} |\nabla u|^2 - 2 \int_\omega h_{ext} \cdot m, \tag{3.3}$$

where

$$e(m) = \frac{1}{l^2 t}\ E(m), \tag{3.4}$$

$$\kappa = \frac{d}{l}, \tag{3.5}$$

$$u\left(\frac{x}{l}\right) = \frac{1}{l}\ U(x), \tag{3.6}$$

$$h_{ind}\left(\frac{x}{l}\right) = -\nabla_{\bar{x}} u\left(\frac{x}{l}\right) = H_{ind}(x) = -\nabla_x U(x), \tag{3.7}$$

$$h_{ext}\left(\frac{x}{l}\right) = H_{ext}(x). \tag{3.8}$$

The static Maxwell equation (2.20) for u implies that

$$\Delta u = \operatorname{div} m. \tag{3.9}$$

If we take a square base and aspect ratio $\tau = 1$ then ω is simply the unit cube. Again, for simplicity, we will restrict attention to the case of spatially uniform applied field, $H_{ext} \equiv$ const.

3.1 The small particle limit

Consider the case $l << d$, i.e., $\kappa \to +\infty$, while τ, Q are fixed numbers of order one. Also, the strength of the applied field, if present, should be of order one. In this limit, the classical model of Stoner and Wohlfarth [108] is recovered, see [35].

Proposition 3.1 *As $\kappa \to +\infty$, the functional* (3.3) Γ*-converges in* H^1 *to*

$$e_\infty(m) = \begin{cases} Q\varphi(m) + m \cdot D_\omega m - 2h_{ext} \cdot m & \text{for } m \equiv \text{ const in } \omega,\ |m| = 1, \\ +\infty & \text{else,} \end{cases} \tag{3.10}$$

where D_ω is the demagnetizing tensor of ω.

In this case the Γ-limit of the energy functionals agrees with the pointwise limit, but this is not true in general (see Section 10).

In the proposition above, the demagnetizing tensor D_ω is a traceless, positive-definite tensor depending only on the shape of ω. For ω a unit cube or a unit sphere, $D_\omega = \frac{1}{3} Id$, with Id the identity. For a more general ω, D_ω is defined implicitly by

$$D_\omega m = -\frac{1}{|\omega|} \int_\omega h_m \quad \forall m = \text{const in } \omega, \tag{3.11}$$

where $|\omega|$ is the volume of ω and h_m is the magnetic field induced by m, i.e., $h_m = -\nabla\Delta^{-1} \operatorname{div} m$.

Remark 3.2 *The functional e_∞ is defined on a finite-dimensional space. It is therefore easy to study its local minima, as was done by Stoner and Wohlfarth in their celebrated paper [108]. In fact, global and local minima of the function $m \mapsto e_\infty(m)$ characterize the asymptotic behavior of both global and local minima of e (see [35], [12]). The Stoner-Wohlfarth model is thus relevant to gain some insight onto the hysteretic behavior of very fine particles. For a recent numerical investigation of the switching fields of small cuboidal particles, and of their deviations from Stoner-Wohlfarth predictions, see [6], where a nonmonotone dependence of the switching field on particle size has also been observed.*

3.2 Large body limit

Consider now the case $l >> d$, i.e. $\kappa \to 0$, while τ, Q and h_{ext} are held fixed, at order one. In the limit, we obtain a mathematically rigorous version of a model which, for ellipsoidal specimens, coincides with the theory of magnetic phases of Néel ([34], see also [99, 111, 112]).

Proposition 3.3 *As $\kappa \to 0$, the functional* (3.3) *Γ-converges with respect to the weak convergence in L^2 to*

$$e_0 = Q \int_\omega \varphi^{**}(m) + \int_{\mathbb{R}^3} |\nabla u|^2 - 2 \int_\omega h_{ext} \cdot m, \quad |m| \leq 1 \text{ in } \omega, \tag{3.12}$$

where φ^{**} is the convex envelope of φ (extended by $+\infty$ for $|m| \neq 1$):

$$\varphi^{**}(m) = \min \left\{ \sum_{i=1}^{4} \lambda_i \varphi(m_i) \ : \ |m_i| = 1, m = \sum_{i=1}^{4} \lambda_i m_i, \lambda_i \geq 0, \sum_{i=1}^{4} \lambda_i = 1 \right\}. \tag{3.13}$$

Remark 3.4 *The notion of weak convergence appearing in the proposition above is essentially equivalent to convergence of 'local' averages on arbitrary cubes C cut out of ω:*

$$m_k \to m \text{ weakly in } L^2(\omega) \Leftrightarrow \frac{1}{|C|}\int_C m_k \to \frac{1}{|C|}\int_C m \quad \forall \text{ cubes } C \subset \omega. \tag{3.14}$$

The loss of the unit length constraint, in the limit, is thus not surprising whenever m_k is oscillating at a fine scale. This is precisely the case in *micromagnetics, because domain patterns of size smaller than l generate, when rescaled onto ω, fine-phase mixtures with characteristic rescaled size tending to zero.*

Proposition 3.3 implies that, in the large body limit, local averages of micromagnetic minimizers can be computed by minimizing (3.12). Since in computing magnetization curves the only relevant feature of a magnetic configuration is its average over the whole specimen, (3.12) can be used to compute magnetization curves in cases where the effects of hysteresis are negligible. For ω an ellipsoid, minimizers of (3.12) are spatially uniform, and minimizing (3.12),(3.13) reduces to the problem of finding a mixture of at most four magnetic phases $m_1, ..., m_4$ (with respective volume fractions $\lambda_1, ..., \lambda_4$), covering ω and carrying minimal energy. This is the approach of Néel to the prediction of virgin magnetization curves, see [34, 96, 66].

Remark 3.5 *The functional* (3.12) *is the 'relaxation' (i.e. the lower semicontinous envelope with respect to weak convergence in L^2) of the functional*

$$Q \int_\omega \varphi(m) + \int_{\mathbb{R}^3} |\nabla u|^2 - 2 \int_\omega h_{ext} \cdot m, \tag{3.15}$$

(still endowed with the constraint $|m| = 1$ in Ω). The study of (3.15)*, initiated with the paper [69] of James and Kinderlehrer, has received considerable attention in the mathematical literature, see [34, 49, 99, 111, 112].*

4 A hierarchy of thin film models

We now consider thin magnetic films. In this case there are three relevant length scales: the film thickness t, the lateral dimension l and the material parameter d, the Bloch line-width (recall that for many materials d is of the order of 5 nm, see Table 1). Out of these one can form two independent dimensionless parameters. It turns out that for our discussion the most useful parameters are the aspect ratio $\tau = t/l$, already introduced above, and a dimensionless measure of the size of the film given by tl/d^2. We will always study the limit of small aspect ratio

$$\tau = \frac{t}{l} \to 0. \tag{4.1}$$

In this case we identify four different regimes depending on the relation of tl/d^2 and $\ln(1/\tau)$ which lead to four distinct two–dimensional limiting theories, see the first four rows in Table 2. For very small films (l/d fixed and still $t/l \to 0$) one can also consider a different rescaling of the energy leading to a limiting theory which captures higher energy states (see also Table 2).

The different limit theories are much simpler than the full three–dimensional micromagnetic energy functional. They capture the leading–order terms in the energy and lead to a drastic simplification of the very complex micromagnetic energy landscape. They thus provide a good description of the robust features of the magnetization patterns in the thin-film limit. We will discuss this in more detail in the next section in the regime of large thin films ($tl/d^2 \gg \ln(l/t)$) and compare the predictions of the thin film theory with experiments.

In this section we first illustrate the separation of energy scales by investigating the energy contributions of certain prototypical magnetization patterns and then state the rigorous results which lead to Table 2.

4.1 Heuristics and separation of energy scales

Here we briefly discuss the energy contributions of a prototypical magnetization configuration, following closely Section 4 of [38]. The results are summarized in Table 3. We first consider the energy due to variations of m in the x_3 direction, i.e. normal to the film plane. If these variations are of order one they lead to an energy contribution of order l^2d^2/t. In all the relevant regimes this will be much larger than the energy scales we are interested in. Hence for the rest of this heuristic discussion we will suppose

Regime	Energy	Limit	Bulk constraint	Bdry constr.
$tl/d^2 \ll 1/\mathcal{L}$ Stoner-W.	$t^2 l\mathcal{L}$	$(1/2\pi l)\int (m' \cdot \nu')^2$	$m_3 = 0$, $\lvert m \rvert = 1$ $m =$ const	
$tl/d^2 = \lambda/\mathcal{L}$ Bdry penalty	$t^2 l\mathcal{L}/\lambda$	$\int \lvert\nabla' m\rvert^2 + (\lambda/2\pi l)\int (m' \cdot \nu')^2$	$m_3 = 0$, $\lvert m \rvert = 1$	
$tl/d^2 = \mu$ Bdry vortex	$t^2 l/\mu$	$\int \lvert\nabla' m\rvert^2 + \frac{\mu}{l}\int \lvert\nabla V\rvert^2$	$m_3 = 0$, $\lvert m \rvert = 1$	$m' \cdot \nu' = 0$
$tl/d^2 \gg \mathcal{L}$ Magnetostatic	$t^2 l$	$\frac{1}{l}\int \lvert\nabla V\rvert^2$	$m_3 = 0$, $\lvert m \rvert \leq 1$	$m' \cdot \nu' = 0$
$\kappa = d/l$ fixed	tl^2	$\kappa^2 \int \lvert\nabla' m\rvert^2 + \frac{1}{l^2}\int m_3^2$	$\lvert m \rvert = 1$	

Table 2: The different scaling regimes in thin films, with the abbreviation $\mathcal{L} = \ln(l/t) = \ln(1/\tau)$. The second column gives the factor by which the energy is divided before one passes to the limit. The limit energy in the boundary vortex regime is formal, since it is actually infinite on all admissible magnetizations (see text). The limiting energies are invariant under the rescaling $\Omega' \mapsto r\Omega'$, $l \mapsto rl$. Going down in the first four rows corresponds to a passage from small (compared to d) films to large films or, equivalently, to decreasing d. At least on the formal level, the different regimes are naturally connected (taking into account the prefactors in the 'energy' column). The second regime turns into the first as $\lambda \to 0$, while the second and third regime merge as $\lambda \to \infty$ and $\mu \to 0$. Finally, the third regime turns into the fourth as $\mu \to \infty$ (if one looks at the limit in the sense of Γ-convergence, it is natural that the constraint $|m| = 1$ is relaxed in the limit, since the Dirichlet integral drops out).

out–of–plane component m_3	$l^2\, t$
non–tangential component $m' \cdot \nu'$	$l\, t^2\, \ln \frac{l}{t}$
in–plane divergence $\nabla' \cdot m'$	$l\, t^2$
external field H_{ext}	$\lvert H_{ext} \rvert\, l^2\, t$
anisotropy Q	$Q\, l^2\, t$
Néel wall	$l\, t^2\, \ln^{-1} \frac{l\, t}{d^2}$
Bloch line	$d^2\, t\, \ln \frac{l}{d}$
Exchange energy for magnetization varying smoothly on scale l	$d^2\, t$

Table 3: Estimates for the key energy contributions in a soft ferromagnetic film.

that

$$m = m(x_1, x_2) \quad \text{in } \Omega. \tag{4.2}$$

The rigorous convergence results actually show that this holds asymptotically. At finite thickness it is still possible that (4.2) is significantly violated on a small set (this occurs e.g. in asymmetric Bloch walls, cf. Section 6.2), but this turns out to be insignificant for the energy contributions we discuss below.

In view of (4.2) the local energy contributions reduce to

$$d^2 t \int_{\Omega'} |\nabla' m|^2 dx' + Qt \int_{\Omega'} \varphi(m) dx', \tag{4.3}$$

where we use the shorthand notation $x' = (x_1, x_2)$ and write ∇' for the in-plane gradient (∂_1, ∂_2). In the following we will always consider magnetizations that vary smoothly on a scale comparable to the lateral dimension

l. Then, ∇m is of order $1/l$ and the exchange and anisotropy energy contributions are of order $d^2 t$ and $Ql^2 t$, respectively.

The nonlocal magnetostatic energy can be computed by considering the Fourier transform in the tangential direction,

$$\mathcal{F}(m)(\xi') = \frac{1}{2\pi} \int_{\mathbb{R}^2} e^{-i\xi' \cdot x'} m(x')\, dx', \tag{4.4}$$

where m is extended by zero outside Ω', as usual. We note in passing that our normalization of $\mathcal{F}$ differs from the choice made frequently in the physics literature; our choice makes $\mathcal{F}$ an L^2 isometry, i.e. $||\mathcal{F}m||_{L^2} = ||m||_{L^2}$. A short calculation shows that the magnetostatic energy splits into a contribution due to the normal component m_3 (which, in terms of the electrostatic analogy leads to a surface charge at the top and bottom surface of the film), and a contribution due to the in-plane divergence $\operatorname{div}' m'$. We get

$$\begin{aligned} \int_{\mathbb{R}^3} |\nabla U|^2\, dx &= t \int_{\mathbb{R}^2} f\left(\frac{t}{2}|\xi'|\right) \left|\frac{\xi'}{|\xi'|} \cdot \mathcal{F}(m')\right|^2 d\xi' \\ &\quad + t \int_{\mathbb{R}^2} g\left(\frac{t}{2}|\xi'|\right) |\mathcal{F}(m_3)|^2\, d\xi'. \end{aligned} \tag{4.5}$$

Here the Fourier multipliers are given by

$$g(z) = \frac{\sinh(z)}{|z| \exp(z)} = \frac{1 - \exp(-2z)}{2z} \quad \text{and} \quad f(z) = 1 - g(z).$$

Since we assumed that m varies smoothly on a scale comparable to l, its Fourier transform is essentially concentrated on wave vectors ξ' of order $1/l$ or less. In view of our assumption $t/l \ll 1$ the arguments of f and g are thus small in the relevant range of ξ' and we expect that (4.5) is approximated as follows

$$\begin{aligned} &\int_{\mathbb{R}^3} |\nabla U|^2\, dx \\ &\approx \frac{t^2}{2} \int_{\mathbb{R}^2} \frac{1}{|\xi'|} |\xi' \cdot \mathcal{F}(m')|^2\, d\xi' + t \int_{\mathbb{R}^2} |\mathcal{F}(m_3)|^2\, d\xi' \\ &= t^2 \int_{\mathbb{R}^3} |\nabla V|^2\, dx + t \int_{\Omega'} m_3^2\, dx', \end{aligned} \tag{4.6}$$

where V is the single layer potential of the surface charge density $\operatorname{div}' m'$. Classically, V is given as the solution of

$$\left.\begin{aligned} \Delta V &= 0 \quad \text{in } \mathbb{R}^3 \setminus (\Omega' \times \{0\}) \\ [V] = 0 \quad \text{and} \quad &\left[\frac{\partial V}{\partial x_3}\right] = \operatorname{div}' m' \quad \text{on } \Omega' \times \{0\} \end{aligned}\right\}. \tag{4.7}$$

Here $[\cdot]$ denotes the jump of a quantity $\cdot$ across the plane $\mathbb{R}^2 \times \{0\}$. A different heuristic argument giving the energy contribution of the in-plane divergence of m is as follows: The potential U^t satisfies Maxwell's equation $\Delta U^t = \operatorname{div}(m(x')\chi_{(0,t)}(x_3))$, where $\chi_{(0,t)}$ is 1 in the interval $(0,t)$ and zero outside. Dividing by t and considering that $\chi_{(0,t)}/t$ converges formally to the Dirac mass δ_0 we see that the limit V of U^t/t is given by (4.7). For a rigorous argument using the relevant weak formulation of (4.7), see [38], p. 1439.

The above characterization of V implicitly contains the assumption that the normal component of m' does not jump across a possible discontinuity line of m', in particular

$$m' \cdot \nu' \;=\; 0 \quad \text{on } \partial\Omega', \tag{4.8}$$

where ν' denotes the normal to the boundary $\partial\Omega'$ of the cross section Ω'. We will come back to this shortly.

¿From (4.6) we first recover the classical argument of Néel that in thin films a nonzero normal component m_3 leads to a large energy contribution of order tl^2. If the in-plane magnetization satisfies (4.8) then a scaling argument in connection with (4.7) shows that the magnetostatic energy is of order $t^2 l$.

If m' does not satisfy (4.8) then an additional energy contribution due to the boundary 'charge' $m' \cdot \nu'$ arises. To compute it one has to go back to the exact representation (4.5) of the magnetostatic energy and a short calculation shows that for a constant magnetization and a straight boundary piece the extra contribution per unit length is of order $t^2 \ln(l/t)(m' \cdot \nu')^2$, see e.g. [38], Section 4.4. For a general boundary one thus expects an extra contribution of the order

$$t^2 \ln(l/t) \int_{\partial\Omega'} (m' \cdot \nu')^2. \tag{4.9}$$

We will see in the next subsection that this is indeed the case, see (4.12) below.

So far we have implicitly assumed that the magnetization is smooth and varies on a typical scale proportional to the lateral extension l of the film. Typical magnetization patterns, however, consist of regions of slowly varying magnetization (domains) which are separated by domain walls, in which the magnetization changes rapidly. We will see below in Subsection 6.3 that the energy of a typical domain wall in thin films, i.e. the Néel wall, is of order $l^2 t / \ln(lt/d^2)$ and thus is asymptotically negligible compared with the magnetostatic energy contributions. One can also check that the energy of a Bloch line (where the magnetization develops a nontrivial m_3 component on a region of diameter d) is of order $d^2 t \ln(l/d)$ and also asymptotically negligible, see (7.21) below and Section 4.5 in [38].

4.2 Rigorous convergence results - the first four regimes

The heuristic discussion on the separation of energy scales suggests that in the thin film limit we get a strong simplification of the energy landscape. If we select a certain energy regime then all energy contributions below this level will become asymptotically irrelevant. Energy contributions that are asymptotically much larger are not allowed to be present, i.e. they lead to constraints in the limiting theory. Typical examples are the constraint that m should become independent of x_3 or that the out-of-plane component m_3 should vanish.

We now describe the rigorous results which are motivated by this reasoning and which are summarized in Table 2. We first focus on the first four rows of this table. It is interesting to note that these four regimes capture very well the qualitative changes in the experimentally observed patterns for increasing size, even though they are mathematically only separated by logarithmic terms. For extremely small films one sees (nearly) uniform states (Stoner-Wohlfarth regime). With increasing size one finds flower states (boundary penalty regime), states with vortices on the boundary, such as the C- and S-states in rectangular samples or the buckle and leaf states in square samples (boundary vortex regime), and flux-closed patterns (magnetostatic regime).

To state the results precisely it is convenient to work in a fixed two–dimensional domain ω' (e.g. the unit square) obtained from Ω' by rescaling all lengths by l. We thus employ the scalings (3.3)–(3.8). For brevity we consider only the situation with zero applied field. Adding a suitably scaled applied field poses no additional difficulty since this represents a continuous perturbation and therefore passes through the Γ-limit, see Section 10. As before we always consider the small-aspect-ratio limit, i.e

$$\tau \to 0, \tag{4.10}$$

and we denote by e^τ the minimal micromagnetic energy for a sample with aspect ratio τ.

In the regime of very small films, i.e. if $(lt/d^2)\ln(l/t) \to 0$ or, equivalently,

$$\frac{\tau}{\kappa^2}\ln(1/\tau) \to 0, \tag{4.11}$$

Table 3 suggest that the most interesting term is the one arising from the boundary energy (4.9). Indeed Kohn and Slastikov [80] showed (see also Carbou [24]) that

$$\frac{1}{\tau \ln(1/\tau)} e^\tau \xrightarrow{\Gamma} e, \tag{4.12}$$

where

$$e = \begin{cases} \frac{1}{2\pi} \int_{\partial\Omega'} (m' \cdot \nu')^2 & \text{if } m = \text{const}, m_3 = 0, |m| = 1, \\ \infty & \text{else.} \end{cases} \tag{4.13}$$

To make the Γ-convergence result precise, we need to specify the convergence of three–dimensional magnetizations $m^\tau : \omega \to \mathbb{R}^3$ to a two–dimensional limit m. We say that convergence holds if the x_3-averages $\bar{m}^\tau = (1/\tau) \int_0^\tau m^\tau dx_3$ converge strongly to m in L^2.

If

$$\frac{\tau}{\kappa^2} \ln(1/\tau) \to \lambda \tag{4.14}$$

(small body limit) then [80]

$$\frac{\lambda}{\tau \ln(1/\tau)} e^\tau \xrightarrow{\Gamma} e, \tag{4.15}$$

where

$$e = \begin{cases} \int_{\Omega'} |\nabla' m|^2 + \frac{\lambda}{2\pi} \int_{\partial\Omega'} (m' \cdot \nu') & \text{if } m_3 = 0, |m| = 1, \\ \infty & \text{else.} \end{cases} \tag{4.16}$$

On the other hand, if the body remains large in the sense that

$$\frac{\tau}{\kappa^2} \frac{1}{\ln(1/\tau)} \to \infty \tag{4.17}$$

then the magnetostatic energy dominates and we have, in the sense of Γ-convergence (with respect to weak L^2 convergence of x_3 averages) [38]

$$\frac{1}{\tau} e^\tau \xrightarrow{\Gamma} \int_{\mathbb{R}^3} |\nabla v|^2 \tag{4.18}$$

provided that $m_3 = 0$ and that m satisfies the relaxed (convexified) constraint $|m| \leq 1$ (else the limit energy is ∞). Here v is the single layer potential of $\text{div}' m'$ defined as in (4.7) (replacing Ω' by the nondimensionalized domain ω'). In particular this imposes the constraint $m' \cdot \nu' = 0$ (for nonsmooth fields m' this has to be understood in the sense of traces, see

[38]). A more detailed discussion of this result, its interpretation and comparison of the predictions of the limit theory with experiments appears in the next section.

Finally for the critical scaling

$$\frac{\tau}{\kappa^2} = 1 \tag{4.19}$$

the limit of e^τ/τ is formally given by

$$\int_{\omega'} |\nabla' m|^2 + \int_{\mathbb{R}^3} |\nabla v|^2, \tag{4.20}$$

subject to the constraints $m_3 = 0$ and $|m| = 1$. Here v is defined as in (4.7), replacing Ω' by the non-dimensionalized domain ω'. The problem is that the limit functional is infinite on all admissible test functions, if ω' is simply connected, e.g. if ω' is a disk or a square. Indeed, the constraint (4.8) forces m' to be tangential at the boundary, but there is no unit vector field in H^1 which is tangential to the boundary. Moser [94, 95] has nonetheless shown that the above formal limit captures the right behavior. More precisely he shows that

$$2\pi \ln\ln(1/\tau) - C \leq \frac{1}{\tau} \min e^\tau \leq 2\pi \ln\ln(1/\tau) + C \tag{4.21}$$

and that the x_3-averages of minimizers of e^τ converge (strongly in the Sobolev space $W^{1,p}$, for all $p < 2$) to a limit m which has two singularities (vortices) on $\partial\omega'$, is otherwise tangential to $\partial\omega'$ and satisfies the Euler-Lagrange equation corresponding to (4.20) in ω'.

4.3 The fifth regime

The fifth regime corresponds to letting the aspect ratio $\tau = t/l$ tend to zero, while keeping $\kappa = d/l$ fixed. It was historically the first regime for which a rigorous convergence result was obtained. In fact Gioia and James [56] showed that in this regime the energy functionals e^τ Γ-converge to e_{GJ} given by

$$e_{GJ}(m) = \begin{cases} \kappa^2 \int_{\omega'} |\nabla' m|^2 + \int_{\omega'} m_3^2 & \text{if } m \in H^1(\omega'), \\ +\infty & \text{else,} \end{cases} \tag{4.22}$$

where ∇' is the in-plane gradient.

Like the first regime this regime corresponds to very small films. The important difference is that one considers here just energy e^τ (without further rescaling) while in the first regimes one rescales the energy by $1/(\tau \ln(1/\tau))$. The setting of Gioia and James emphasizes the fact that the nonlocal magnetostatic energy reduces to the local term m_3^2 which behaves like an effective anisotropy (this is thus an extreme case of shape anisotropy). The limiting functional has many (minimizing) zero energy states. In fact, all constant in-plane magnetizations have zero limiting energy.

The first regime breaks the degeneracy between all these states and assigns to them a refined limiting energy according to $\int_{\partial\omega'}(m' \cdot \nu')^2$. On the other hand, the limit functional for the first regime does not discriminate between limiting magnetizations which are not constant in-plane fields and assigns infinite energy to all of them.

5 A two–dimensional model for large soft films and comparison with experiment

In this section we discuss in detail the regime $lt/d^2 \gg \ln(l/t)$, which corresponds to large films. This regime is of special interest for at least two reasons. First, it covers a large range of concrete samples (including e.g. thicknesses from a few nm to hundreds of nm and lateral dimensions from 1 μm to several hundred μm and larger). This allows us to compare the predictions of the thin-film theory with a wealth of experimental data. Secondly this regime covers exactly a range of parameters which is not accessible by direct numerical simulation of the full micromagnetic functional $E(m)$, since large lateral dimensions beyond a few μm would require an excessive number of discretization points for an accurate resolution of all the relevant length scales.

5.1 Statement of the limit problem and the convergence result

For the rest of this section we will neglect anisotropy, i.e. we will set $Q = 0$. Table 3 suggests that anisotropy is indeed negligible as long as $Q \ll \tau = t/l$ and this is established rigorously in [38]. For Permalloy we have $Q = 2.5 \times 10^{-4}$ so that the condition $Q \ll \tau = t/l$ is indeed well satisfied, even for films with very small aspect ratio. To simplify the comparison with experiments we will explicitly include an in-plane applied field H_{ext} (usually to be taken as constant).

We thus study the three–dimensional energy functional (2.17)

$$E(m) = d^2 \int_\Omega |\nabla m|^2 + \int_{\mathbb{R}^3} |\nabla U|^2 - 2 \int_\Omega H_{ext} \cdot m, \tag{5.1}$$

where (see (2.15))

$$H_{ext} = \frac{\mu_0 \mathbb{H}_{ext}}{J_s}. \tag{5.2}$$

After the non-dimensionalization (3.3)–(3.8) this becomes

$$e^\tau(m) = \kappa^2 \int_\omega |\nabla m|^2 + \int_{\mathbb{R}^3} |\nabla u|^2 - 2 \int_\omega h_{ext} \cdot m, \tag{5.3}$$

where $\omega = \omega' \times (0, \tau)$ and $\tau = t/l$ is the aspect ratio of the film. For both functionals we impose the constraint

$$|m| = 1, \tag{5.4}$$

and the potentials U and u are determined from m through the static Maxwell equations (2.20) and (3.9), respectively. Table 3 suggests that a natural scaling for the applied field is $H_{ext}(x) = \tau \tilde{h}_{ext}(x/l)$. We also assume that the applied field is in-plane. We thus suppose

$$H_{ext}(lx) = h_{ext}(x) = \tau \begin{pmatrix} \tilde{h}'_{ext}(x_1, x_2) \\ 0 \end{pmatrix}. \tag{5.5}$$

Theorem 5.1 *Suppose that*

$$\tau \longrightarrow 0, \quad \frac{\kappa^2}{\tau} \ln \frac{1}{\tau} \longrightarrow 0 \tag{5.6}$$

and that h_{ext} *is given by* (5.5) *with* $\tilde{h}'_{ext}$ *fixed. Then*

$$\frac{1}{\tau} e^{\tau} \xrightarrow{\Gamma} e, \tag{5.7}$$

where

$$e(m) = \left\{ \begin{array}{ll} \int_{\mathbb{R}^3} |\nabla v|^2 - 2 \int_{\omega'} \tilde{h}'_{ext} \cdot m' & \textit{if } m_3 = 0, \quad |m'| \leq 1, \\ +\infty & \textit{else} \end{array} \right. \tag{5.8}$$

and where v *is the single layer potential of* $\mathrm{div}' m'$*, i.e.*

$$\left. \begin{array}{rcl} \Delta v &=& 0 \quad \textit{in}\, \mathbb{R}^3 \setminus (\omega' \times \{0\}) \\ {[v]} &=& 0 \quad \textit{and} \quad \left[\frac{\partial v}{\partial x_3}\right] = \mathrm{div}'\, m' \qquad \textit{on}\; \omega' \times \{0\} \end{array} \right\}. \tag{5.9}$$

We recall that the energy $\int |\nabla v|^2$ of the single layer potential of $\mathrm{div}' m'$ is only finite if the normal component of m' does not jump across a possible discontinuity curve of m', in particular if

$$m' \cdot \nu' \;=\; 0 \quad \text{on } \partial\omega'. \tag{5.10}$$

As before Γ-convergence is taken with respect to weak L^2 convergence of thickness averages, i.e. we say that at sequence of three–dimensional magnetizations m^τ converges to a two–dimensional magnetization m as $\tau \rightarrow 0$, if

$$\frac{1}{\tau} \int_0^\tau m^\tau(\cdot, x_3)\, dx_3 \rightarrow m \quad \text{weakly in } L^2(\omega', \mathbb{R}^3). \tag{5.11}$$

In the following we will view e as a functional on tangential vector fields $m' = (m_1, m_2)$, keeping in mind the constraint $m_3 = 0$. One feature of Theorem 5.1, which may look unusual at first glance, is that the unit length constraint on m is replaced by the inequality constraint $|m'| \leq 1$ on the limiting in-plane magnetizations m'. We discuss this in more detail in Remark 5.3 at the end of the next subsection.

The proof of Theorem 5.1 is given in [38]. The heuristic justification of the argument is that the scaling assumptions on t and l (or equivalently on $\tau = t/l$ and $\kappa = d/l$) are precisely what is needed to ensure that the key energy contributions are clearly separated in the thin film limit, as shown in Table 3. Indeed, the hypothesis $\tau \to 0$ implies that the scaling in the upper tier of the table is stronger than lt^2, the hypothesis (5.5) makes sure that the middle tier scales as lt^2 (with the exception of the anisotropy energy, which has been dropped), while the scaling of the lower tier is weaker than lt^2 in view of the assumption $\tau^{-1}\kappa^2 \ln(1/\tau) \to 0$. For the upper tier, energy penalization in the full model turns into a constraint in the reduced model. The middle tier gives the leading–order energy scaling of the full model, giving rise to the reduced limiting model. This is determined by a competition of penalization of in-plane divergence with the energy contributions of the external field. Finally, the lower tier contains terms that are of higher order, see (6.19) and (7.21).

Theorem 5.1 ensures, in particular, that sequences m^τ of ground states for the full micromagnetic problem converge (in the sense of (5.11)) to magnetizations $(m', 0)$ which solve the reduced problem. In fact, we will use knowledge about the behavior of minimizers of the reduced problem to deduce information on some of the asymptotic features of micromagnetic minimizers, in the thin film limit, see Corollary 5.2 below. The reduced problem however, is degenerate. The following discussion clarifies what we can actually learn by minimizing the reduced energy.

5.2 Discussion of the reduced problem, its Euler-Lagrange equation and the relation with the theories of van den Berg and Bryant and Suhl

The reduced variational problem is convex. It is even strictly convex in the potential v. Consequently, v is uniquely predicted by energy minimization. On the other hand the reduced variational problem is highly degenerate in m': for constant external field $\tilde{h}'_{ext} = \text{const}$ the energy e depends on m' only through its in–plane divergence $\operatorname{div}' m'$.

To extract further information from the reduced variational problem and to compare it to existing models in the physics literature, it is very instructive to look at the corresponding Euler-Lagrange equation (since the problem is convex, solutions of the Euler-Lagrange equations and minimizers of the functional agree). These can be written in the form

$$-\nabla'\tilde{v} + \tilde{h}'_{ext} \;=\; \lambda m' \quad \text{on}\, \omega', \tag{5.12}$$

where $\lambda = \lambda(x') \geq 0$ is the Lagrange multiplier corresponding to the inequality constraint

$$|m'| \leq 1. \tag{5.13}$$

It turns out that for sufficiently small applied fields the constraint is not active, i.e. one can satisfy (5.12) with $\lambda \equiv 0$. Then the Euler-Lagrange equation reduces to

$$-\nabla'\tilde{v} + \tilde{h}'_{ext} = 0, \tag{5.14}$$

i.e. in this case the stray field $-\nabla' v$ compensates the external field within the sample (in our thin–film framework). This is analogous to electrostatics, where charges on $\partial\omega$ arrange themselves to shield the interior ω of a conductor from an external field.

The model of van den Berg [113] considers the case without external field and in view of (5.14) predicts that the stray field and thus $\operatorname{div}' m'$ vanishes ('flux closure').

The model of Bryant and Suhl [19] allows for an external field and determines $\nabla' v$ and thus $\operatorname{div}' m'$ from (5.14). The constraint (5.13) on the magnetization, however, limits the 'charges', unlike the case in electrostatics. Hence stronger external fields 'penetrate' into the sample and we have

$$\tilde{h}'_{pen} = -\nabla' v + \tilde{h}'_{ext} \neq 0. \tag{5.15}$$

Therefore, our model extends the model of Bryant and Suhl [19] and puts it in a natural variational context.

In the region of field penetration

$$\omega'_{pen} \;:=\; \{\, x' \in \omega' \,|\, \tilde{h}'_{pen}(x') \neq 0 \,\}, \tag{5.16}$$

m' is uniquely determined by the Euler-Lagrange equation, in fact $m' = \tilde{h}'_{pen}(x')/|\tilde{h}'_{pen}(x')|$. Moreover, the region ω'_{pen} is itself uniquely determined since it only depends on the uniquely determined potential v. We notice in passing that, in order to properly define ω'_{pen}, we need some technical assumptions ensuring some regularity of v (in [38] it is shown that, for constant applied field, these are satisfied if ω' is simply connected; for the situation without anisotropy considered here, even this assumption can be dropped, see [88]).

Using the additional information arising from the Euler-Lagrange equation of the reduced problem we can strengthen the results that naturally follow from Theorem 5.1. In particular, we can strengthen the notion of convergence of micromagnetic minimizers to minimizers of the reduced problem.

Corollary 5.2 *Under the assumptions of Theorem 5.1 and assuming, in addition, that* $\tilde{h}'_{ext}$ *is constant, we have*

i) Let m' *and* n' *be two minimizers of the reduced variational problem with corresponding potentials* v *and* w*. Then* $w = v$ *and*

$$m' = n' = \tilde{h}'_{pen}/|\tilde{h}'_{pen}| \quad \text{on } \omega'_{pen}, \tag{5.17}$$

where $\tilde{h}'_{pen}$ *and* ω'_{pen} *are defined in* (5.14) *and* (5.16)*, respectively.*

ii) Suppose that m^τ *is a sequence of almost minimizers of* e^τ/τ*, i.e.*

$$\lim_{\tau\to 0} \frac{1}{\tau}(e^\tau(m^\tau) - \min e^\tau) = 0. \tag{5.18}$$

Then we have for any minimizer m' *of the reduced variational problem and its potential* v

$$\begin{aligned} \lim_{\tau\to 0} \frac{1}{\tau} \int_{\omega'_{pen}\times(0,\tau)} \left| m^\tau - \begin{pmatrix} m' \\ 0 \end{pmatrix} \right|^2 dx &= 0, & (5.19) \\ \lim_{\tau\to 0} \int_{\mathbb{R}^3} \left| \frac{1}{\tau}\nabla u^\tau - \nabla v \right|^2 dx &= 0, & (5.20) \\ \lim_{\tau\to 0} \frac{1}{\tau} e^\tau(m^\tau) &= e'(m'). & (5.21) \end{aligned}$$

Remark 5.3 *We now come back to the point that the reduced problem only involves the inequality constraint* $|m'| \le 1$ *while we impose the condition* $|m| = 1$ *in the three–dimensional problem. This relaxation of the constraint might be surprising from a physics point of view - indeed both van den Berg and Bryant & Suhl consider only magnetization fields of unit length.*

To understand this relaxation of the constraint better we first explain why it arises naturally in the Γ*-convergence setting and then discuss how the unit length constraint might be restored through a finer analysis.* Γ*-convergence analyzes the energy functional at a particular energy scale. Theorem 5.1 says in particular that given a two–dimensional magnetization field* m' *with* $e(m') < \infty$*, there exists a sequence of three–dimensional magnetization fields*

m^t which converge weakly to m' (in the sense of (5.11)*) such that $e^\tau(m^\tau)/\tau$ converges to $e(m')$, even if $|m'| < 1$. In fact if m' is a minimizer of e (for a given applied field) then the fields m^τ can be chosen as approximate minimizers in the sense of* (5.18)*. The reason that this is possible is, roughly speaking, the low energy of Néel walls. To achieve, e.g., the limit $m' = 0$ one can consider magnetization patterns which consist of thin strips with magnetization $\pm(1, 0, 0)$, separated by Néel walls. Since the energy of a Néel wall is negligible compared with the other energy contributions (see Table 3) one can let the number of stripes and Néel walls go to infinity as $\tau \to 0$ (at a sufficiently slow rate), thus obtaining a sequence of magnetizations whose volume average converges to zero at each fixed scale (this is exactly weak convergence) and for which the additional energy due to the walls is negligible (for a general limiting pattern the actual implementation of this idea is rather delicate and is discussed in detail in [38]).*

The low energy of Néel walls thus allows one to construct highly oscillatory magnetization patterns that still have low energy. In contrast to the situation for the large body limit, however, the limit functional does not favor magnetizations that satisfy $|m'| < 1$. In fact, we will see in the next section that given a minimizer m'_0 with $|m'_0| < 1$ one can construct a new minimizer m' (for the same applied field) that satisfies $|m'| = 1$. Thus, one might speculate that rapid oscillations of m^τ are never necessary. In other words, if one considers minimizers $\hat{m}^\tau$ of e^τ (and not just approximate minimizers) then they may converge strongly to a limit m' that satisfies $|m'| = 1$. Mathematically this is so far an unsolved problem, even though some results are available for related, but different, problems [8, 37, 67, 68, 103, 104]. To make progress on this question one could view the result in Theorem 5.1 as the zero–order term in an asymptotic expansion of the energy and one would then need to understand the higher-order terms that break the degeneracy of the zero–order limit functional (we have seen such a hierarchy of Γ-limits in Section 4.3; a very simple one–dimensional example is discussed in Section 10.3). Some results on such higher-order contributions are discussed in Section 6.

5.3 Numerical implementation

The reduced model can be used for the computation of domain patterns. Following the algorithm proposed in [40], we proceed in two steps. First, we use to our advantage the fact that replacing the nonconvex constraint $|m'|^2 = 1$ with the relaxed, convex constraint $|m'|^2 \leq 1$ does not change the minimum of e'. Thus, we minimize the reduced energy e' among all regular, in–plane vector fields of length less than or equal to one:

Step 1. Find a regular m'_0 minimizing e'.

(We call an in–plane vector field $m'(x')$ on ω "regular" if it satisfies $[m' \cdot \nu'] = 0$ across all possible discontinuity lines and at $\partial\omega$). The in–plane divergence $\mathrm{div}'\, m'$ is known to have characteristic singularities near the edges and corners of ω. Since the energy e' depends on m' only through $\mathrm{div}'\, m'$, this raises the question of how to choose a local refinement strategy for a triangulation of ω. In [44] we derive the necessary refinement rate to retain the optimal rate of convergence in the energy norm. In particular, we show that it is sufficient to refine the triangulation towards the edges (and not the corners).

Computation of the magnetostatic part of the energy leads to matrix–vector products with fully populated matrices due to the nonlocal character of the magnetostatic interaction. On translation invariant grids one can apply the Fast Fourier Transform (FFT) to reduce computational cost from $\mathcal{O}(N^2)$ to $\mathcal{O}(N \log N)$. On locally refined triangulations we use the method of $\mathcal{H}$–matrices (hierarchical matrices) as introduced in [58]. This method relies on the fact that submatrices of the original matrix can be replaced by suitable low-rank approximations. The approximate matrix is then stored in a hierarchical data structure of size $\mathcal{O}(N \log N)$, thus allowing an evaluation of matrix–vector products in $\mathcal{O}(N \log N)$ time. We implement a new class of hierarchical matrices, the so–called $\mathcal{H}^2$–matrices [59], with optimal complexity $\mathcal{O}(N)$ in the matrix–vector multiplication.

An application of $\mathcal{H}^2$–matrices to three–dimensional stray field computations in micromagnetics is given in [27], where the large body limit, cf. Section 3.2, is considered. In conjunction with a boundary integral formulation of the three–dimensional stray field, $\mathcal{H}$-matrices have been used in [50].

The m'_0 obtained at the end of the first step has the correct energy, but in general violates the unit length constraint. The second step postprocesses m'_0 to obtain a minimizer m' of e' with unit length according to the following procedure.

Step 2. For a given regular m'_0 of at most unit length, find a scalar function ψ solving

$$\begin{aligned} |\nabla'^{\perp}\psi + m'_0|^2 &= 1 \text{ in } \omega, && (5.22)\\ \psi &= 0 \text{ on } \partial\omega. && (5.23) \end{aligned}$$

The computed domain pattern m', which we later compare with experiments, is obtained by setting $m' = \nabla'^{\perp}\psi + m'_0$.

The first step in the algorithm above involves a convex (but degenerate) variational problem. We solve it with an interior point method [114]. In more detail, the convex constraint is enforced by adding to the physical energy e' a small multiple s of a self-concordant barrier B. The unique stationary point of the strictly convex functional $e' + sB$ is computed by Newton's method. This is then used as the initial guess for the minimizer of $e' + \tilde{s}B$, where $\tilde{s} < s$. The parameter s is then slowly decreased by multiplicative increments. Within Newton's method, the Hessian of $e' + sB$ is inverted by a preconditioned conjugate gradient method, where the magnetostatic part of the Hessian is evaluated with the help of $\mathcal{H}^2$–matrices.

For the second step, we recall that there are many Lipschitz continuous solutions of (5.22),(5.23). However, there is a special solution, known as the viscosity solution, which has special mathematical properties. This can be computed efficiently using the level set method [107]. This is the pointwise solution of (5.22),(5.23) selected by our algorithm.

Our numerical scheme selects, automatically and robustly, one out of the many minimizers of the reduced energy e'. The selection principle implicit in this scheme is the same as the one often proposed in the physics literature. Indeed, it appears to pick minimizers with as few walls as possible. Clearly, a more physical selection mechanism should be based on minimizing wall energy. This requires, however, the characterization of energy terms that represent higher order corrections of our model, a step that seems to be far from trivial. Understanding wall energies requires, in particular, the understanding of their structures. Preliminary steps in this direction are discussed in Section 6.

Figure 5 shows the predictions of our numerical scheme for a square film of edge-length one, subject to a monotonically increasing field applied along the diagonal. This rather special geometry was chosen to guarantee that nontrivial domain patterns could persist beyond penetration of the external field, as illustrated by the 90–degree domain wall emerging from the bottom right corner of the sample.

5.4 Comparison with experiment

To check the predictions of the reduced theory, the response of two AC-demagnetized Permalloy ($Ni_{81}Fe_{19}$, $J_s = 1.0$ T) square samples of edge lengths $L = 30$ and 60 μm and thicknesses $D = 40$ and 230 nm, respectively,

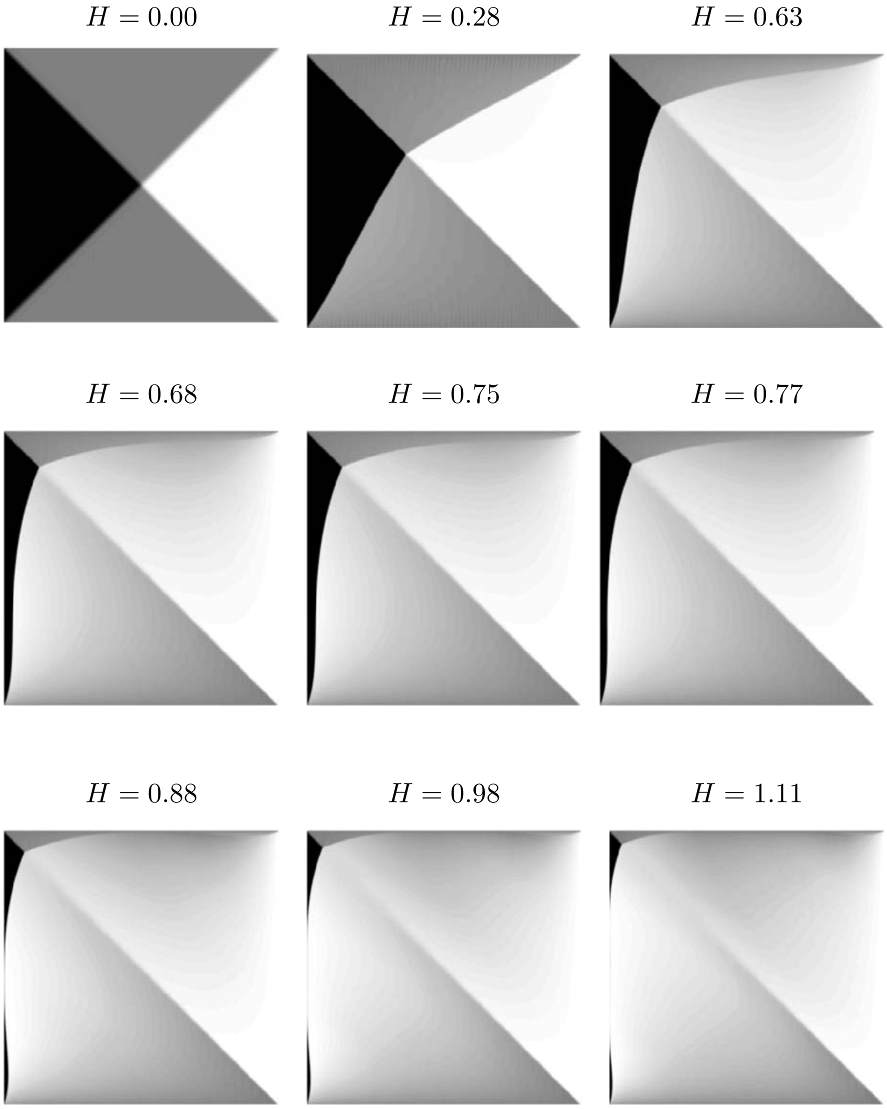

$H = 0.00$ $H = 0.28$ $H = 0.63$

$H = 0.68$ $H = 0.75$ $H = 0.77$

$H = 0.88$ $H = 0.98$ $H = 1.11$

Figure 5: Predictions of the two–dimensional theory: gray–scale plots of the vertical component of the computed magnetization.

have been observed in a digitally enhanced Kerr microscope, [40]. The observed domain patterns are given in Figures 6, 7, where the field intensity H_{ext}, measured in Tesla, is scaled according to

$$H = \frac{l}{d}\frac{H_{ext}}{J_s}. \tag{5.24}$$

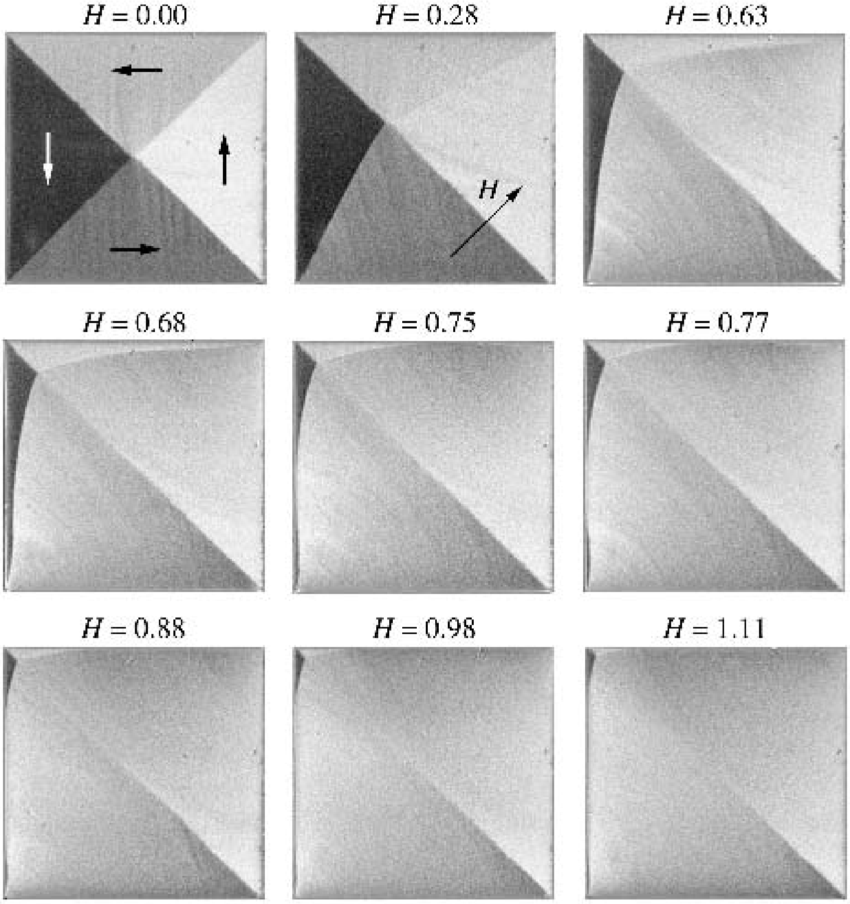

Figure 6: Permalloy films: $L = 60$ μm, $D = 230$ nm.

In comparing Figures 5, 6, and 7 one may speculate that the small lag in the strength of the applied field exhibited by the thinner samples may be due to the fact that, for these films, the walls are of Néel type and they

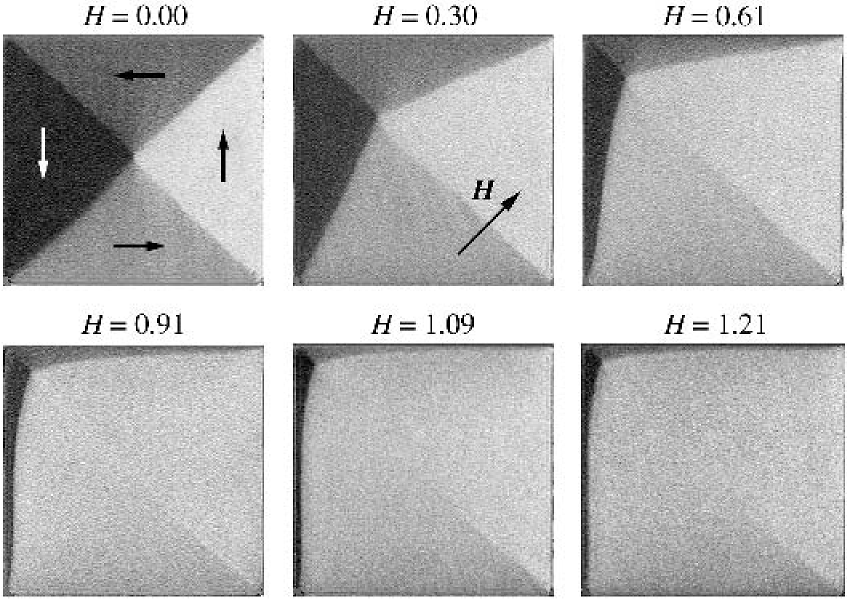

Figure 7: Permalloy films: $L = 30$ μm, $D = 40$ nm.

are repelled by the lateral boundary, cf. Section 6.4 for a discussion of their repulsive effect. This effect, whose impact on the hysteretic response of soft films is discussed in [41], could be captured by an enhanced two–dimensional model in which higher-order terms in the film thickness are taken into account.

Figure 8 examines more closely the predictions of our theory, and, in particular, the phenomenon of external field penetration. In order to estimate the critical field strength at which penetration occurs, we have superimposed on each gray-scale plot the level curves of the potential v_{pen} of the penetrated field, defined by

$$-\nabla' v_{pen} = \tilde{h}'_{pen} = -\nabla' v + \tilde{h}'_{ext} \,,$$

see eq. 5.15. Regions where the field lines concentrate are regions where $\nabla v_{pen} \neq 0$, i.e., where the external field has penetrated the sample. Within them, the Euler-Lagrange equation (5.12) implies that m' is parallel to ∇v. The theory predicts that m' can have no walls in the penetrated region. The pictures confirm this, and show quite clearly that two apparently independent phenomena – the expulsion of the domain walls from the interior of the sample and the penetration of the external field – are in fact two manifestations of the same event.

The comparison between computed patterns and experimental observations shows that the material parameter regime in which the constructions of the theories of van den Berg and of Bryant and Suhl are relevant is correctly identified. Moreover, the successful comparison shows that the energy at leading order is captured in a satisfactory way by the reduced model described in this section.

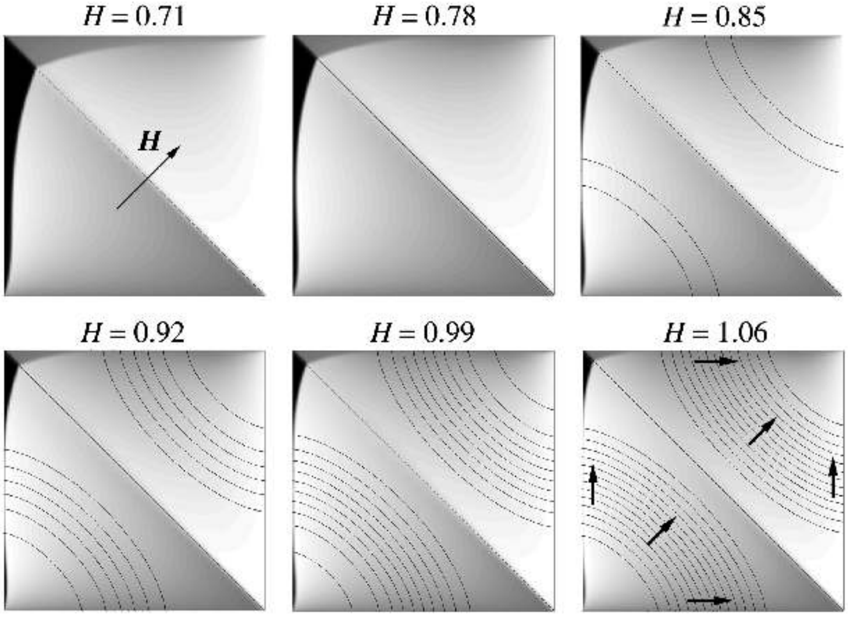

Figure 8: The transition between expulsion and penetration regimes. Lines show the level curves of the potential of the penetrated field, arrows indicate the magnetization direction.

6 Higher order terms and wall structures

In this section, we discuss walls in ferromagnetic films of low anisotropy. Walls are transition layers in the magnetization which separate domains. What are the mechanisms which stabilize such a transition layer? Ordinary Bloch walls in bulk samples arise from the competition of exchange energy and crystalline anisotropy, cf. Section 7.2 and [66, 3.6.1 (A)]. As we shall see, walls in films rather arise from the competition of exchange and magnetostatic energy. Apart from the intrinsic interest in these structures, their energetic contributions are also expected to play a crucial role in breaking the degeneracy of the two–dimensional limit functional (5.8) discussed in the previous section.

Following van den Berg, [113], we shall start by explaining why there are walls at all in low anisotropy ferromagnetic films, cf. Subsection 6.1. Then we will discuss the wall structures themselves – as it turns out, the picture is quite complex. In Subsection 6.2, we introduce the two basic wall types, the Néel wall and the stray–field free asymmetric Bloch wall. The thickness–dependent crossover can be rigorously identified on the level of the specific line energy [98]. The Néel wall is a multiscale object in itself. In Subsection 6.3, we discuss the logarithmic tail of the Néel wall, and present its rigorous analysis by Melcher [89, 90]. In Subsection 6.4, we discuss the core of the Néel wall in moderately thin films, and present some rigorous analysis on how the volume charge is distributed between core and tail [39]. In Subsection 6.5, we introduce the cross–tie wall, which is a compound wall made of a periodic microstructure of Néel wall segments. It is observed in moderately thin films. We present the rigorous analysis by Alouges, Rivière and Serfaty [7], which identifies an optimal pattern. In Subsection 6.6, we give an explanation why the Néel wall in very thin films does not form a cross–tie pattern [42]. In Subsection 6.7, we address the mechanisms which determine the period of the cross–tie wall. In Subsection 6.8, we consider thick films with a perpendicular uniaxial anisotropy and analyze domain branching [28, 29].

For each topic, we start with an informal discussion, then present the rigorous result and finally give some insight into its proof. The arguments of this section rely on the variational nature of the micromagnetic model: The ground state structures are characterized as minimizers of the energy. Physically motivated constructions ('models') yield upper bounds on the minimal energy. A rigorous analysis can contribute by establishing that these upper bounds cannot be improved (in terms of scaling, asymptotically or exactly). Even if these ansatz–free lower bounds just capture the correct scaling, they allow to unambiguously identify the various regimes. We shall try to give an idea on how such lower bounds are obtained.

6.1 Why walls in soft ferromagnetic films?

Based on the nonrelaxed "magnetostatic regime" introduced in Section 4 we shall very informally explain how the principle of pole avoidance leads to the formation of walls in ferromagnetic *films*, even in the absence of crystalline anisotropy. This discussion follows the lines of van den Berg's work, see e. g. [113]. Let us think of a "mesoscopic" magnetization m where walls would be represented by line discontinuities. In the magnetostatic regime, the exchange energy suppresses the variation of m in the thickness direction, i. e. $m = m(x')$. The magnetostatic energy, on the other hand, suppresses the out–of–plane component, i. e. $m = m' \in \mathbb{S}^1$, it suppresses a non–tangential component, i. e. $m' \cdot \nu' = 0$ along $\partial\Omega'$, and suppresses the in–plane divergence, i. e. $\nabla' \cdot m' = 0$ in Ω'. This is the principle of pole avoidance. We collect these conditions on the two–dimensional unit length $m'(x')$:

$$\nabla' \cdot m' = 0 \ \text{ in } \ \Omega' \quad \text{and} \quad m' \cdot \nu' \ = \ 0 \ \text{ along } \ \partial\Omega'. \tag{6.1}$$

These conditions are too rigid for a smooth mesoscopic m'. This can be seen by using the first property of (6.1) to write m' with the help of a stream function ψ as $m' = \nabla'^{\perp}\psi$. Then is seen the fact that $m' \in \mathbb{S}^1$ and the second condition in (6.1) turn into the Dirichlet problem for the eikonal equation, i. e.

$$|\nabla'^{\perp}\psi|^2 \ = \ 1 \ \text{ in } \ \Omega' \quad \text{and} \quad \psi \ = \ \text{const} \ \text{ along } \ \partial\Omega'. \tag{6.2}$$

(This is a special case of (5.22) and(5.23).) It is well known that (6.2) does not admit a smooth solution for a simply connected, bounded Ω'. On the other hand, (6.2) admits many continuous solutions that satisfy the first condition of (6.2) outside of a set of lower dimensionality. The simplest one, the "viscosity solution", is the distance function to $\partial\Omega'$:

$$\psi(x') \ = \ \text{dist}(x', \partial\Omega'). \tag{6.3}$$

The negative distance function $\psi(x') = -\text{dist}(x', \partial\Omega')$ is of course as good, or any distance function of the form $\psi(x') \ = \ \text{dist}(x', \partial\Omega' \cup \Gamma')$ where Γ' is an arbitrary curve. Notice that unless Ω' is a disk, all these functions ψ feature lines across which the derivative jumps. Hence we learn that the solution concept for (6.2) has to be relaxed to allow for line singularities. This therefore applies also to (6.1): For (6.1) to be solvable, one has to admit for line singularities and interpret the first condition in (6.1) in the distributional sense.

It is tempting to interpret these line singularities of the mesoscopic magnetization enforced by (6.1) as walls. Indeed, van den Berg has shown that huge variety of domain and wall patterns in the "magnetostatic regime" fit into the above framework. Let us just mention the "Landau state", which can be associated with (6.3), see Figure 9.

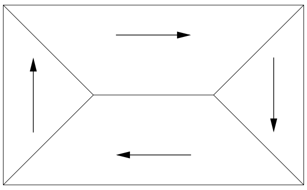

Figure 9: The Landau state

Notice that the first condition in (6.1), when interpreted in the distributional sense, implies that the normal component of m' does not jump across the one–dimensional discontinuity lines – charge–free walls in the jargon of micromagnetics. As usual in the study of transition layers, we assume that the mesoscopic discontinuity lines are straight. In view of the above, straight discontinuity lines are characterized by a single (nonoriented) angle $2\theta_\infty \geq 0$, which is the angle between the constant magnetization to the left and to the right, see Figure 10. In the sequel, we will always denote by x_1 and x_2 the in–plane variables normal and tangential, respectively, to the straight wall.

6.2 Néel vs. asymmetric Bloch wall

In this subsection, we present the two basic wall types in soft ferromagnetic films. On a microscopic level, a straight discontinuity line is replaced by a smooth transition layer. We assume that the magnetization is independent of the tangential in–plane variable x_2, but we do a priori allow for a dependence on the out–of–plane variable x_3. Hence the considered class of admissible magnetizations is given by

$$m \;=\; m(x_1, x_3) \in \mathbb{S}^2 \tag{6.4}$$

with

$$\lim_{x_1 \uparrow \pm\infty} m \;=\; (\cos\theta_\infty, \pm\sin\theta_\infty, 0). \tag{6.5}$$

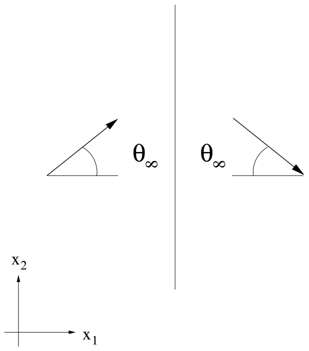

Figure 10: The wall angle θ_∞

It is well known in the applied literature that there are two basic types of walls in films:

- In thin films, the (symmetric) Néel wall is observed, see [66, Chapter 3.6 (C)]. If the film is sufficiently thin, the internal structure of the wall is subject to the same constraints which are also imposed on the mesoscopic magnetization: Variations in x_3–direction are effectively suppressed by the exchange energy, and the out–of–plane component m_3 is effectively suppressed by the stray–field energy. Hence the magnetization is of the form

  $$m = (m_1(x_1), m_2(x_1), 0), \tag{6.6}$$

  see Figure 11. In view of (6.5), these walls are not charge–free on a *microscopic* level:

  $$\nabla \cdot m \;=\; \frac{dm_1}{dx_1} \not\equiv 0. \tag{6.7}$$

- In thicker films, the asymmetric Bloch wall (and its variant, the asymmetric Néel wall) are observed, see [66, Chapter 3.6 (D)]. Indeed, for sufficiently thick films the volume charges (6.7) lead to a prohibitively large magnetostatic energy. The ordinary Bloch wall, i. e. $m = (\cos\theta_\infty, m_2(x_1), m_3(x_1))$, which has no volume charges, would generate surface charges at $x_3 \in \{0, t\}$. For sufficiently thick films however, the exchange energy leaves enough room to avoid *both* volume and surface charges:

  $$\nabla \cdot m \;=\; 0 \text{ for } x_3 \in (0,t) \quad\text{and}\quad m_3 \;=\; 0 \text{ for } x_3 \in \{0,t\}. \tag{6.8}$$

The nonobvious fact that there exists an m of the form (6.4), which exactly satisfies (6.8) has been discovered in [65], see Figure 12. Simultaneously, numerical simulation in [82] showed that the relaxation of the symmetry assumption (6.6) allows for a considerable reduction of the energy.

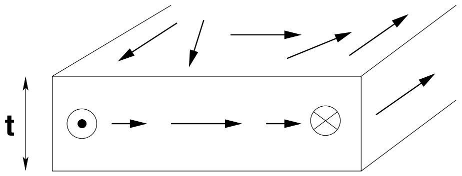

Figure 11: The basic form of a Néel wall

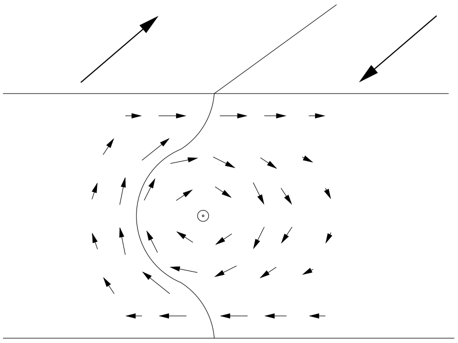

Figure 12: The asymmetric Bloch wall

This distinction of two basic types of mesoscopically one–dimensional transitions is reflected by the scaling of the specific line energy. We will first do this heuristically and then present the corresponding rigorous result [98]. To fix ideas, in this and the next subsection we treat the case of adjacent domains of opposite magnetization, i. e. $\theta_\infty = \frac{\pi}{2}$. For reasons which will be clarified in the sequel we require a small anisotropy $Q \ll 1$ whose easy axis stabilizes the magnetization $(0, \pm 1, 0)$ in the adjacent domains. Hence the relevant specific energy (that is, per length in x_2) for configurations of the form (6.4) is given by

$$\begin{aligned} E_{x_1x_3}(m) &= d^2 \int_{\mathbb{R}\times(0,t)} \left(|\partial_1 m|^2 + |\partial_3 m|^2\right) dx_1 dx_3 \qquad (6.9) \\ &\quad + \int_{\mathbb{R}^2} |\nabla u_m|^2 \, dx_1 dx_3 + Q \int_{\mathbb{R}\times(0,t)} \left(m_1^2 + m_3^2\right) dx_1 dx_3, \end{aligned}$$

where the stray–field $u_m = u_m(x_1, x_3)$ is defined in the usual way, cf (2.16).

Let us first heuristically discuss the case of the asymmetric Bloch wall. Because of the structure assumption (6.8), the magnetostatic contribution to (6.9) drops out. Let us assume that the anisotropy contribution is negligible. Then the remaining variational problem of minimizing the exchange energy among all magnetizations of the form (6.8) has a single length scale, namely, t. Hence, by dimensional analysis, we expect that the wall width w and its specific energy E scale as

$$w_{asymBloch} \sim t \quad \text{and} \quad E_{asymBloch} \sim d^2. \qquad (6.10)$$

In this case, the contribution from anisotropy would scale as $Q\,t^2$, which is indeed small compared to d^2 as long as

$$t^2\, d^{-2} \ll Q^{-1}. \qquad (6.11)$$

This purely dimensional argument, however, does not reveal how the exchange energy (in combination with the constraint (6.8)) manages to localize the transition layer. We will give the argument at the end of this subsection in connection with Theorem 6.1.

Let us now consider the case of a Néel wall. For magnetizations of the form (6.6), the specific energy (6.9) reduces to

$$E_{1d}(m) = d^2 t \int_{\mathbb{R}} |\frac{d}{dx_1} m'|^2 \, dx_1 + \int_{\mathbb{R}^2} |\nabla u_m|^2 \, dx_1 dx_3 + Q\, t \int_{\mathbb{R}} m_1^2 \, dx_1. \qquad (6.12)$$

The stray–field energy term becomes more transparent when considered in Fourier space (k_1 denotes the dual variable to x_1)

$$\int_{\mathbb{R}^2} |\nabla u_m|^2 \, dx_1 dx_3 = t \int_{\mathbb{R}} \left(1 - \frac{\sinh(\frac{1}{2}t|k_1|)}{\frac{1}{2}t|k_1| \, \exp(\frac{1}{2}t|k_1|)}\right) |\mathcal{F}(m_1)|^2 \, dk_1. \qquad (6.13)$$

Note that this is the x_2–independent version of (4.5). Here

$$\mathcal{F}(m_1)(k_1) = \frac{1}{\sqrt{2\pi}} \int_{\mathbb{R}} m_1(x_1) e^{-ik_1x_1} \, dx_1. \qquad (6.14)$$

We note that the Fourier multiplier has a crossover at horizontal wavelengths $\frac{2\pi}{|k_1|}$ of the order of the film thickness t:

$$1-\frac{\sinh(\frac{1}{2}t|k_1|)}{\frac{1}{2}t|k_1|\,\exp(\frac{1}{2}t|k_1|)} \approx \left\{\begin{array}{cl} \frac{1}{2}t|k_1| & \text{for} \quad t|k_1| \ll 1 \\ 1 & \text{for} \quad t|k_1| \gg 1 \end{array}\right\}. \tag{6.15}$$

Since we expect magnetizations of the form (6.6) to occur for sufficiently thin films it is natural to consider the $t|k_1| \ll 1$ approximation to (6.15). This yields

$$\begin{aligned} & E_{1dthin}(m) \qquad\qquad (6.16) \\ = \; & d^2t\int_{\mathbb{R}} |\frac{d}{dx_1}m'|^2\,dx_1 + \frac{t^2}{2}\int_{\mathbb{R}} |k_1||\mathcal{F}(m_1)|^2\,dk_1 + Q\,t\int_{\mathbb{R}} m_1^2\,dx_1 \\ = \; & d^2t\int_{\mathbb{R}} |\frac{d}{dx_1}m'|^2\,dx_1 + \frac{t^2}{2}\int_{\mathbb{R}} \big||\frac{d}{dx_1}|^{1/2}m_1\big|^2\,dx_1 + Q\,t\int_{\mathbb{R}} m_1^2\,dx_1. \end{aligned}$$

Let us make a deliberately naive attempt to guess the scaling of the width w of the Néel wall from (6.16) by a dimensional argument. The exchange energy would scale as $d^2\,t\,w^{-1}$, the anisotropy energy as $Q\,t\,w$, whereas the magnetostatic energy would not depend on w and scale like t^2. Hence, w would, like for the bulk Bloch wall, be determined by the balance of exchange and anisotropy contributions, i.e. $w \sim d\,Q^{-1/2}$, see Subsection 6.8. But, as opposed to bulk Bloch walls, the main contribution would come from magnetostatics, since $t^2 \gg Q^{1/2}\,d\,t$ for sufficiently soft materials.

The flaw of this argument lies in the assumption that the Néel wall has a *single* length scale w, when it actually has *two*: a core and a tail width $w_{core} \ll w_{tail}$. Indeed, we think of the Néel wall centered at $x_1 = 0$ as being divided into two portions: a core $|x_1| \lesssim w_{core}$ and two tails $w_{core} \lesssim |x_1| \lesssim w_{tail}$. This two–scale nature allows the Néel wall to decrease its magnetostatic energy by a logarithmic factor. In fact, the scalings of the energy contributions are

$$\begin{array}{ccc} \text{contribution from exchange} & \sim & d^2\,t\,w_{core}^{-1}, \\ \text{contribution from magnetostatics} & \sim & t^2\ln^{-1}\dfrac{w_{tail}}{w_{core}}, \\ \text{contribution from anisotropy} & \sim & Q\,t\,w_{tail}. \end{array} \tag{6.17}$$

The logarithmic scaling of the magnetostatic contribution will be explained in Subsection 6.3. Now, optimizing in w_{tail} and w_{core} yields

$$w_{corethin} \sim d^2\,t^{-1}, \quad w_{tail} \sim Q^{-1}\,t \quad \text{and} \quad E_{Neelthin} \sim t^2\,\ln^{-1}\frac{w_{tail}}{w_{corethin}}. \tag{6.18}$$

For very soft materials like permalloy ($Q \ll 1$), $Q^{-1}\,t$ may be larger than the sample dimension ℓ. In this case w_{tail} has to be estimated by ℓ and thus the specific Néel wall energy scales as

$$E_{Neelthin} \;\sim\; t^2\,\ln^{-1}\frac{\ell t}{d^2}. \tag{6.19}$$

This is the model of what is called the ultrathin Néel wall, see [66, p.243], because it is the appropriate model for very thin films. The core width of the Néel wall in moderately thin films scales as d, as we shall explain in Subsection 6.4. In fact, the scaling (6.18) is only consistent with the thin–film approximation (6.16) provided the smallest length scale, i. e. $w_{corethin}$, is large compared to t, which yields $t \;\ll\; d$. Notice also that the scaling (6.18) is consistent with the assumption that $w_{corethin} \ll w_{tail}$ as long as

$$t^2\,d^{-2} \;\gg\; Q. \tag{6.20}$$

The optimization of (6.18) in w_{tail} and w_{core} also shows that, by a logarithmic factor, the main contribution to the energy scaling comes from the magnetostatic energy. In particular (6.18) shows that the Néel wall not only requires a small–scale cutoff by the exchange energy but also a large–scale cutoff, which in the present case is provided by anisotropy. Only this cutoff limits the tail width w_{tail}.

The heuristics which lead to the energy scaling of asymmetric Bloch and Néel walls have been made rigorous in [98]. The analysis does *not* presuppose the special form (6.6) or (6.8). It thus confirms that there are only these two basic types of mesoscopically one–dimensional transition layers in soft materials – at least in terms of the leading–order scaling of the specific wall energy.

Theorem 6.1 ([98]) *In the regime (6.11) & (6.20) and for* $\theta_\infty = \frac{\pi}{2}$ *in (6.5) we have*

$$\min_{m \text{ satisfies } (6.4)} E_{x_1x_3}(m) \;\sim\; \left\{ \begin{array}{lll} d^2 & \textit{for} & t^2\,d^{-2} \;\geq\; \ln\frac{1}{Q} \\ t^2\,\ln^{-1}\frac{t^2}{Q\,d^2} & \textit{for} & t^2\,d^{-2} \;\leq\; \ln\frac{1}{Q} \end{array} \right\}. \tag{6.21}$$

The notation "$A \sim B$ in the regime (6.11) and (6.20)" means that there exists a universal constant $0 < C < \infty$ such that $\frac{1}{C}\,A \leq B \leq C\,A$ provided $t^2\,d^{-2} \leq \frac{1}{C}\,Q^{-1}$ and $t^2\,d^{-2} \geq C\,Q$. Upper bounds are proved by construction based on the ansatz (6.6), resp. (6.8) and inspired by the physics literature, in particular [65] for (6.8). The main contribution of a mathematically minded analysis is to show that these models cannot be substantially improved, i. e. in terms of scaling. This is done by providing ansatz–free lower bounds.

To give a flavor of a lower bound argument, we show how to obtain the bound $\gtrsim d^2$ for m of the form (6.8). This shows how the exchange energy in combination with (6.8), and the nonconvex constraint $|m|^2 = 1$, manages to stabilize the transition layer. Indeed, the second condition in (6.8) implies

$$\pi^2 \int_{\mathbb{R}\times(0,t)} m_3^2 \, dx_1 dx_3 \;\le\; t^2 \int_{\mathbb{R}\times(0,t)} (\partial_3 m_3)^2 \, dx_1 dx_3. \tag{6.22}$$

Furthermore, (6.8) together with $\theta_\infty = \frac{\pi}{2}$ yields $\int_0^t m_1 \, dx_3 = 0$, which gives

$$\pi^2 \int_{\mathbb{R}\times(0,t)} m_1^2 \, dx_1 dx_3 \;\le\; t^2 \int_{\mathbb{R}\times(0,t)} (\partial_3 m_1)^2 \, dx_1 dx_3. \tag{6.23}$$

Similarly, we have for the vertical average $\bar{m}_2 = \frac{1}{t}\int_0^t m_2 \, dx_3$:

$$\pi^2 \int_{\mathbb{R}\times(0,t)} (m_2 - \bar{m}_2)^2 \, dx_1 dx_3 \;\le\; t^2 \int_{\mathbb{R}\times(0,t)} (\partial_3 m_2)^2 \, dx_1 dx_3. \tag{6.24}$$

Now because of $m_1^2 + m_2^2 + m_3^2 = 1$, (6.22), (6.23) and (6.24) combine to

$$\pi^2 \, t \int_{\mathbb{R}\times(0,t)} (1 - \bar{m}_2^2) \, dx_1 \;\le\; t^2 \int_{\mathbb{R}\times(0,t)} |\partial_3 m|^2 \, dx_1 dx_3. \tag{6.25}$$

On the other hand, we have

$$\begin{aligned} t \int_{\mathbb{R}} \frac{1}{1-\bar{m}_2^2} (\partial_1 \bar{m}_2)^2 \, dx_1 \;&\le\; \int_{\mathbb{R}\times(0,t)} \frac{1}{1-m_2^2} (\partial_1 m_2)^2 \, dx_1 dx_3 \\ &\le\; \int_{\mathbb{R}\times(0,t)} |\partial_1 m|^2 \, dx_1 dx_3, \end{aligned} \tag{6.26}$$

where we again used $m_1^2 + m_2^2 + m_3^2 = 1$. Now (6.25) and (6.26) combine by the Modica–Mortola argument (cf. Subsection 7.2) to give a lower bound:

$$\begin{aligned} & d^2 \int_{\mathbb{R}\times(0,t)} |\partial_1 m|^2 + |\partial_3 m|^2 \, dx_1 dx_3 \\ & \quad \overset{(6.25),(6.26)}{\ge} \quad d^2 \left(t \int_{\mathbb{R}} \frac{1}{1-\bar{m}_2^2} (\partial_1 \bar{m}_2)^2 \, dx_1 + \frac{\pi^2}{t} \int_{\mathbb{R}} (1 - \bar{m}_2^2) \, dx_1 \right) \\ & \quad \ge \quad 2\pi \, d^2 \int_{\mathbb{R}} |\partial_1 \bar{m}_2| \, dx_1 \overset{(6.5)}{\ge} 4\pi \, d^2. \end{aligned}$$

6.3 The logarithmic tails of the Néel wall

It is by now well–established that the tails of a Néel wall decay logarithmically, see [66, Figure 3.76]. However, early treatments based on ansatz functions missed the very slow decay and led to an overestimation of the wall energy, in particular for low anisotropy Q (see e.g. the review article [43], pp. 397–401, where $q = 1/Q$, and [66], p. 242). A first formal asymptotic analysis predicting the logarithmic decay was carried out by Riedel and Seeger [101]; a detailed mathematical discussion and various refinements of their work can be found in the work of Garcia–Cervera [52, 53]. Finally, Melcher [89, 90] recently established the logarithmic behavior of the tails rigorously, see Theorem 6.2 below.

We start by giving a very informal argument in favor of the logarithmic scaling (6.17) of the magnetostatic energy of the Néel wall, as well as in favor of a logarithmic tail in the range $w_{core} \lesssim |x_1| \lesssim w_{tail}$. We notice that due to (6.5) and (6.6), there must be an x_1 such that $|m_1(x_1)| = 1$, which we think of as the center of the wall. By symmetry we may assume $m_1(0) = 1$. On the Fourier side, $m_1(0) = 1$ is expressed as

$$\int_{\mathbb{R}} \mathcal{F}(m_1)\, dk_1 \ = \ \sqrt{2\pi}. \tag{6.27}$$

It helps to think of (6.27) as a constraint on the charge distribution $-\frac{dm_1}{dx_1}$, i. e. as $\int_{-\infty}^{0} \frac{dm_1}{dx_1}\, dx_1 \ = \ -\int_0^{\infty} \frac{dm_1}{dx_1}\, dx_1 \ = \ 1$, rather than on the shape of m itself. Minimizing the thin–film magnetostatic energy $\frac{t^2}{2}\int_{\mathbb{R}} |k_1||\mathcal{F}(m_1)|^2\, dk_1$, subject to the constraint (6.27), yields the optimality condition

$$\mathcal{F}(m_1)(k_1) \ = \ \frac{\sqrt{2\pi}\,\lambda}{|k_1|} \quad \text{for } k_1 \neq 0 \tag{6.28}$$

for some Lagrange multiplier λ. Since the Fourier transform of $-\frac{2}{x_1}$ (in the sense of Cauchy's principal value) is given by $-\sqrt{2\pi}\, i\,\mathrm{sign}(k_1)$, we may regard (6.28) as the Fourier transform of $2\ln\frac{w}{|x_1|}$, where w is some length scale which can be identified with w_{tail}:

$$m_1(x_1) \ = \ 2\lambda\, \ln\frac{w_{tail}}{|x_1|}. \tag{6.29}$$

Note that changes in w_{tail} affect m_1 by an additive constant to which the charge distribution $-\frac{dm_1}{dx_1}$ is oblivious.

If one assumes that most of the volume charges $-\frac{dm_1}{dx_1}$ reside in the tail (this assumption will be questioned in Subsection 6.4), (6.27) turns into

$$\int_{\{w_{tail}^{-1}\lesssim|k_1|\lesssim w_{core}^{-1}\}} \mathcal{F}(m_1)(k_1)\,dk_1 \;\approx\; \sqrt{2\pi}. \tag{6.30}$$

This determines the constant λ in (6.28) asymptotically; we obtain from (6.29):

$$m_1(x_1) \;\approx\; \frac{\ln\frac{w_{tail}}{|x_1|}}{\ln\frac{w_{tail}}{w_{core}}} \qquad \text{for} \quad w_{core} \ll |x_1| \ll w_{tail} \tag{6.31}$$

and from (6.28):

$$\frac{t^2}{2}\int_{\{w_{tail}^{-1}\lesssim|k_1|\lesssim w_{core}^{-1}\}} |k_1||\mathcal{F}(m_1)|^2\,dk_1 \;\approx\; \frac{\pi}{2}\,t^2\,\ln^{-1}\frac{w_{tail}}{w_{core}}. \tag{6.32}$$

The asymptotic formula (6.32) justifies (6.17) and specifies (6.18) to

$$E_{Neelthin} \;\approx\; \frac{\pi}{2}\,t^2\,\ln^{-1}\frac{t^2}{Q\,d^2}. \tag{6.33}$$

This very formal argument has been made rigorous in [89, 90]:

Theorem 6.2 ([90]) *In the regime (6.20) and for $\theta_\infty = \frac{\pi}{2}$ in (6.5) one has*

$$\min_{m\ \textit{satisfies}\ (6.6)} E_{1dthin}(m) \;\approx\; \frac{\pi}{2}\,t^2\,\ln^{-1}\frac{t^2}{Q\,d^2}.$$

Furthermore, for any minimizer, m_1 is symmetric around 0, decreasing on the right half–axis and satisfies

$$m_1(x_1) \sim \frac{\ln\frac{t}{Q\,|x_1|}}{\ln\frac{t^2}{Q\,d^2}} \qquad \textit{for} \qquad d^2t^{-1} \;\ll\; |x_1| \;\ll\; Q^{-1}t.$$

The precise meaning of "$A \approx B$ in the regime (6.20)" is the following: For any $\epsilon > 0$ there exists a $\delta > 0$ such that for $Q \le \delta\,t^2\,d^{-2}$ it holds $1-\epsilon \le \frac{A}{B} \le 1+\epsilon$. Let us give an outline of the approach. One is interested in the tails, which are expected to carry most of the energy. Thus it seems promising to consider the linearization of E_{1dthin} around $m_1 = 0$. The original non–linear character is just preserved in the affine constraint $\int_{-\infty}^0 \frac{dm_1}{dx_1}\,dx_1 = -\int_0^\infty \frac{dm_1}{dx_1}\,dx_1 = 1$ on the charge distribution $-\frac{dm_1}{dx_1}$, which is expressed by

(6.27). The linearized energy $E_{1dthinlin}$ can then be conveniently expressed in Fourier space:

$$\begin{aligned}
&E_{1dthinlin}(m) \\
&\quad = \; d^2 t \int_{\mathbb{R}} \left(\frac{d}{dx_1} m_1 \right)^2 dx_1 + \frac{t^2}{2} \int_{\mathbb{R}} |k_1| |\mathcal{F}(m_1)|^2 \, dk_1 + Q\, t \int_{\mathbb{R}} m_1^2 \, dx_1 \\
&\quad = \; \int_{\mathbb{R}} \left(d^2\, t\, |k_1|^2 + \frac{t^2}{2} |k_1| + Q\, t \right) |\mathcal{F}(m_1)|^2 \, dk_1. \qquad (6.34)
\end{aligned}$$

Now (6.34) is minimized subject to the constraint (6.27). We introduce the rescaling

$$x_1 \;=\; \tfrac{1}{2} Q^{-1}\, t\, \hat{x}_1 \quad \text{and} \quad E_{1dthinlin} \;=\; \tfrac{1}{2} t^2\, \hat{E}_{1dthinlin},$$

and denote by $\hat{\mathcal{F}}$ and $\hat{k}_1$ the Fourier transform and the wave vector after rescaling. The solution is given by

$$\hat{\mathcal{F}}(m_1) \;=\; \frac{\sqrt{2\pi}\lambda}{\epsilon |\hat{k}_1|^2 + |\hat{k}_1| + 1} \quad \text{and} \quad \hat{E}_{1dthinlin} \;=\; 2\pi\lambda \quad \text{with} \quad \epsilon \;=\; 4\, \frac{Q\, d^2}{t^2},$$

where the Lagrange multiplier λ is determined through

$$\lambda^{-1} \;=\; \int_{\mathbb{R}} (\epsilon |\hat{k}_1|^2 + |\hat{k}_1| + 1)^{-1} \, d\hat{k}_1 \;\approx\; 2 \ln \frac{1}{\epsilon}.$$

For $\varepsilon = 0$ the inverse Fourier transform can be carried out explicitly, defining $\hat{m} = \lambda^{-1} m$:

$$\begin{aligned}
\hat{m}_1^0(\hat{x}_1) \;&:=\; \hat{\mathcal{F}}^{-1} \left(\frac{1}{\sqrt{2\pi}(|\hat{k}_1| + 1)} \right) (\hat{x}_1) \\
&=\; \frac{\cos \hat{x}_1}{\pi} \int_{|\hat{x}_1|}^{\infty} \frac{\cos \xi_1}{\xi_1} \, d\xi_1 + \frac{\sin |\hat{x}_1|}{\pi} \int_{|\hat{x}_1|}^{\infty} \frac{\sin \xi_1}{\xi_1} \, d\xi_1, \quad \text{for } \hat{x}_1 \neq 0.
\end{aligned}$$

The function $\hat{m}_1^0$ has the expansions

$$\hat{m}_1^0(\hat{x}_1) \;=\; \frac{1}{\pi} \begin{cases} \ln(1/|\hat{x}_1|) - \gamma + \mathcal{O}(\hat{x}_1) & \text{as } |\hat{x}_1| \ll 1 \\ \hat{x}_1^{-2} + \mathcal{O}(\hat{x}_1^{-4}) & \text{as } |\hat{x}_1| \gg 1 \end{cases}$$

where $\gamma = 0.577\ldots$ is Euler's constant.

This shows that in the region $d^2\, t^{-1} \ll x_1 \ll t\, Q^{-1}$ the optimal profile for the linearized energy $E_{1dlinthin}$ indeed has a logarithmic shape (6.31).

Theorem 6.2 shows that the minimizers of the linearized energy $E_{1dthinlin}$ already capture the correct leading–order asymptotics both for the tails and the minimal energy for E_{1dthin}. In [39, Proposition 2], the correction has been shown to scale as

$$\min_{m \text{ satisfies (6.6)}} E_{1dthin}(m) - \frac{\pi}{2}\, t^2 \ln^{-1} \frac{w_{tail}}{w_{core}} \sim t^2 \left(\ln \ln \frac{w_{tail}}{w_{core}} \right) \ln^{-2} \frac{w_{tail}}{w_{core}}$$

in a slightly different context.

6.4 The core of the Néel wall in moderately thin films

In moderately thin films, the Néel wall has an even more complex structure than the analysis of the previous subsection reveals. We quote from [66, p.243] "In the centre of the wall, the flux into the wall normal direction [i. e. x_1] is ... 1 in reduced units. In the domains this flux is ... $\cos\theta_\infty$. In each half wall the reduced total magnetic charge $\pm(1-\cos\theta_\infty)$ has therefore to be distributed. Part of the charge is concentrated in the core, where it supports a low energy state by close interaction with its counterpart of opposite polarity. This part is limited by the exchange energy, which prevents an arbitrarily narrow core width. The other part of the charge gets widely spread in the tail." We refer to Figure 13. In this subsection we present a rigorous analysis [39], which brings this to the point. We start with the heuristics.

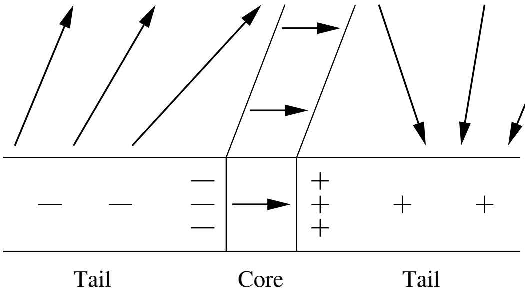

Figure 13: The charge distribution in core and tail

The "close interaction between charges in the core" cannot be captured within the thin–film approximation of the stray–field energy (6.16). As a heuristic, let us replace the Fourier multiplier in (6.13) by its second limiting expression in (6.15), since it is the asymptotic expression for horizontal scales

$\ll t$. For subsequent use, we consider a general wall angle θ_∞ and neglect anisotropy, which is not relevant for the balance in the core. Notice that in this case $m_1 - \cos\theta_\infty$ is the quantity which is square integrable for $|x_1| \to \pm\infty$. Therefore, in (6.13) $\mathcal{F}(m_1)$ has to be replaced by $\mathcal{F}(m_1 - \cos\theta_\infty)$. Hence, E_{1d} is approximated by

$$\begin{aligned} E_{1dthick}(m) &= d^2 t \int_{\mathbb{R}} |\frac{dm'}{dx_1}|^2 \, dx_1 + t \int_{\mathbb{R}} |\mathcal{F}(m_1 - \cos\theta_\infty)|^2 \, dk_1 \\ &= d^2 t \int_{\mathbb{R}} |\frac{dm'}{dx_1}|^2 \, dx_1 + t \int_{\mathbb{R}} (m_1 - \cos\theta_\infty)^2 \, dx_1. \end{aligned}$$

It is convenient to express $E_{1dthick}$ in terms of the local angle, $m' = (\cos\theta, \sin\theta)$:

$$E_{1dthick}(m) \;=\; d^2 t \int_{\mathbb{R}} \left(\frac{d\theta}{dx_1}\right)^2 dx_1 + t \int_{\mathbb{R}} (\cos\theta - \cos\theta_\infty)^2 \, dx_1. \quad (6.35)$$

This standard variational problem has — up to translation – a unique minimizer for the boundary conditions (6.5). A dimensional argument shows that the width of the transition layer scales as

$$w_{corethick} \;\sim\; d. \quad (6.36)$$

The energy of the optimal transition layer can be computed explicitly:

$$E_{Neelthick} \;=\; 2\,d\,t \int_{-\theta_\infty}^{\theta_\infty} (\cos\theta - \cos\theta_\infty)\, d\theta \;=\; 4\,d\,t\,(\sin\theta_\infty - \theta_\infty \cos\theta_\infty). \quad (6.37)$$

Hence $E_{1dthick}(m)$ indeed models the competition of magnetostatics and exchange in the Néel wall core as described in the quotation. This is consistent as long as the core width is small compared with t, i. e.

$$d \;\ll\; t, \quad (6.38)$$

so that the approximation of the Fourier multiplier (6.15) leading to (6.35) is justified. On the other hand, the magnetostatic part of E_{1dthin} models the spreading of charges into logarithmic tails, as we have seen in Subsection 6.3.

Let us now address the optimal mix suggested in the quotation and envision a Néel wall profile $m' = (\cos\theta, \sin\theta)$ with $\theta_\infty = \frac{\pi}{2}$ and center at $x_1 = 0$. We think of the profile as being divided into a core governed by $E_{1dthick}(m)$ and tails governed by $E_{1dthin}(m)$. The core extends over $|\theta| \le$

θ_{core} and the tails over the region described by $|\theta| \geq |\theta_{core}|$ and $|x_1| \lesssim w_{tail}$. Observe that core and tails not only live in different parts of physical space but also in different parts of frequency space: In view of (6.36), the core has a peaked frequency spectrum around $|k_1| \sim d^{-1}$ whereas the tail has a spread–out frequency spectrum, cf. (6.28). This justifies thinking of the energy as the *sum* of the energies of core and tail.

The energy of the optimal core is given by (6.37) with θ_∞ replaced by θ_{core}. The magnetostatic energy of the optimal tail is given by (6.32), but with a factor of $\cos^2\theta_{core}$. Indeed, the right tail has only to accommodate the charges $-\frac{dm_1}{dx_1}$ coming from the rotation from $m_1 = \cos\theta_{core}$ to $m_1 = 0$ (instead of the rotation from $m_1 = 1$ to $m_1 = 0$ considered in Subsection 6.3). This means that in the informal discussion at the beginning of Subsection 6.3, the constraint (6.27) has to be replaced by $\int_{\mathbb{R}} \mathcal{F}(m_1)\, dk_1 = \sqrt{2\pi}\cos\theta_{core}$. The square in $\cos^2\theta_{core}$ is a consequence of the fact that the magnetostatic energy is quadratic in m_1, cf. (6.32). We summarize these findings:

$$\begin{array}{rcc} \text{contribution from core} & \approx & 4\,d\,t\,(\sin\theta_{core} - \theta_{core}\cos\theta_{core}), \\ \text{contribution from tail} & \approx & \frac{\pi}{2}\,t^2\,(\ln^{-1}\frac{w_{tail}}{w_{core}})\,\cos^2\theta_{core}, \\ \text{contribution from anisotropy} & \sim & Q\,t\,w_{tail}. \end{array} \tag{6.39}$$

We allow ourselves to be noncommittal about w_{core} since it only appears in the logarithm; to fix ideas we take $w_{core} = d \sim w_{corethick}$. Now the quotation suggests that the optimal Néel wall profile is obtained by optimizing the sum of (6.39) in θ_{core} and w_{tail} (as opposed to w_{core} and w_{tail} for the ultrathin Néel wall, see (6.17)).

This somewhat bold optimization principle has been made rigorous for a special case in [39]. It treats the case where the length w_{tail} of the Néel wall tails is not implicitly determined by the balance of magnetostatics and anisotropy as in (6.18), but is imposed by boundary conditions:

$$m \;=\; (0, \pm 1, 0) \quad \text{for} \quad \pm\, x_1 \geq w_{tail}. \tag{6.40}$$

The condition (6.40) models the confinement of the Néel wall tails by sample edges or neighboring Néel walls. The result of [39] is also restricted to the limiting regime where the core energy dominates the tail energy, i. e.

$$d\,t^{-1}\,\ln\frac{w_{tail}}{d} \;\ll\; 1 \quad \text{with the understanding that} \quad d \ll w_{tail}. \tag{6.41}$$

Notice that this contains (6.38). In the regime (6.41), the optimization principle in θ_{core} based on (6.39) yields

$$\theta_{core} \;\approx\; \frac{\pi}{2} - 2\,d\,t^{-1}\,\ln\frac{w_{tail}}{d} \quad \text{and} \quad E_{Neelmix} \;\approx\; 4\,d\,t - 2\pi\,d^2\,\ln\frac{w_{tail}}{d}.$$

This is exactly what can be proved using the *original* magnetostatic energy in E_{1d}.

Theorem 6.3 ([39]) *Let $Q = 0$. In the regime (6.41) and $t \ll w_{tail}$, we have*

$$\min_{m \text{ satisfies } (6.6) \text{ and } (6.40)} E_{1d} \;\approx\; 4\,d\,t - 2\pi\, d^2 \ln \frac{w_{tail}}{d}. \qquad (6.42)$$

The precise meaning of the notation of Theorem 6.3 is the following: For any $\epsilon > 0$ there exists a $\delta > 0$ such that if $d \le \delta w_{tail}$, $dt^{-1} \ln \frac{w_{tail}}{d} \le \delta$ and $t \le \delta\, w_{tail}$, one has

$$|\frac{1}{dt} \min E_{1d} - 4 + 2\pi dt^{-1} \ln \frac{w_{tail}}{d}| \le \epsilon\, dt^{-1} \ln \frac{w_{tail}}{d}.$$

The statement in [39, Theorem 1] has an additional factor of two, since it considers the case of an array of winding Néel walls at distance w_{tail} and computes the energy of a pair of walls. The proof is based on a perturbation analysis around the well–characterized minimizer of (6.35). It uses the variational structure and, amongst others, the fact that E_{1d}, when expressed in terms of m_1 alone:

$$E_{1d}(m) \;=\; d^2 t \int_{\mathbb{R}} \frac{1}{1-m_1^2} (\frac{d}{dx_1} m_1)^2\, dx_1 + \int_{\mathbb{R}^2} |\nabla u_m|^2\, dx_1 dx_3 + Q\, t \int_{\mathbb{R}} m_1^2\, dx_1,$$

is nonlinear but *convex* in m_1.

The comparison of (6.37) for $\theta_\infty = \frac{\pi}{2}$ with (6.42) quantifies how the spreading of charges into the tails reduces the total wall energy. It can be seen from (6.42) that this effect decreases as the confinement length w_{tail} of the tails is decreased: $\frac{\partial E_{Neelmix}}{\partial w_{tail}} < 0$. It can also be read off that the relative importance of the repulsive term decreases with increasing thickness: $-\frac{\partial E_{Neelmix}}{\partial w_{tail}} / E_{Neelmix} \approx \frac{\pi}{2}\, d\, t^{-1}\, w_{tail}^{-1}$. This quantifies the repulsion.

It has to be noted, however, that for the full energy $E_{x_1 x_3}$ (i. e. when minimizing over the larger class (6.4)), there is no proper regime where the leading–order energy scales as $d\,t$, as we learn from Theorem 6.1. The scaling in Theorem 6.3 is a consequence of the restriction to magnetizations of the form (6.6). Other restrictions of the magnetization have been considered, for instance that of a bulk Bloch wall symmetry, i. e. $(0, m_2(x_1), m_3(x_1))$. This yields a scaling of the specific wall energy as $d^{4/3}\, t^{2/3}$, see [53, Theorem 7.1].

6.5 The cross–tie wall

Formula (6.37) shows that the core energy of a Néel wall strongly degenerates for small wall angles θ_∞:

$$E_{Neelthick}(\theta_\infty) \;=\; 4\,d\,t\,(\sin\theta_\infty - \theta_\infty\cos\theta_\infty) \;\approx\; \frac{4}{3}\,d\,t\,\theta_\infty^3 \quad \text{for } \theta_\infty \ll 1. \tag{6.43}$$

In particular, a $(\theta_\infty = \frac{\pi}{4})$–wall "costs" only a fraction of a $(\theta_\infty = \frac{\pi}{2})$–wall: $E_{Neelthick}(\frac{\pi}{4}) = \frac{4-\pi}{4\sqrt{2}}\,E_{Neelthick}(\frac{\pi}{2})$, with $\frac{4-\pi}{4\sqrt{2}} \approx 0.152$. In the physics literature, this observation is evoked to explain the occurrence of the cross–tie wall, see Figure 14. The cross–tie wall is a periodic pattern of small–angle Néel walls which macroscopically acts as a $(\theta_\infty = \frac{\pi}{2})$–wall. This pattern is formed by perpendicular Néel wall segments (the "cross–ties") which divide a central wall into segments. In this subsection, we report on a remarkable work by Alouges, Rivière and Serfaty [7], which, based on (6.43), identifies an optimal mesoscopic pattern.

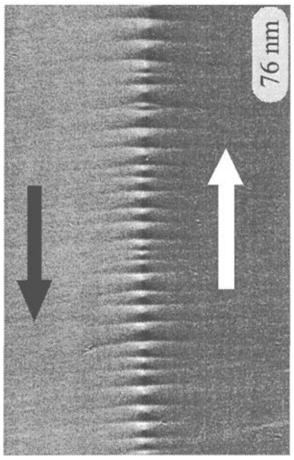

Figure 14: Cross–tie wall in a 76–nm–thick Permalloy film. Reproduced with permission from Hubert and Schäfer, Magnetic Domains, Springer 1998

Motivated by van den Berg's view, cf. Subsection 6.1, all admissible mesoscopic patterns are described by (discontinuous) in–plane magnetizations $m'(x') \in \mathbb{S}^1$ which macroscopically act as a $(\theta_\infty = \frac{\pi}{2})$–wall, which have

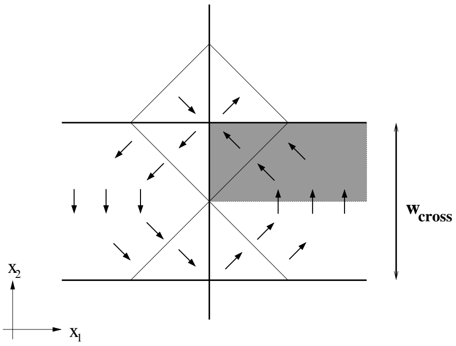

Figure 15: The optimal mesoscopic pattern

some tangential period w_{cross}, and which are weakly divergence–free, i. e.

$$\begin{aligned} \lim_{x_1\to\pm\infty} m' &= (0,\pm 1), \\ m'(x_1, x_2 + w_{cross}) &= m'(x_1, x_2), \\ \nabla' \cdot m' = 0 &\quad \text{distributionally}. \end{aligned} \tag{6.44}$$

We first describe the optimal mesoscopic magnetization m' and its line discontinuities, which are sketched in Figure 15. If $x_1 = 0$ denotes the position of the central discontinuity line, m' obeys the symmetry $(m_1, m_2)(-x_1, x_2) = (m_1, -m_2)(x_1, x_2)$. If $x_2 = 0$ denotes the line half way between two perpendicular discontinuity lines, m' also obeys the symmetry $(m_1, m_2)(x_1, -x_2) = (-m_1, m_2)(x_1, x_2)$. Hence, it suffices to specify m' in $\{x_1 > 0, 0 < x_2 < \frac{w_{cross}}{2}\}$, the shaded region in Figure 15. In this region, the magnetization is continuous (but not differentiable) and given by pasting a vortex–like magnetization to a constant magnetization:

$$m'(x') = \left\{ \begin{array}{cc} (-\frac{x_2}{\sqrt{x_1^2+x_2^2}}, \frac{x_1}{\sqrt{x_1^2+x_2^2}}) & \text{for} \quad x_1 \geq x_2 \\ (-\frac{1}{\sqrt{2}}, \frac{1}{\sqrt{2}}) & \text{for} \quad x_1 \leq x_2 \end{array} \right\}. \tag{6.45}$$

It is easy to check that m' satisfies (6.44). The angle θ_∞ of the line discontinuities cover the range from $\frac{\pi}{4}$ to zero. The line energy per unit length in x_2–direction of this pattern is easily calculated to be (we may set $w_{cross} = 1$)

$$\begin{aligned} E_{crosstie} &= 2\, E_{Neelthick}(\frac{\pi}{4}) + 2\int_{\frac{1}{2}}^{\infty} E_{Neelthick}(\arctan\frac{1}{2x_1})\, dx_1 \\ &= 4\, d\, t\, (\sqrt{2} - 1). \end{aligned} \tag{6.46}$$

Notice that this is indeed smaller than the line energy $E_{Neelthick}(\frac{\pi}{2}) = 4\,d\,t$ of a simple ($\theta_\infty = \frac{\pi}{2}$)–Néel wall. Surprisingly, it can be shown that the value (6.46) is optimal:

Theorem 6.4 ([7]) *It holds*

$$\min_{m \text{ satisfies } (6.44)} \frac{1}{w_{cross}} \int_\Gamma E_{Neelthick}(\theta_\infty)\,ds \;=\; 4\,d\,t\,(\sqrt{2}-1),$$

where Γ *denotes the union of all line discontinuities of* m' *as characterized by the angle* θ_∞ *which varies with arc length* s.

Let us give the concept of the proof. It follows a strategy laid out in [70] for a mathematically related variational problem. This strategy makes use of continuous maps $\Phi'(m') \in \mathbb{R}^2$ with the following two properties:

$$\left\{ \begin{array}{l} \nabla' \cdot \Phi'(m') \;=\; 0 \\ \\ \text{for every } \textit{smooth} \;\; m'(x') \in \mathbb{S}^1 \text{ with } \nabla' \cdot m' = 0, \end{array} \right\} \tag{6.47}$$

and

$$\left\{ \begin{array}{l} |\big(\Phi'(m'_{left}) - \Phi'(m'_{right})\big) \cdot \nu'| \;\le\; E_{Neelthick}(\theta_\infty) \\ \text{for any } m'_{left}, m'_{right} \in \mathbb{S}^1 \text{ which form the angle } \theta_\infty \\ \text{with a normal } \nu' \in \mathbb{S}^1, \text{ see Figure16} \end{array} \right\}. \tag{6.48}$$

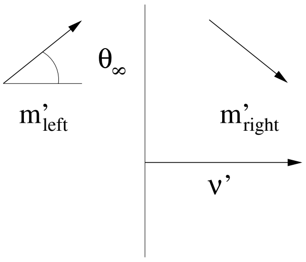

Figure 16: Wall and normal

By the divergence theorem, such a Φ' yields a lower bound independent of m':

$$
\begin{aligned}
&\frac{1}{w_{cross}}\int_\Gamma E_{Neelthick}(\theta_\infty)\,ds\\
&\quad\overset{(6.48)}{\geq}\quad \frac{1}{w_{cross}}\Big|\int_\Gamma\big(\Phi'(m'_{left})-\Phi'(m'_{right})\big)\cdot\nu'\,ds\Big|\\
&\quad=\quad \Big|\frac{1}{w_{cross}}\int_{\mathbb{R}\times(0,w_{cross})}\nabla'\cdot\Phi'(m')\,dx'\\
&\qquad\qquad -\Phi'\big(m'(x_1{=}+\infty)\big)\cdot(1,0)-\Phi'\big(m'(x_1{=}-\infty)\big)\cdot(-1,0)\Big|\\
&\quad\overset{(6.44),(6.47)}{=}\quad \big|\Phi'((0,1))\cdot(1,0)-\Phi'((0,-1))\cdot(-1,0)\big|. \qquad (6.49)
\end{aligned}
$$

In order to yield an optimal lower bound, Φ' must be adapted to the form of $E_{Neelthick}$ (and the conditions imposed at $x_1=\pm\infty$). The choice of Φ' in [7] is guided by

$$\frac{1}{2dt}\tilde{\Phi}'(m') \;=\; \theta\, m'+m'^{\perp} \quad\text{where}\quad m' \;:=\; (\cos\theta,\sin\theta) \qquad (6.50)$$

introduced in [103]. That paper treats the case where m' admits a *global* phase θ. It is not difficult to see that $\tilde{\Phi}'$ satisfies (6.47) and (6.48). But it cannot be used here since there is no global phase θ for the cross–tie pattern (6.45), see also Subsection 6.6. For [7], symmetric variants of the $\tilde{\Phi}'$ in (6.50) are pieced together to form a map $\Phi'(m')$ *continuous* in $m'\in\mathbb{S}^1$:

$$\frac{1}{2dt}\,\Phi'(m') \;=\; \left\{\begin{array}{rll}
\theta\, m'+m'^{\perp}+(0,-\sqrt{2}) & \text{for} & -\frac{\pi}{4}\leq\theta\leq\frac{\pi}{4}\\
(\frac{\pi}{2}-\theta)\,m'-m'^{\perp}+(-\sqrt{2},0) & \text{for} & \frac{\pi}{4}\leq\theta\leq\frac{3\pi}{4}\\
(\theta-\pi)\,m'+m'^{\perp}+(0,\sqrt{2}) & \text{for} & \frac{3\pi}{4}\leq\theta\leq\frac{5\pi}{4}\\
(\frac{3\pi}{2}-\theta)\,m'-m'^{\perp}+(\sqrt{2},0) & \text{for} & \frac{5\pi}{4}\leq\theta\leq\frac{7\pi}{4}
\end{array}\right\}.$$

Using the corresponding property of $\tilde{\Phi}'$, one checks that also Φ' satisfies (6.47) and (6.48). Finally, one easily checks that for this choice of Φ', the right hand side of (6.49) indeed takes the value $4\,d\,t\,(\sqrt{2}-1)$.

6.6 Two–dimensional stability of the Néel wall in very thin films

We return to the ultrathin Néel wall investigated in Subsection 6.2 and 6.3. In this case, the degeneracy in the angle is even more pronounced. Indeed,

$$
\begin{aligned}
E_{Neelthin}(\theta_\infty) \;&=\; \frac{\pi}{2}\,t^2\,(\ln^{-1}\frac{w_{tail}}{w_{core}})\,(1-\cos\theta_\infty)^2\\
&\approx\; \frac{\pi}{8}\,t^2\,(\ln^{-1}\frac{w_{tail}}{w_{core}})\,\theta_\infty^4 \quad \text{for } \theta_\infty\ll 1, \qquad (6.51)
\end{aligned}
$$

cf. the argument which leads to (6.39). So the ultrathin Néel wall should be more prone to the formation of a cross–tie pattern, Figure 15, than the Néel wall in moderately thin films. But in fact, experiments do show stable ($\theta_\infty = \frac{\pi}{2}$)–Néel walls in sufficiently thin films.

We first give the heuristic explanation from the physics literature why the ultrathin Néel wall does not suffer from the cross–tie instability. As we have noted in Subsection 6.5, the optimal mesoscopic cross–tie pattern m', see Figure 15 and formula (6.45), does not allow for a global phase θ. More precisely, there are topological defects residing in the points indicated in Figure 17. The black circles indicate a point singularity with winding number 1, the white circle a point singularity with winding number -1. Analogously to the line singularities, the point singularities are replaced by smooth structures on the microscopic level, the so–called Bloch lines ("line" refers to the x_3–direction). Because of the topological reasons mentioned, these structures require an out–of–plane component m_3. The inner structure of the Bloch line which replaces a white circle is easy, cf. Figure 18: It is the regularization of a vortex, where the magnetization avoids the singularity by turning out of the plane when approaching the center.

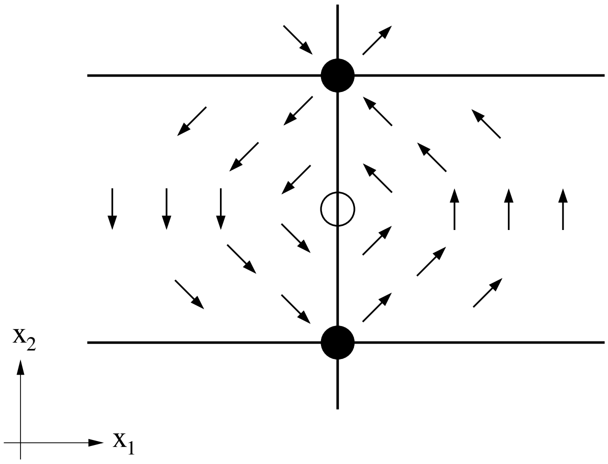

Figure 17: Topological defects in the mesoscopic cross–tie pattern

In [38] the following scaling of the energy for the Bloch line in ultrathin films is heuristically derived:

$$E_{Bloch} \sim d^2 t \ln \frac{w_{cross}}{d},$$

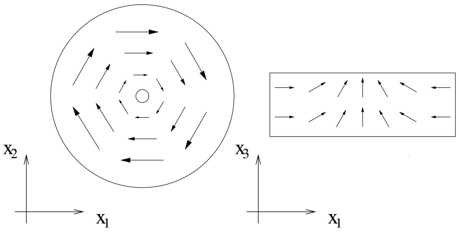

Figure 18: The circular Bloch line

see also Section 7.3. Since the Néel–wall energy tends quadratically to 0 for $t \downarrow 0$, cf. (6.51), the relative cost of Bloch lines increases with decreasing film thickness. This is the common explanation why cross-tie walls are not observed in sufficiently thin films despite the pronounced angle degeneracy, cf. (6.51).

This does not yet explain why the $(\theta_\infty = \frac{\pi}{2})$–Néel wall is stable in very thin films, even if an out–of–plane component is suppressed. This question has been addressed in [42]. There, a class of microscopic *in–plane* magnetizations $m'(x') \in \mathbb{S}^1$, which macroscopically act as a $(\theta_\infty = \frac{\pi}{2})$–wall, and which have some period w in the tangential direction, is considered. The Néel–wall tails are constrained to have the width w_{tail} by a two–dimensional version of (6.40). This amounts to:

$$\begin{aligned} m'(x_1,x_2) &= (0,\pm 1) \quad \text{for } \pm x_1 \geq w_{tail}, \\ m'(x_1,x_2+w) &= m'(x_1,x_2). \end{aligned} \tag{6.52}$$

For this type of m', the three–dimensional energy (per period w in x_2) without anisotropy assumes the form

$$E_{x_1x_2}(m') \;=\; d^2 t \int_{\mathbb{R}\times(0,w)} |\nabla' m'|^2 \, dx' + \int_{\mathbb{R}\times(0,w)\times\mathbb{R}} |\nabla u_m|^2 \, dx,$$

where the the magnetostatic potential $u_m(x_1,x_2,x_3)$ is generated by the volume charge $\nabla' \cdot m'$ in $\{0 < x_3 < t\}$. For sufficiently thin films, this charge distribution is well approximated by the surface charge $-t\,\nabla' \cdot m'$ on

$\{x_3 = 0\}$. This is the thin–film approximation of (4.6) and yields

$$\begin{aligned} & E_{x_1x_2thin}(m') \\ = \; & d^2 t \int_{\mathbb{R}\times(0,w)} |\nabla' m'|^2 \, dx' + \frac{t^2}{2} \int_{\mathbb{R}\times\frac{2\pi}{w}\mathbb{Z}} |k'|^{-1} |\mathcal{F}(\nabla'\cdot m')|^2 \, dk' \\ = \; & d^2 t \int_{\mathbb{R}\times(0,w)} |\nabla' m'|^2 \, dx' + \frac{t^2}{2} \int_{\mathbb{R}\times(0,w)} ||\nabla'|^{-1/2}\nabla'\cdot m'|^2 \, dx'. \end{aligned} \tag{6.53}$$

This is the proper two–dimensional generalization of (6.16) with $Q = 0$. The relevant regime is when the core width of the ultrathin ($\theta_\infty = \frac{\pi}{2}$)–Néel wall, cf. (6.18), is much smaller than the imposed tail width, i. e.

$$d^2 \, t^{-1} \;\ll\; w_{tail}. \tag{6.54}$$

The energy of the ultrathin Néel wall approximately behaves as

$$E_{Neelthin} \;\approx\; \frac{\pi}{2} \, t^2 \, \ln^{-1} \frac{w_{tail}\, t}{d^2},$$

cf. the argument which leads to (6.18). In [42], it is shown that the one–dimensional transition profile is asymptotically optimal under all two–dimensional variations of the type (6.52):

Theorem 6.5 ([42]) *In the regime (6.54),*

$$\min_{m' \text{ satisfies } (6.52)} \frac{1}{w} E_{x_1x_2thin}(m') \;\approx\; \frac{\pi}{2} \, t^2 \, \ln^{-1} \frac{w_{tail}\, t}{d^2}. \tag{6.55}$$

Let us give the concept of the proof. For an arbitrary m' of the form (6.52) there is a curve Γ in $(-w_{tail}, w_{tail}) \times \mathbb{R}$ with

$$\Gamma \text{ is } w\text{–periodic in } x_2 \quad \text{and} \quad m' = \nu' \quad \text{along } \Gamma.$$

One may think of Γ as the wall center, see Figure 19.

The strategy is to show that for length(Γ) (short for length($\Gamma \cap (\mathbb{R} \times (0,w))$))

$$E_{x_1x_2thin}(m') \;\gtrapprox\; \frac{\pi}{2} \, t^2 \, (\ln^{-1} \frac{w_{tail}\, t}{d^2}) \, \text{length}(\Gamma), \tag{6.56}$$

which yields (6.55) because of length(Γ) $\geq w$. This is done by a duality argument based on the charge distribution $-\nabla'\cdot m'$. The charge distribution is tested by the characteristic function ϕ

$$\phi \;=\; -\tfrac{1}{2} \text{ left of } \Gamma \quad \text{and} \quad \phi \;=\; \tfrac{1}{2} \text{ right of } \Gamma,$$

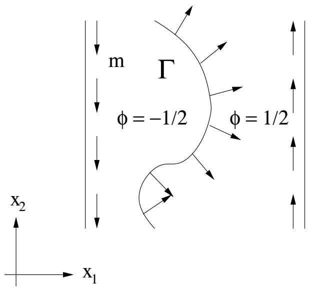

Figure 19: The mesoscopic wall position

see Figure 19. By the construction of Γ, the definition of ϕ and the divergence theorem one has on the one hand

$$\left|\int_{\mathbb{R}\times(0,w)} \nabla'\cdot m'\,\phi\,dx'\right| \;=\; \mathrm{length}(\Gamma).$$

In order to conclude (6.56), one needs, on the other hand, that

$$\begin{aligned}&\left|\int_{\mathbb{R}\times(0,w)} \nabla'\cdot m'\,\phi\,dx'\right|\\ &\quad\le \left(\Big(\frac{2}{\pi}\,t^{-2}\,\ln\frac{w_{tail}\,t}{d^2}\,E_{x_1x_2thin}(m')+o(1)\Big)\mathrm{length}(\Gamma)\right)^{1/2}. \quad (6.57)\end{aligned}$$

This inequality is based on Cauchy–Schwarz in Fourier space

$$\begin{aligned}\int_{\mathbb{R}\times(0,w)} \nabla'\cdot m'\,\phi\,dx' \quad&\le\quad \left(\int_{\mathbb{R}\times\frac{2\pi}{w}\mathbb{Z}} |k'|^{-1}|\mathcal{F}(\nabla'\cdot m')|^2\,dk'\int_{\mathbb{R}\times\frac{2\pi}{w}\mathbb{Z}} |k'||\mathcal{F}(\phi)|^2\,dk'\right)^{1/2}\\ &\overset{(6.53)}{\le}\quad \left(2\,t^{-2}\,E_{x_1x_2thin}(m')\int_{\mathbb{R}\times\frac{2\pi}{w}\mathbb{Z}} |k'||\mathcal{F}(\phi)|^2\,dk'\right)^{1/2},\end{aligned}$$

on the fact that an interpolation estimate of the form

$$\int_{\mathbb{R}\times\frac{2\pi}{w}\mathbb{Z}} |k'||\mathcal{F}(\phi)|^2\,dk' \;\not\lesssim\; \sup_{x'}|\phi|\int_{\mathbb{R}\times(0,w)}|\nabla'\phi|\,dx' \qquad (6.58)$$

just fails logarithmically, and on the obvious identity

$$\sup_{x'}|\phi|\int_{\mathbb{R}\times(0,w)}|\nabla'\phi|\,dx' \;=\; \frac{1}{2}\,\mathrm{length}\;(\Gamma)$$

for our ϕ. The failure of (6.58) is carefully controlled by a cutoff in k'–space and gives rise to the logarithmic scaling including the optimal prefactor in (6.57) via the interpolation estimate

$$\begin{aligned} & \int_{\mathbb{R}\times\frac{2\pi}{w}\mathbb{Z}} \min\{w_{core}\,|k'|^2, |k'|, w_{tail}^{-1}\}|\mathcal{F}(\phi)|^2\,dk' \\ \lessapprox \; & \frac{2}{\pi}\ln\frac{w_{tail}}{w_{core}}\sup_{x'}|\phi|\int_{\mathbb{R}\times(0,w)}|\nabla'\phi|\,dx', \end{aligned} \tag{6.59}$$

which holds for all $w_{core} \ll w_{tail}$ and an arbitrary function ϕ. The main ingredient for (6.59) is the inequality

$$\begin{aligned} \int_{\mathbb{R}\times\frac{2\pi}{w}\mathbb{Z}} 4\,\sin^2(\frac{k'\cdot\delta x'}{2})\,|\mathcal{F}(\phi)|^2\,dk' &= \int_{\mathbb{R}\times(0,w)}(\phi(x'+\delta x')-\phi(x'))^2\,dx' \\ &\leq 2\sup_{x'}|\phi|\int_{\mathbb{R}\times(0,w)}|\delta x'\cdot\nabla'\phi|\,dx' \end{aligned} \tag{6.60}$$

for arbitrary $\delta x' \in \mathbb{R}^2$. This inequality is multiplied with $|\delta x'|^{-3}$ and integrated over the annulus $\{w_{core} \leq |\delta x'| \leq w_{tail}\}$.

6.7 The cross–tie period

We return to the cross–tie wall of Subsection 6.5. The analysis of that subsection does not yield the cross–tie period w_{cross}. Indeed, the variational problem considered in Theorem 6.4 is oblivious to w_{cross}. In this subsection we heuristically address mechanisms which might determine w_{cross}, following [39]. In the physics literature, this is considered an open problem: "An attempt to calculate the equilibrium period of cross–ties has to include the repulsive interaction between the main wall segments and the adjacent cross–ties... . In addition, the extra energy connected ... [with] the Bloch lines has to be considered. No reliable estimates are available for either of these contribution, which means that a consistent theory of the cross–tie wall is still lacking.", cf. [66, p.245].

Let us address the proposed mechanisms. The repulsive interaction between the main wall segments and the adjacent cross–ties results from the following fact: The sense of winding of these Néel walls, cf. Figure 20, is such that their tails compete for space. Since the average distance between the main wall segments and the adjacent cross–ties scales as w_{cross}, we have $w_{tail} \sim w_{cross}$ in the language of Subsection 6.4. As Theorem 6.3 shows for

$(\theta = \frac{\pi}{2})$–walls, the specific wall energy decreases with increasing w_{tail}. The repulsive mechanism due to the Bloch lines is easy to understand: As stated in Subsection 6.6 for very thin films, every Bloch line carries a quantum of energy which only weakly depends on w_{cross}. But the number of Bloch lines per unit length is given by $2\,w_{cross}^{-1}$. There is no ambiguity about the relevant *attractive* mechanism. It is given by an in–plane uniaxial crystalline anisotropy, which favors the magnetization in the domains. Of course, we think of soft materials:

$$Q \ll 1. \tag{6.61}$$

Since there is a band around the central wall segments of width $\sim w_{cross}$, where the magnetization deviates from the easy axis, see Figure 21, anisotropy favors a small w_{cross}.

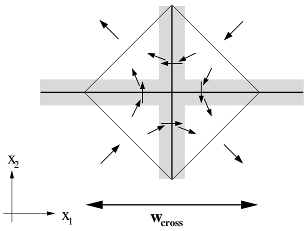

Figure 20: Winding Néel walls in cross–tie

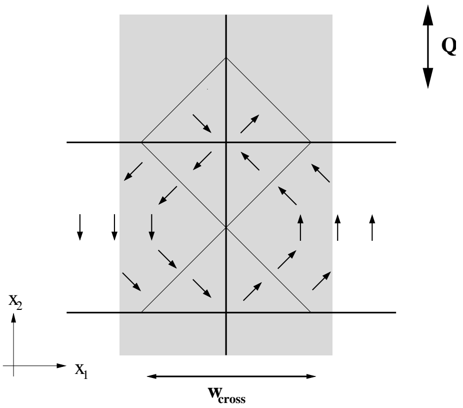

Figure 21: The effect of anisotropy

In order to arrive at a more quantitative picture, we make the following assumption: The dominant energy contribution is the energy of the Néel wall core. According to Subsection 6.5, it completely determines the relative proportions of the optimal mesoscopic pattern, cf. (6.45) and Figure 15, but not its length scale w_{cross}. We now identify the corrections to the energy from anisotropy, Néel–wall interaction and Bloch–line contribution *based on this optimal mesoscopic pattern.* The sum of these expressions will then be minimized in w_{cross}.

Based on (6.45), the contribution from crystalline anisotropy per length in x_2 is easy to quantify:

$$\text{anisotropy per length} \;\approx\; \frac{1}{4}(1+\frac{\pi}{2})\,Q\,t\,w_{cross}. \tag{6.62}$$

In order to assess the contribution of Néel–wall interaction, we need the result of Theorem 6.3 for an arbitrary wall angle θ_∞. Recall the heuristics of Subsection 6.4 on the optimal mix of core and tail in a Néel wall. We are now interested in the case of an arbitrary wall angle θ_∞ and tails limited to a length w_{tail}, cf. (6.40). In this situation, the contribution from the tails in (6.39) has to be replaced by $\frac{\pi}{2}\,t^2\,(\ln^{-1}\frac{w_{tail}}{d})\,(\cos\theta_{core}-\cos\theta_\infty)^2$. Minimization of core and tail contributions in θ_{core} gives the following expression for the specific Néel–wall energy:

$$E_{Neelmix} \;\approx\; 4\,d\,t\,(\sin\theta_\infty-\theta_\infty\,\cos\theta_\infty)-\frac{8}{\pi}\,d^2\,(\ln\frac{w_{tail}}{d})\,\theta_\infty^2 \tag{6.63}$$

in the regime $d \ll w_{tail}$ and $d\,t^{-1}\ln\frac{w_{tail}}{d} \ll 1$, cf. (6.41). The leading term in (6.63) is the expression on which the identification of the optimal mesoscopic pattern was based upon, see (6.43). We are interested in the correction term. It captures the reduction of the specific Néel wall energy coming from spreading a small amount of the Néel wall charge in form of logarithmic tails. More important, it quantifies how this reduction increases with decreasing confinement of the tails. We apply (6.63) to the Néel walls in the optimal mesoscopic pattern. As motivated above, we use $w_{tail} \sim w_{cross}$ (so that $\ln\frac{w_{tail}}{d} \approx \ln\frac{w_{cross}}{d}$) and integrate the correction term along the discontinuity lines of the mesoscopic pattern (with varying $\theta_\infty(s)$). We so obtain the following correction to the total Néel wall energy per length:

$$\begin{aligned}&\text{Correction to total Néel wall energy per length}\\ &\approx\; -d^2\ln\frac{w_{cross}}{d}\,(\pi+0.844\,\frac{8}{\pi}).\end{aligned} \tag{6.64}$$

For the contribution of the Bloch lines, we focus on the simpler circular Bloch line. The circular Bloch line seamlessly extends into the vortex segment of the mesoscopic magnetization, cf. (6.45). By a logarithmic factor, the main contribution to the energy of a Bloch line comes from the exchange energy. We therefore calculate the exchange energy of the vortex segments outside the vortex core and assume that the vortex core size scales as d. Per unit length in x_2 this yields:

$$\text{Total Bloch line energy per length} \;\approx\; \pi\, d^2\, t\, w_{cross}^{-1} \ln \frac{w_{cross}}{d}. \tag{6.65}$$

We now minimize the sum of (6.62), (6.64) and (6.65) in w_{cross}. The minimizer is the solution of

$$0.643\, Q\, t - 5.29\, d^2\, w_{cross}^{-1} - 3.14\, d^2\, t\, w_{cross}^{-2} \ln \frac{w_{cross}}{d} \;\approx\; 0. \tag{6.66}$$

Obviously, there are two regimes:

$$w_{cross} \;\approx\; \left\{ \begin{array}{lll} 8.23\, Q^{-1}\, d^2\, t^{-1} & \text{for} \quad t\, d^{-1} \ll (\frac{1}{Q} \ln^{-1} \frac{1}{Q})^{1/2} & \text{Regime I} \\ 2.21\, (\frac{1}{Q} \ln \frac{1}{Q})^{1/2}\, d & \text{for} \quad t\, d^{-1} \gg (\frac{1}{Q} \ln^{-1} \frac{1}{Q})^{1/2} & \text{Regime II} \end{array} \right\}. \tag{6.67}$$

In the first regime, the dominant repulsive mechanism is the Néel–wall interaction; in the second regime, it is the Bloch–line contribution.

Let us check the consistency of the argument: For (6.64) and (6.65) we need to check $w_{cross} \gg d$ and $dt^{-1} \ln \frac{w_{cross}}{d} \ll 1$. This is consistent provided the film is sufficiently thick, i. e.

$$t\, d^{-1} \;\gg\; \ln \frac{1}{Q}, \tag{6.68}$$

so that Regime I is restricted to the band $\ln \frac{1}{Q} \;\ll\; t\, d^{-1} \;\ll\; (\frac{1}{Q} \ln \frac{1}{Q})^{1/2}$. Notice, however, that in regime (6.68), the asymmetric Bloch wall beats the Néel wall as we learn from Theorem 6.1. Hence, the above analysis only applies to a small range of film thicknesses.

Let us now compare (6.67) with some experimental observations of cross–tie walls. The scaling of w_{cross} with respect to Q was experimentally investigated by Middelhoek in [91] for Permalloy films of thickness $t = 60nm$, for which the effective quality factor was varied through the application of mechanical stresses. The observations show that w_{cross} is proportional to Q^{-1}, which is in agreement with Regime I.

Concerning the dependence on thickness t, we turn to [66, p.449]. We consider Figure 5.59 a) through e), where we read off w_{cross}. To compare

t	w_{cross}^{exp}	w_{cross}^{RegI}	w_{cross}^{RegII}	w_{cross}
10 nm	62.4 μm	82.3 μm	2.01 μm	82.4 μm
30 nm	29.2 μm	27.4 μm	2.01 μm	27.7 μm
40 nm	16.4 μm	20.6 μm	2.01 μm	20.9 μm
60 nm	8.0 μm	13.7 μm	2.01 μm	14.2 μm
76 nm	2.8 μm	10.8 μm	2.01 μm	11.5 μm

Table 4: Comparison of predictions and observations of w_{cross}

these experiments for Permalloy films of varying thickness with the theoretical prediction, we use $d = 5nm$ and $Q = 2.5 \times 10^{-4}$. Hence (6.61) is certainly satisfied while only the thicker films satisfy (6.68). In Table 4, the first column gives the film thickness, the second column the experimental cross–tie period, the third column the prediction based on Regime I, the fourth column the prediction based on Regime II and the fifth column the prediction based on the solution w_{cross} of (6.66). The order of magnitude is certainly well captured by the theoretical model (6.66). It tends to overestimate the repulsive mechanisms, especially for the larger thicknesses. The theoretical model also predicts the right trend in the t–dependence. The comparison of the last three rows shows that the experiments are in a parameter regime where the full theoretical model (6.66) is well approximated by Regime I. Hence the dominant mechanism for these experiments seems to be rather the Néel–wall interaction than the cost of Bloch lines.

Recent observations of cross–tie walls in films of CoFeSiB seem to provide an example of Regime II. The proportionality of w_{cross} to $Q^{-1/2}$ for this set of experiments seems to be well established while the dependence on the thickness is being currently investigated [36].

6.8 Domain branching

In this section, we address thick films with a strong uniaxial perpendicular anisotropy, i. e.

$$Q \gg 1, \tag{6.69}$$

which favors the out–of–plane magnetizations $m = (0, 0, \pm 1)$. It is experimentally well documented and heuristically well understood that this leads to domains with $m \approx (0, 0, \pm 1)$, which branch and thus refine towards the sample edges $\{x_3 = 0, t\}$, see Figure 22. In this section, we present the heuristic arguments, which go back to Lifshitz [84], essentially following Privorotskii [100] and Hubert [64] (see also [66, 3.7.1]). We also present a rigorous scaling analysis of the minimal energy [28, 29], which confirms the heuristics.

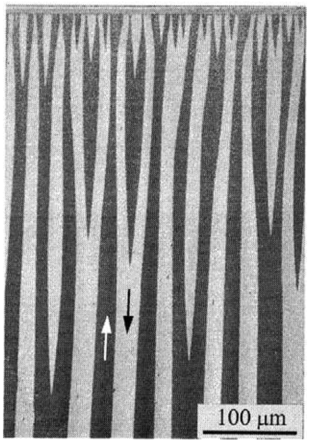

Figure 22: Domain branching in a cobalt crystal. Reproduced with permission from Hubert and Schäfer, Magnetic Domains, Springer 1998

To fix ideas, we impose some period w in the in–plane variables, i. e.

$$m(x_1 + w, x_2, x_3) \ = \ m(x_1, x_2 + w, x_3) \ = \ m(x_1, x_2, x_3),$$

and consider the energy per area w^2:

$$E(m) \ = \ d^2 \int_{(0,w)^2\times(0,t)} |\nabla m|^2 \, dx + \int_{(0,w)^2\times\mathbb{R}} |\nabla u|^2 \, dx + Q \int_{(0,w)^2\times(0,t)} |m'|^2 \, dx.$$

In domains of infinite thickness, the uniform magnetizations $m \equiv (0, 0, 1)$ and $m \equiv (0, 0, -1)$ are the ground states since all energy contributions vanish. In films of a finite thickness, the magnetostatic and the anisotropy contributions to the energy compete: The magnetization favored by anisotropy generates surface charges m_3. But the penalization of surface charges is "soft": Alternating domains with $m = (0, 0, 1)$ and $m = (0, 0, -1)$ (bubble domains) reduce the magnetostatic energy, see Figure 23 for a sketch of the mesoscopic magnetization. This reduction is significant for domain widths ℓ smaller than the thickness, i. e.

$$\ell \ \ll \ t, \tag{6.70}$$

since charge cancellations occur over the distance ℓ. A dimensional argument yields that the magnetostatic energy scales as

$$w^{-2} \times \text{magnetostatic contribution} \;\sim\; \ell. \tag{6.71}$$

On the other hand, these domains require walls. We obviously have

$$w^{-2} \times \text{wall area} \;\approx\; \ell^{-1} t. \tag{6.72}$$

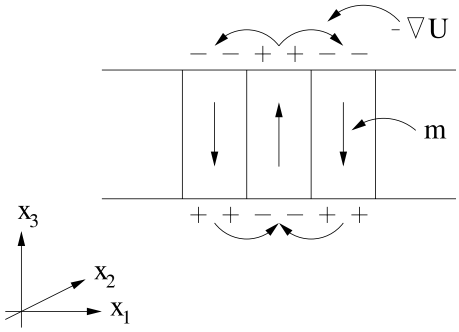

Figure 23: Bubble domains

In order to assess the total wall energy, we need the specific wall energy. For sufficiently thick films, the wall type is that of infinite films: the bulk Bloch wall. It is of the form:

$$m \;=\; m(x_1), \quad m \;=\; (0, m_2, m_3), \quad m \;\to\; (0,0,\pm 1) \;\text{ as }\; x_1 \to \pm\infty$$

and thus does not generate volume charges. Hence, the bulk Bloch wall is stabilized by a balance of exchange and anisotropy energy. The optimal wall profile and the specific wall energy is therefore found by minimizing

$$\begin{aligned} E_{1dbulk}(m) \;&=\; d^2 \int_{\mathbb{R}} |\frac{dm}{dx_1}|^2 \, dx_1 + Q \int_{\mathbb{R}} |m'|^2 \, dx_1 \\ &=\; d^2 \int_{\mathbb{R}} \frac{1}{1-m_3^2} (\frac{dm_3}{dx_1})^2 \, dx_1 + Q \int_{\mathbb{R}} \left(1 - m_3^2\right) \, dx_1. \end{aligned} \tag{6.73}$$

Hence the wall profile is given by $m_3(x_1) = \tanh \frac{x_1}{w_{bulkBloch}}$ with wall width $w_{bulkBloch}$ and wall energy per area defined by

$$w_{bulkBloch} \;=\; Q^{-1/2}\, d, \quad E_{bulkBloch} \;=\; 4\, Q^{1/2}\, d, \tag{6.74}$$

see also Section 7.2.

¿From (6.72) and (6.74) we now deduce

$$w^{-2} \times \text{wall contribution} \;\approx\; Q^{1/2}\, d\, \ell^{-1}\, t. \tag{6.75}$$

Optimizing the sum of (6.71) and (6.75) in ℓ yields the domain width ℓ_{bubble} and total energy in the regime (6.70):

$$\ell_{bubble} \;\sim\; Q^{1/4}\, d^{1/2}\, t^{1/2}, \quad w^{-2}\, E_{bubble} \;\sim\; Q^{1/4}\, d^{1/2}\, t^{1/2}. \tag{6.76}$$

This is self–consistent as long as $t \gg \ell_{bubble} \gg w_{bulkBloch}$, which in view of (6.74) and (6.76) translates into

$$t \;\gg\; Q^{1/2}\, d. \tag{6.77}$$

But precisely in this regime one can do better! Indeed, the magnetostatic energy favors a small domain width ℓ *at the surfaces*, whereas the wall energy favors a large domain width ℓ *in the bulk*. This suggests that the typical domain width ℓ should be larger in the bulk than at the surfaces:

$$t \;\gg\; \ell_{bulk} \;\gg\; \ell_{surface} \;\gg\; w_{bulkBloch}. \tag{6.78}$$

This refinement can be achieved by domain branching, see Figure 24 for a schematic representation of the experimentally observed mesoscopic magnetization. For appropriate refinement, ℓ_{bulk} appears in the wall energy contribution (6.75) but $\ell_{surface}$ in the surface magnetostatic contribution (6.71):

$$\begin{array}{rcc} w^{-2} \times \text{wall contribution} & \sim & Q^{1/2}\, d\, \ell_{bulk}^{-1}\, t, \\ w^{-2} \times \text{surface magnetostatic contribution} & \sim & \ell_{surface}. \end{array} \tag{6.79}$$

However, the mesoscopic structure in Figure 24 is not charge–free in the interior, as indicated in Figure 25. In the regime (6.78), each discontinuity of the mesoscopic pattern carries a surface charge density scaling as $\ell_{bulk}\, t^{-1} \ll 1$. Hence the strength of the demagnetizing field scales as $\ell_{bulk}\, t^{-1}$ so that

$$w^{-2} \times \text{bulk magnetostatic contribution} \;\sim\; \ell_{bulk}^{2}\, t^{-1}. \tag{6.80}$$

The minimization of the sum of (6.79) and (6.80) in ℓ_{bulk} yields

$$\ell_{bulk} \;\sim\; Q^{1/6}\, d^{1/3}\, t^{2/3}. \tag{6.81}$$

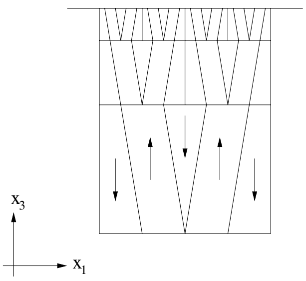

Figure 24: Schematic domain branching

This is consistent with the first condition in (6.78) provided (6.77) is satisfied. We think of the surface width $\ell_{surface}$ to be (at least) so small that the surface magnetostatic contribution is dominated by the bulk magnetostatic contribution. In view of (6.79), (6.80) and (6.81) this means that $\ell_{surface} \ll Q^{1/3}d^{2/3}t^{1/3}$. Notice that in regime (6.77) this necessarily implies $\ell_{surface} \ll w_{bulk}$, the second assumption in (6.78), which thus is consistent. Finally, the third assumption in (6.78) is ensured by (6.69) & (6.77). Hence, we have

$$w^{-2}\,E_{branch} \;\sim\; Q^{1/3}\,d^{2/3}\,t^{1/3}, \tag{6.82}$$

which beats (6.76) in regime (6.77).

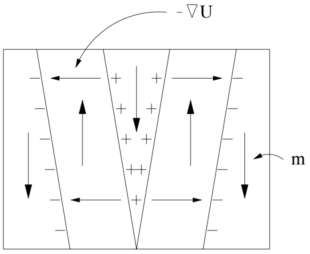

Figure 25: Charges in the bulk

The energy scaling (6.82) has been made rigorous:

Theorem 6.6 ([28, 29]) *In the regime (6.69) & (6.77) we have*

$$w^{-2}\,\min_m E(m) \;\sim\; Q^{1/3}\,d^{2/3}\,t^{1/3}, \tag{6.83}$$

provided $w \gg Q^{1/6}\,d^{1/3}\,t^{2/3}$.

The last condition just ensures that the artificially imposed period w leaves enough room for the bulk domains of width ℓ_{bulk} given by the heuristic discussion, cf. (6.81). Actually, [28, 29] considers a slightly simplified model of E where the exchange energy has been replaced by a term which mimics the wall energy. The analysis in [28, 29] is motivated by the work in [76, 77] on a mathematically similar model for twin branching of martensite near a martensite–austenite interface. A finer analysis of this two–dimensional model, which captures the anisotropic self–similarity of the branched structure near the surface was carried out by Conti [30].

We sketch the argument for the lower bound, which is surprisingly elementary given the complexity of the pattern. At first, one uses the strong crystalline anisotropy to single out the m_3–component:

$$Q^{1/2}\, d \int_{(0,w)^2\times(0,t)} |\nabla m_3|\, dx \;\le\; \frac{1}{2}\, E(m), \tag{6.84}$$

$$\int_{(\frac{2\pi}{w}\mathbb{Z})^2\times\mathbb{R}} \frac{k_3^2}{|k|^2}\, |\mathcal{F}(m_3)|^2\, dk \;\lessapprox\; E(m). \tag{6.85}$$

Inequality (6.84) follows from the standard Modica–Mortola argument, cf. (10.8), i. e.

$$\begin{aligned} &2\, Q^{1/2}\, d \int_{(0,w)^2\times(0,t)} |\nabla m_3|\, dx \\ &\quad\le\; d^2 \int_{(0,w)^2\times(0,t)} \frac{1}{1-m_3^2} |\nabla m_3|^2\, dx + Q \int_{(0,w)^2\times(0,t)} (1-m_3^2)\, dx, \end{aligned}$$

and the second identity of (6.73). The approximate inequality (6.85) follows from a triangle inequality in Fourier space

$$\begin{aligned} &\left(\int_{(\frac{2\pi}{w}\mathbb{Z})^2\times\mathbb{R}} \frac{k_3^2}{|k|^2}\, |\mathcal{F}(m_3)|^2\, dk \right)^{1/2} \\ &\quad\le\; \left(\int_{(\frac{2\pi}{w}\mathbb{Z})^2\times\mathbb{R}} \frac{1}{|k|^2}\, |k\cdot\mathcal{F}(m)|^2\, dk \right)^{1/2} + \left(\int_{(\frac{2\pi}{w}\mathbb{Z})^2\times\mathbb{R}} |\mathcal{F}(m')|^2\, dk \right)^{1/2}. \end{aligned}$$

Notice that the right–hand side is $(\int |\nabla u|^2\, dx)^{1/2} + (\int |m'|^2\, dx)^{1/2}$, so that (6.85) follows from (6.69).

The next step is to factorize in x_3 the left–hand side of (6.84) and (6.85):

$$\int_0^t \Big(Q^{1/2}\, d \int_{(0,w)^2} |\nabla' m_3|\, dx'\Big) dx_3 \;\le\; Q^{1/2}\, d \int_{(0,w)^2\times(0,t)} |\nabla m_3|\, dx, \tag{6.86}$$

$$\int_0^t \Big(\int_{(\frac{2\pi}{w}\mathbb{Z})^2} \frac{1}{1+t^2|k'|^2} |\mathcal{F}'(m_3)|^2\, dk'\Big) dx_3 \;\le\; 2\int_{(\frac{2\pi}{w}\mathbb{Z})^2\times\mathbb{R}} \frac{k_3^2}{|k|^2}\, |\mathcal{F}(m_3)|^2\, dk. \tag{6.87}$$

Inequality (6.86) is obvious. For inequality (6.87) we remark that since m_3 vanishes outside $\{0 < x_3 < t\}$, the left–hand side of (6.87) is identical to

$$\begin{aligned} \frac{1}{2}\int_0^t \int_{(\frac{2\pi}{w}\mathbb{Z})^2} & \frac{1}{1+t^2|k'|^2} \big|\mathcal{F}'(m_3)(k', x_3+t) - \mathcal{F}'(m_3)(k', x_3)\big|^2\, dk'\, dx_3 \\ &= 2\int_{(\frac{2\pi}{w}\mathbb{Z})^2\times\mathbb{R}} \frac{\sin^2(\frac{k_3\, t}{2})}{1+t^2|k'|^2}\, |\mathcal{F}(m_3)|^2\, dk, \end{aligned}$$

so that (6.87) follows from $\frac{\sin^2\left(\frac{k_3 t}{2}\right)}{1+t^2|k'|^2} \le \frac{t^2 k_3^2}{t^2 k_3^2 + t^2|k'|^2}$.

Motivated by the heuristic discussion, we introduce a length scale $\ell_{bulk} \ll t$ and observe that for fixed x_3

$$\int_{\{|k'|\ge \ell_{bulk}^{-1}\}} |\mathcal{F}'(m_3)|^2\, dk' \;\lesssim\; \ell_{bulk} \sup_{x'} |m_3| \int_{(0,w)^2} |\nabla' m_3|\, dx', \tag{6.88}$$

$$\int_{\{|k'|\le \ell_{bulk}^{-1}\}} |\mathcal{F}'(m_3)|^2\, dk' \;\lessapprox\; \ell_{bulk}^{-2}\, t^2 \int_{(\frac{2\pi}{w}\mathbb{Z})^2} \frac{1}{1+t^2|k'|^2}\, |\mathcal{F}'(m_3)|^2\, dk'. \tag{6.89}$$

The approximate inequality (6.89) is obvious for $\ell_{bulk} \ll t$. The ingredient for (6.88) is identical to (6.60):

$$\begin{aligned} &\int_{(\frac{2\pi}{w}\mathbb{Z})^2} 4\, \sin^2\left(\frac{k'\cdot \delta x'}{2}\right) |\mathcal{F}'(m_3)|^2\, dk' \\ &\quad = \int_{(0,w)^2} (m_3(x'+\delta x') - m_3(x'))^2\, dx' \;\le\; 2 \sup_{x'} |m_3| \int_{(0,w)^2} |\delta x' \cdot \nabla' m_3|\, dx'. \end{aligned}$$

This latter inequality has to be averaged over vectors $\delta x'$ of length $|\delta x'| \le \ell_{bulk}$ to obtain (6.88). We notice that (6.88) & (6.89) amount to a slight generalization of the interpolation inequality

$$\int_{(0,w)^2} m_3^2\, dx' \;\lesssim\; \left(\sup_{x'} |m_3| \int_{(0,w)^2} |\nabla' m_3|\, dx'\right)^{2/3} \left(\int_{(0,w)^2} ||\nabla'|^{-1} m_3|^2\, dx'\right)^{1/3},$$

which holds for an arbitrary function m_3.

If we now choose ℓ_{bulk} like in the heuristic argument, cf. (6.81), the estimates (6.84) – (6.89) combine to

$$\begin{aligned} Q^{1/3}\, d^{2/3}\, t^{-2/3} \int_{(0,w)^2\times(0,t)} m_3^2\, dx &= \int_0^t Q^{1/3}\, d^{2/3}\, t^{-2/3} \int_{(\frac{2\pi}{w}\mathbb{Z})^2} |\mathcal{F}'(m_3)|^2\, dk'\, dx_3 \\ &\lesssim E(m). \end{aligned}$$

Together with $Q\int_{(0,w)^2\times(0,t)} |m'|^2\, dx \le E(m)$ this yields the desired lower bound in the regime (6.69) and (6.77).

7 Pattern formation in micromagnetics: mathematical context

The analysis of magnetization patterns and their complex multiscale structure has only recently attracted the broader attention of the mathematics community. There has, however, been a lot of work on related problems (often motivated by questions in geometry), which capture certain crucial aspects of the micromagnetics functional. In this section we discuss three examples: the possible formation of singularities and harmonic maps, the relation between smooth wall profiles and sharp interface theories (such as domain theory), and the role of topological singularities in soft magnetic films.

7.1 Structure of singularities at small scales: Micromagnetics and Harmonic Maps

The different terms in the micromagnetic energy functional

$$E(m) = d^2 \int_\Omega |\nabla m|^2 + Q \int_\Omega \varphi(m) + \int_{\mathbb{R}^3} |\nabla U|^2 - 2 \int_\Omega H_{ext} \cdot m \qquad (7.1)$$

scale differently under a rescaling of the domain. As we already discussed in Section 3, at small scales the highest order term, namely the exchange energy, is the dominant. Hence we expect that this term should control whether singularities (e.g. “Bloch points”) can arise in minimizing magnetization patterns and what their typical structure is.

If we focus only on the exchange energy the minimization problem assumes an extremely simple form:

$$\text{minimize} \quad D(m) = \int_\Omega |\nabla m|^2 \quad \text{subject to } |m| = 1 \qquad (7.2)$$

and to suitable boundary conditions. In other words we seek to minimize the Dirichlet integral $D(m)$ among maps $m : \Omega \subset \mathbb{R}^n \to S^2$. Every minimizer m needs to satisfy the condition

$$\frac{d}{dt}|_{t=0} D\left(\frac{m+\varphi}{|m+\varphi|}\right) = 0 \quad \text{for all } \varphi \in C_0^\infty(\Omega; \mathbb{R}^3), \qquad (7.3)$$

where C_0^∞ denotes the space of smooth maps which vanish in a neighborhood of the boundary $\partial\Omega$. A short calculation shows that this condition is equivalent to the (weak form of) the Euler-Lagrange equations

$$-\Delta m = |\nabla m|^2 m, \qquad (7.4)$$

where $|\nabla m|^2$ can be understood as a Lagrange multiplier arising from the constraint $|m|^2 = 1$. Solutions of this equation are called *harmonic maps.* We say that a harmonic map is *minimizing* if $D((m + \varphi)/|m + \varphi|) \geq D(m)$ for all $\varphi \in C_0^\infty(\Omega; \mathbb{R}^3)$.

The study of harmonic maps and their (possible) singularities has been a central question in geometric analysis for many decades (see [106] for a recent introduction with many further references). In the following we first briefly summarize some of the key results and then discuss their extension to the micromagnetic functional. It turns out that the presence of singularities depends strongly on the dimension n of the domain Ω. For $n = 2$ Morrey showed already in 1948 that minimizing harmonic maps must be smooth. Understanding the situation in higher dimensions was one of the major open question in geometric analysis in the 1960s and 1970s and the problem was finally solved by Schoen and Uhlenbeck. We state their result for the special case $n = 3$.

Theorem 7.1 ([105]) *Let $n = 3$ and let m be a minimizing harmonic map. Then there exists a discrete set S (which may be empty) such that m is smooth in $\Omega \setminus S$.*

A set is discrete if it has no accumulation points in Ω, in particular it can contain at most countably many points. If the boundary of the set Ω is smooth then one can show that m is smooth up to the boundary, with the exception of at most finitely many points.

Singularities can indeed arise. A typical example is given by the map

$$m_0(x) = \frac{x}{|x|}$$

from the three–dimensional unit ball B^3 to its boundary. Indeed, it is easy to see that m_0 solves (7.4). To prove that m_0 is actually minimizing is much more delicate [85, 15]. In the above example the singularity arises for topological reasons. There is no smooth map from B^3 to S^2 which agrees with m_0 on the boundary. There are, however, also examples of singularities in cases were the boundary data are topologically trivial.

The question whether nonminimizing harmonic maps may have singularities remained open even longer. Finally, Hélein [61, 62] showed in 1990 that for $n = 2$ all solutions of (7.4) (with finite energy $D(m)$) are smooth. Shortly afterwards Rivière [102] destroyed all hope for a regularity theory for (7.4) in higher dimension. For $n = 3$ he constructed a harmonic map which is not continuous on any open subset. This led to a new notion of solution, which lies in between harmonic maps and minimizing harmonic maps. We say that a map is *stationary* if it satisfies (7.4) (or, equivalently, (7.3)) and if it is also well behaved with respect to variations of the independent variable, i.e.

$$\frac{d}{dt}_{|t=0} D(m \circ \Phi_t) = 0, \quad \text{for all } \Phi_t = id + t\varphi \quad \text{with } \varphi \in C_0^\infty(\Omega; \mathbb{R}^3), \quad (7.5)$$

where $\circ$ denotes the composition of maps. For those maps Evans established a slightly weaker counterpart of the Schoen-Uhlenbeck result.

Theorem 7.2 ([47]) *Suppose that $n = 3$ and that m is a stationary map. Then there exists a closed subset S such that m is smooth on $\Omega \setminus S$ and such that S has zero one–dimensional Hausdorff measure, $\mathcal{H}^1(S) = 0$.*

This in particular implies that the singular set cannot contain any segment of a line or a smooth curve. In contrast to the result of Schoen and Uhlenbeck the set S here could contain a set of small fractal dimension, e.g. a Cantor subset of a line segment. No such example is known, however.

Now let us turn to micromagnetics. Carbou [23] showed that the above results can be extended to the micromagnetic functional $E(m)$, given by (7.1) (in fact he took H_{ext} = const, but a smooth variable field poses no additional difficulties). Independently, Hardt and Kinderlehrer [60] analyzed the regularity property of minimizing micromagnetic maps. The Euler-Lagrange equation for $E(m)$ is

$$-d^2\Delta m + \frac{1}{2}\nabla\varphi(m) - (H_{ind} + H_{ext}) = (d^2|\nabla m|^2 - (H_{ind} + H_{ext}) \cdot m)m. \quad (7.6)$$

Here $H_{ind} = -\nabla u$ and $\nabla\varphi$ denotes the gradient of φ tangential to S^2. Denoting the left–hand side of (7.6) by H_e (the effective magnetic field acting on Ω), and writing λ for the scalar Lagrange multiplier of m on the right–hand side, we can rewrite the Euler-Lagrange equation as $H_e(x) = \lambda(x)m(x)$ or, equivalently,

$$H_e \wedge m = 0 \quad \text{in } \Omega, \quad (7.7)$$

granting to (7.6) its physical meaning of equilibrium condition for the torques acting on m.

We say that m is a stationary micromagnetic map if, in addition,

$$\frac{d}{dt}_{|t=0} E(m \circ \Phi_t) \quad \text{for all } \Phi_t = id + t\varphi \quad \text{with } \varphi \in C_0^\infty(\Omega; \mathbb{R}^3). \quad (7.8)$$

Finally, we say that m is minimizing if $E((m+\varphi)/|m+\varphi|) \geq E(m)$ for all $\varphi \in C_0^\infty(\Omega;\mathbb{R}^3)$.

Theorem 7.3 ([23]) *Suppose that H_{ext} is smooth.*

(i) If $n=2$ then every solution m of the Euler-Lagrange equation (7.6) *is smooth.*

(ii) Suppose that $n=3$ and that m is a stationary micromagnetic map. Then there exists a closed set S such that m is smooth in $\Omega \setminus S$ and the one–dimensional Hausdorff measure of S is zero, $\mathcal{H}^1(S)=0$.

(iii) Suppose that $n=3$ and m is minimizing. Then there exists a discrete set S such that m is smooth in $\Omega \setminus S$.

Statement (iii) can be refined. Hardt and Kinderlehrer [60] showed that minimizers are smooth up to the boundary (if the boundary is sufficiently smooth) with the exception of a finite set S. Near a singular point a the magnetization approaches the standard singularity $R\frac{x-a}{|x-a|}$, where R is a fixed rotation. Moreover, they derive a universal bound on the number of possible singularities in terms of the applied field, the domain and the anisotropy function. They also show that singularities can indeed arise for smooth applied fields, even for globally minimizing maps m. Examples of concrete physical situations where singularities are expected are reviewed in [66], Section 3.6.5 (D), pp. 268–271. There, one can also find a discussion in how far the (continuum) micromagnetic energy can still be used near a singular point and what modifications of the energy functional might be needed in the immediate vicinity of a singular point.

7.2 Walls vs. sharp interfaces: Modica-Mortola functionals and domain theory

The exchange energy plays very different roles at different length scales. At very small scales ($\ll d$) it determines the presence and structure of possible singularities, as we saw in the previous subsection. At scales comparable to the Bloch–line width d or the Bloch–wall width $d_{BW} = d/\sqrt{Q}$ it determines the inner structure of domain walls. At larger scales the inner structure of the domain walls is not seen, but it is important to keep track of the fact that a domain wall carries a certain energy per unit area. This domain wall energy is crucial in determining patterns at larger scales, as we saw in the discussion on domain branching in Section 6.8. The description of the magnetization pattern in terms of regions of constant magnetizations separated by sharp interfaces carrying a certain energy per unit area is exactly the content of domain theory, which is often used as an approximation of micromagnetics.

In this subsection we discuss how domain theory arises as a rigorous limit of micromagnetics in a specific regime, corresponding in particular to hard materials $Q \gg 1$. The idea that a simplified functional, which allows for sharp domain walls, should lead to the right description of the magnetization patterns on large scales should be applicable in a much broader regime. Mathematically, however, this so far remains an open question, and new tools to capture multiscale behavior might be needed (see e.g. [5]).

The easiest setting to explain the relation between domain walls and sharp–interface theories is that of hard uniaxial material. Macroscopic samples of such materials tend to exhibit complex domain patterns, including very fine magnetic domains. It is not surprising that, historically, the first attempts to understand pattern formation through the competition among the various terms of the energy functional (2.17) have involved cases in which the role of anisotropy is decisive.

Consider, for simplicity, the case $H_{ext} = 0$, and let l be the diameter of Ω. By rescaling Ω to a set ω of unit diameter through the change of variables $x \mapsto \bar{x} = \frac{x}{l} \in \omega$, and suitably normalizing the energy functional (7.1) we obtain

$$i_{\varepsilon,Q}(m) = \varepsilon \int_\omega |\nabla m|^2 + \frac{1}{\varepsilon} \int_\omega \varphi(m) + \frac{1}{Q\varepsilon} \int_{\mathbb{R}^3} |\nabla u|^2, \tag{7.9}$$

where

$$\varepsilon = \frac{d}{lQ^{1/2}} = \frac{d_{BW}}{l}, \tag{7.10}$$

$$u\left(\frac{x}{l}\right) = \frac{1}{l} U(x), \tag{7.11}$$

$$i_{\varepsilon,Q}(m) = \frac{1}{\varepsilon} \quad \frac{I(m)}{l^3} = \frac{1}{\varepsilon} \quad \frac{E(m)}{Ql^3}. \tag{7.12}$$

For a sample that is large enough compared with the intrinsic length scale d_{BW}, i.e.

$$l \gg d_{BW}, \tag{7.13}$$

ε is a small number. It is therefore natural to study $i_{\varepsilon,Q}$ in the limit $\varepsilon \to 0$.

If, in addition, Q is large enough that it makes sense to assume

$$Q\varepsilon = 1 \Longleftrightarrow Q = \left(\frac{l}{d}\right)^2 = \frac{l}{d_{BW}} \gg 1 \tag{7.14}$$

we are naturally led to the study of minimizers of the functional

$$i_\varepsilon(m) = \varepsilon \int_\omega |\nabla m|^2 + \frac{1}{\varepsilon}\int_\omega \varphi(m) + \int_{\mathbb{R}^3} |\nabla u|^2 \tag{7.15}$$

in the limit $\varepsilon \to 0$.

Intuitively, as ε tends to zero the second summand of (7.15) will force minimizers of i_ε to assume only values in $\mathcal{K}$, the zero level set of φ. In the uniaxial case $\mathcal{K}_{uni} = \{\pm e\}$. Then, magnetostatic energy will favor non-uniform, divergence-free patterns (in order to reduce the effect of the charges $m \cdot \nu$ at the boundary of ω). Since $m(x) \in \{\pm e\}$, and since surface discontinuities of m are not allowed by the exchange energy, we expect to see transition layers joining the two values $\pm e$ in a divergence-free fashion. In these layers, $m(x) \notin \mathcal{K}_{uni}$: their thickness is then decided by the competition of anisotropy (which favors thin transition regions and thus high gradients of m) and exchange. This reasoning is precisely the one put forward by Landau and Lifschitz [83]. At least in the case when (7.13) and (7.14) hold, a rigorous mathematical justification of this argument is available. This has been provided in [10], by adapting to the micromagnetic setting an argument due to Modica and Mortola ([93], [92]).

The essence of the argument is that in the limit $\varepsilon \to 0$ minimizers of the functional

$$\varepsilon \int_\omega |\nabla m|^2 + \frac{1}{\varepsilon}\int_\omega \varphi_{uni}(m) \tag{7.16}$$

(possibly subject to suitable boundary conditions or augmented by other lower order terms such as the magnetostatic energy) develop the structure outlined above. They take values very close to the set $\mathcal{K}$, except in an ε neighborhood of certain interfaces. Moreover, in this neighborhood the profile of the minimizer is essentially one–dimensional, varying mainly in the direction normal to the interface. Therefore, the effective energy due to the interface can be determined by solving a one–dimensional optimal profile problem. Performing a further rescaling of length by ε this problem consists in minimizing

$$\int_{-\infty}^{\infty} |\nabla m|^2 + \int_{-\infty}^{\infty} \varphi_{uni}(m) \tag{7.17}$$

among all one–dimensional profiles such that $m(s) \to \pm e$ as $s \to \pm\infty$ (and $|m| = 1$). Using that $\varphi_{uni}(m) = 1 - (m \cdot e)^2$ one can solve the corresponding Euler-Lagrange equation explicitly and one finds that minimizing profiles correspond to suitably parametrized great circles on S^2. The optimal wall energy turns out to be 4 in this dimensionless formulation. In the physical domain Ω the typical scale of the wall profile is the Bloch wall width

$$d_{BW} = \varepsilon L = \sqrt{\frac{A}{K_a}} \tag{7.18}$$

and its energy per unit area given by

$$4\frac{K_a l^3 \varepsilon}{l^2} = 4\sqrt{AK_a}. \tag{7.19}$$

If we also consider the magnetostatic energy, then interfaces whose normal ν is perpendicular to e play a special role. A sharp jump from e to $-e$ at such an interface gives zero contribution to the distributional divergence $\operatorname{div} m$ and hence does not lead to additional magnetostatic energy. If we replace the sharp jump by a transition profile, then there is a distinguished wall profile, which is optimal for (7.17) and which is in addition divergence free – this is exactly the classical Bloch–wall profile, corresponding to the great circle with $m \cdot \nu = 0$.

Anzellotti, Baldo, and Visintin [10] extended the Modica-Mortola argument to the micromagnetic functional i_ε. The limit functional i_0 allows only for magnetizations $\pm e$, penalizes the interfacial area between these two states by the Bloch wall energy and includes the magnetostatic energy of the magnetization pattern. This is the essence of domain theory, which is often considered as a useful, though only approximately valid, strategy to predict domain patterns. The following proposition shows that domain theory can be deduced from micromagnetics as a suitable limit theory, at least in the case that (7.13) and (7.14) hold.

Proposition 7.4 *As $\varepsilon \to 0$, the functional i_ε Γ-converges in L^1 to*

$$i_0 = \begin{cases} 4\,\mathrm{Per}_\Omega\{m(x) = +e\} + \int_{\mathbb{R}^3} |\nabla u|^2 & \textit{if } m \in BV(\Omega) \textit{ and } m(x) \equiv \pm e, \\ +\infty & \textit{else}, \end{cases}$$

where $\mathrm{Per}_\Omega\{m(x) = +e\}$ measures the area of the interface between the region magnetized according to $+e$ and that magnetized according to $-e$.

Remark 7.5 *In the result above, $BV(\Omega)$ denotes the space of functions with bounded variation (see e.g. [57, 48, 9]). For a function in this space, which* *in addition only takes the values* $+e$ *and* $-e$*, the interface between the regions where each of the two values is taken has finite area (in a suitably generalized sense). As outlined above and argued in more detail in Section 10, the essential part of the result is that, in the limit* $\varepsilon \to 0$*, exchange and anisotropy combine to define the energy per unit area of a domain wall. The additional term* $\int_{\mathbb{R}^3} |\nabla u|^2$ *is a continuous perturbation and it is simply reproduced in the limit (see Proposition 10.4 below and note that* L^1 *and* L^2 *convergence are equivalent since* $|m| = 1$*). By the same reasoning, the argument can be extended to cover the presence of an applied field. There is also an extension to more complex anisotropy energies, such as those appropriate for materials with cubic symmetry.*

The essence of domain theory is the elimination of a length scale (the thickness of domain walls), through the replacement of a transition layer with a sharp interface carrying the same energy. This scheme has a great appeal, and it should have a range of applicability much wider than the rather restrictive material parameter regime encoded in (7.13), (7.14). Clearly, it is essential that all dimensions of the sample should be large compared to d_{BW}, and that the material be sufficiently hard. But it should be possible to relax the assumption $Q \gg 1$, at the cost of having to overcome some technical difficulties. Nevertheless, the result above is important in that it demonstrates the possibility to derive domain theory as a rigorous consequence of micromagnetics.

For soft materials, i.e. $Q < 1$, (7.14) certainly fails. In these cases, we cannot rely on φ to simplify the structure of the problem by allowing only finitely many values of m to compete for a low energy state. In addition, for samples which are small in some dimension (thin films), the calculation proving that the optimal transition layer has the one–dimensional structure of a Bloch wall is no longer justified. In fact, the structure of walls in confined geometries is much richer, but also much more complex, see Section 6 above, [66] and Kléman's review [73] on soft ferromagnetic materials.

7.3 The role of topology: soft films and Ginzburg-Landau vortices

For a very soft ferromagnetic material, $Q \ll 1$, and in the absence of the aligning action of an applied magnetic field, pattern formation is controlled by the competition of magnetostatic and exchange energy. Minimization of the former promotes divergence-free magnetization patterns and, in particular, configurations that are everywhere tangential to the boundary of the sample. In a thin film Ω, with cross-section Ω' perpendicular to the coordinate axis x_3, and neglecting variations of m along the thickness direction (which are strongly disfavored by the exchange energy) this requires $m_3 \equiv 0$, and that the in-plane component m' be tangential to the lateral boundary (see Section 4.1 and Table 3 for a more quantitative discussion).

We are thus led to consider a two–dimensional unit vector field, defined on the cross-section of the film, and everywhere tangential to its boundary. There are, however, no continuous vector fields of this type, and there is no such field with finite exchange energy. In fact, the way the system beats this topological obstruction is by creating a localized region, called a Bloch line, where the magnetization becomes perpendicular to the plane of the cross-section (escape in the third dimension). The section of a Bloch line with the plane of the cross-section is a vortex. Its core size is decided by the competition between magnetostatics (penalizing the surface charges associated with $m_3 \neq 0$, hence favoring a core as narrow as possible) and exchange (which clearly favors a core as spread out as possible).

For a film of thickness t and circular cross section of radius l, assume that the core of a Bloch line is a cylinder $\Omega_r = \Omega'_r \times (0,t)$ of radius r, coaxial with the sample $\Omega_l = \Omega'_l \times (0,t)$. For thin films, it is safe to assume that the magnetization is constant along the thickness direction. The exchange contribution to the energy can be rougly estimated as

$$\begin{aligned} E_{exch} &= d^2 \left(\int_{\Omega_l \setminus \Omega_r} |\nabla m|^2 + \int_{\Omega_r} |\nabla m|^2 \right) \\ &\approx 2\pi d^2 t \ln\left(\frac{l}{r}\right) + \pi d^2 t \\ &\approx 2\pi d^2 t \ln\left(\frac{l}{r}\right) . \end{aligned}$$

The magnetostatic contribution to the energy can be estimated through its leading order term

$$E_{mst} \approx t \int_{\Omega_r} m_3^2 = \pi r^2 t \, .$$

Optimizing $E_{exch} + E_{mst}$ with respect to r shows that the competition between exchange and magnetostatic energies results in Bloch lines of characteristic width $d_{BL} = d$, where

$$d = \left(\frac{A}{K_d}\right)^{\frac{1}{2}} , \tag{7.20}$$

each carrying a characteristic energy of order

$$d^2 t \ln\left(\frac{l}{d}\right), \tag{7.21}$$

where t is the film thickness, and l is the diameter of the cross-section. Since in typical applications $d \ll l$, one is confronted with the problem of studying vortices whose energy (after scaling by d^2t) diverges while their size (relative to that of the sample) tends to zero.

Vortex structures of the type just described are common in other physical systems which have been described using mathematical tools similar to the ones suitable for micromagnetics. Problems associated with topological obstructions are of great mathematical interest, and have received considerable attention in the recent literature. A very well studied example is that of the so called 'Ginzburg-Landau vortices', see e.g. [13, 109, 110]. In two dimensions, this is the problem of minimizing an energy of the type

$$\int_{\Omega'} |\nabla m|^2 + \frac{1}{\epsilon^2}\int_{\Omega'} \left(|m|^2 - 1\right)^2$$

among vector fields in the space

$$\left\{m \in H^1(\Omega') \, : m = m_0 \text{ on } \partial\Omega'\right\}$$

in the limit $\epsilon \to 0$. Here m_0 is a prescribed vector field which has unit length on $\partial\Omega'$.

It is worth emphasizing a key difference between this problem, in which vector fields would be constrained to be tangential to $\partial\Omega'$ by a (hard) boundary condition, with the case of soft magnetic films, where only an energetic penalty against non-tangential vector fields is in action. This results in an interesting qualitative difference for the solutions of the corresponding minimization problems. While Ginzburg-Landau vortices can only appear in the interior of Ω', in the case of soft magnetic films vortices at the boundary of ω' will appear in certain material parameter regimes (see [94, 95, 81] and Section 4.2).

8 Beyond low energy states

8.1 Magnetization reversal in soft films

Hysteresis means that an experimentally observed magnetization depends on the history of the external field. For an external field which varies at a sufficiently slow pace in time, we may think of the observed magnetization as a local minimizer of the micromagnetic energy at any moment. Hence, hysteresis can be related to a complex energy landscape with several local minima whose energy might be far from the global minimum. This complex energy landscape is probed by the external field. In fact, the Stoner–Wohlfarth astroid visualizes this point of view in a very special situation. It is based on the assumption that the sample is so small that the magnetization is spatially uniform at any moment, cf. Proposition 3.1. For somewhat larger samples, this is no longer true even if the remanent states (the local minimizers at zero external field) are almost uniform. This was recently brought to the point in [97] for an ellipsoid of revolution.

For sufficiently strong external fields, the magnetization essentially saturates in (the fixed) direction of the external field. A further increase in the external field strength will not affect the magnetization much. This defines the saturation branch, parametrized by the field strength. Imagine moving down the saturation branch by slowly decreasing the external field strength. Typically, one eventually encounters an instability. This event is termed nucleation and is at the onset of switching, but is not necessarily connected with an irreversible event. Nucleation has been theoretically and numerically investigated for some time, we shall mention some of the pertinent work below.

In this section, we report on a series of mathematical papers [20, 21, 22] on nucleation in elongated thin–film elements. This work is motivated by the ubiquitous concertina pattern in elongated soft thin–film elements, see Figure 26. The concertina pattern is the quasiperiodic pattern which can be seen in the middle of the cross–section; it is framed by two Landau states. Figure 27 gives a sketch of the corresponding domain pattern with charge–free walls. The concertina pattern is experimentally generated in the following way: First, the element is saturated along the long axis, then the external field is slowly reduced, and eventually reversed. For some field strength, the uniform magnetization buckles into the concertina pattern.

Let us give a short summary of this section. In Subsection 8.1.2, we present [20], which proves that there are exactly four regimes of instability in elongated thin–film elements. These regimes are identified in terms of the scaling of the critical field. To our knowledge, the oscillatory buckling regime (Regime III) has not been reported in the physics literature. In Subsection 8.1.3, we present [21], which focuses on Regime III and identifies the asymptotic form of the unstable mode by Γ–convergence of the Hessian. In Subsection 8.1.4, we present [22], which identifies the type of bifurcation in Regime III by Γ–convergence of a nonlinearly renormalized energy.

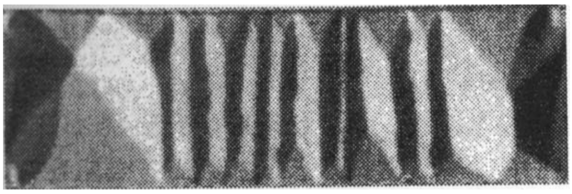

Figure 26: Concertina pattern in a Permalloy film, thickness $t = 300nm$, width $\ell = 18\mu m$. Reproduced with permission from Hubert and Schäfer, Magnetic Domains, Springer 1998

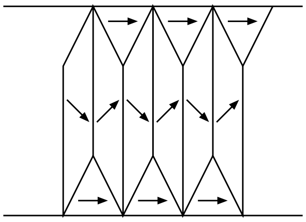

Figure 27: Domains in the concertina pattern of Fig. 26

8.1.1 The setting

An idealized geometry

Motivated by the concertina pattern we consider the following idealized sample geometry

$$\Omega \;=\; \mathbb{R}\times(0,\ell)\times(0,t) \quad \text{with } \; \ell \gg t,$$

see Figure 28. The reasons for this choice are:

- Ω mimics an elongated thin–film element of thickness t and width ℓ. In Section 8.1.4, a finite periodicity L in direction x_1 will be imposed.
- Due to the translation invariance in x_1, Ω admits $m^* = (1,0,0)$ as a stationary point for *all* external fields of the form $H_{ext} = (-h_{ext}, 0, 0)$, $h_{ext} \in \mathbb{R}$ (note the change of sign), and for an easy axis in direction of x_1 or perpendicular to x_1. In fact, we shall neglect crystalline anisotropy altogether without much loss of generality.

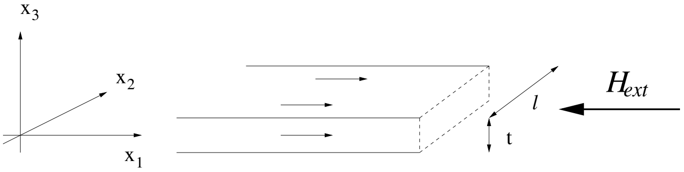

Figure 28: The geometry

The Hessian

The local stability of the stationary point $m^* = (1,0,0)$ is described by the second variation of the energy E, its Hessian. Owing to the constraint $|m|^2 = 1$, infinitesimal perturbations of $m^* = (1,0,0)$ are of the form

$$\delta m \;=\; (0, \delta m_2, \delta m_3), \quad \delta m \;=\; \delta m(x_1, x_2, x_3).$$

The Hessian $\mathrm{Hess}E(m^*)$ in m^* is given by

$$\tfrac{1}{2}\,\mathrm{Hess}E(m^*)(\delta m, \delta m) \;=\; \tfrac{1}{2}\,\mathrm{Hess}E^0(m^*)(\delta m, \delta m) - h_{ext} \int_\Omega |\delta m|^2\, dx, \quad (8.1)$$

where $\mathrm{Hess}E^0(m^*)$ denotes the Hessian without Zeeman term, i. e.

$$\tfrac{1}{2}\,\mathrm{Hess}E^0(m^*)(\delta m, \delta m) \;=\; d^2 \int_\Omega |\nabla\, \delta m|^2\, dx \;+\; \int_{\mathbb{R}^3} |\nabla u_{\delta m}|^2\, dx,$$

and the magnetostatic potential $u_{\delta m}$ is determined by δm in the usual way.

Variational characterization of critical field and unstable modes

The critical field h_{crit} is the value of h_{ext} for which $\mathrm{Hess}E(m^*)$ ceases to be positive definite. The unstable modes are the elements of the degenerate subspace of $\mathrm{Hess}E(m^*)$ at $h_{ext} = h_{crit}$. The following variational characterization of both can be inferred from (8.1): h_{crit} and the (normalized) unstable modes are the minimum and the minimizers, respectively, of the variational problem

$$\tfrac{1}{2}\,\mathrm{Hess}E^0(m^*)(\delta m, \delta m) \qquad \text{subject to} \qquad \int_\Omega |\delta m|^2\, dx \;=\; 1. \tag{8.2}$$

It is natural to capitalize on the translation invariance of (8.2) in x_1 by a partial Fourier transform in that variable. More precisely, the Hessian $\mathrm{Hess}E^0(m^*)(\cdot,\cdot)$ factorizes into $\{\mathrm{Hess}E^0(m^*)(k_1,\cdot,\cdot)\}_{k_1\in\mathbb{R}}$, where

$$\begin{aligned}
&\frac{1}{2}\mathrm{Hess}E^0(m^*)(k_1, \delta m, \delta m)\\
&\quad=\; d^2 \int_{(0,\ell)\times(0,t)} \left(k_1^2\,|\delta m|^2 + |\partial_2\,\delta m|^2 + |\partial_3\,\delta m|^2\right) dx_2 dx_3\\
&\qquad+ \int_{\mathbb{R}^2} \left(k_1^2\,|u_{\delta m}|^2 + |\partial_2\,u_{\delta m}|^2 + |\partial_3\,u_{\delta m}|^2\right) dx_2 dx_3,
\end{aligned} \tag{8.3}$$

k_1 denotes the dual variable to x_1 and $\delta m = \delta m(x_2, x_3)$. Hence, we replace the variational problem (8.2) in $\delta m(x_1, x_2, x_3)$ by the variational problem in $\delta m(x_2, x_3)$ *and* k_1 of minimizing

$$\tfrac{1}{2}\mathrm{Hess}E^0(m^*)(k_1, \delta m, \delta m) \qquad \text{subject to} \qquad \int_{(0,\ell)\times(0,t)} |\delta m|^2\, dx_2 dx_3 \;=\; 1. \tag{8.4}$$

Notice that unstable modes can also be seen as the ground states for the operator

$$\mathcal{L}\,\delta m \;=\; -d^2\triangle_{\mathrm{Neumann}}\delta m - \begin{pmatrix}\partial_2\\ \partial_3\end{pmatrix} u_{\delta m}. \tag{8.5}$$

A complete explicit diagonalization beyond the obvious factorization (8.3) of $\mathcal{L}$ seems not at hand. Indeed, the contribution from the exchange energy is diagonal with respect to cosine *series* in (x_2, x_3) whereas the contribution from the magnetostatic energy is diagonal with respect to the Fourier *transform* in (x_2, x_3). This lack of compatibility reflects the fact that the exchange energy is confined to the sample but the energy of the stray field extends into the ambient space.

Different types of models and modes

Following [1] we distinguish between "models" and "modes". A model is a special ansatz for an infinitesimal perturbation δm. In view of (8.2), it gives an upper bound for h_{crit}. A mode is an eigenfunction of (8.5) – but only the eigenfunction corresponding to the smallest eigenvalue yields h_{crit} and the degenerate subspace.

We now discuss the physics literature. There, besides infinite prisms like our Ω, ellipsoids have been considered, since they also allow for constant stationary states m^*. Brown [16] found two modes for ellipsoids of rotation: The first mode corresponds to a coherent rotation, the second mode corresponds to a curling of the magnetization. The characterizing feature of the curling mode is the complete absence of a stray field, i.e., no surface or volume charges are generated by this mode. Brown also found that for sufficiently small samples (w.r.t. d), the coherent mode has a lower eigenvalue than the curling mode.

In [51], three models are compared for an infinite circular cylinder: Coherent rotation, Brown's curling mode and a model for buckling. It is found that only in a small size range the buckling model beats the two modes. In [3], the infinite cylinder is investigated more systematically: Cylindrical coordinates (x_1, r, ϕ) reduce (8.5) to a one–dimensional problem in r parametrized by $(k_1, n) \in \mathbb{Z} \times \mathbb{R}$. The case $n = 0$ is treated completely, the lowest eigenvalue occurs for $k_1 = 0$ and corresponds to the curling mode. By a lower bound estimate, the cases $n \geq 2$ are discarded for nucleation. The case $n = 1$ is treated numerically, the buckling model of [51] is found to be close to an actual mode.

In [2], an infinite prism with rectangular cross–section is considered. This is the geometry considered here, but in [2], no consideration was given to extreme aspect ratios of the rectangular cross–section, i. e. $t \ll \ell$. Guided by [3], modes and models which vary in the infinite direction x_1 are ignored. Upper and lower bounds for h_{crit} are given.

Based on these works, Aharoni [1, p. 202] emphatically rules out any other type of unstable mode besides coherent rotation, buckling and curling. Moreover, he claims that the buckling mode only plays a minor role [1, pp. 200-202]. We now report on [20], where it is shown that there are exactly *four* different regimes. As we shall discuss, two of these regimes (Regime II and Regime III) are buckling regimes, one of which (Regime III) covers a wide range in parameter space of thin films. Aharoni's analysis misses this regime since, implicitly guided by $t \sim \ell$, it discards modes which vary in the infinite direction x_1.

8.1.2 Identification of four scaling regimes

[20] is a rigorous analysis of the scaling of the critical field h_{crit}. By dimensional analysis, h_{crit} is a function of the non–dimensional parameters $t/d, \ell/d$:

$$h_{crit} \;=\; h_{crit}(t/d, \ell/d). \tag{8.6}$$

[20] identifies all regimes for the scaling of this function.

Theorem 8.1 *For $t \ll \ell$*

$$h_{crit} \;\sim\; \left\{ \begin{array}{cccc} \frac{t}{\ell}\ln\left(\frac{\ell}{t}\right) & \mathit{for} & t \,\le\, \frac{d^2}{\ell}\ln^{-1}\left(\frac{\ell}{d}\right) & \mathit{Regime\ I} \\ \left(\frac{d}{\ell}\right)^2 & \mathit{for} & \frac{d^2}{\ell}\ln^{-1}\left(\frac{\ell}{d}\right) \,\le\, t \,\le\, \frac{d^2}{\ell} & \mathit{Regime\ II} \\ \left(\frac{dt}{\ell^2}\right)^{2/3} & \mathit{for} & \frac{d^2}{\ell} \,\le\, t \,\le\, (d\ell)^{1/2} & \mathit{Regime\ III} \\ \left(\frac{d}{t}\right)^2 & \mathit{for} & (d\ell)^{1/2} \,\le\, t & \mathit{Regime\ IV} \end{array} \right\}. \tag{8.7}$$

As in previous sections, the notation $A \sim B$ means that there exists a universal constant $C < \infty$ with $\frac{1}{C}A \le B \le CA$. Theorem 8.1 can best be visualized in terms of a phase diagram for (8.6) in parameter space, see Figure 29.

It is instructive to confront Theorem 8.1 with Theorem 5.1. The reduced convexified model of Theorem 5.1 implicitly treats the reduced critical field $\frac{\ell}{t}h_{crit}$ as being zero. Theorem 8.1 shows that $\frac{\ell}{t}h_{crit} \ll 1$ is indeed true in the interior of Regimes III and IV which, up to a logarithm, coincide with the regime considered in Theorem 5.1. We notice that Regime III is broad in the sense that it spans a range of film thicknesses t which includes both basic types of walls discussed in Subsection 6.2, cf. Theorem 6.1.

Theorem 8.1 is proved by establishing upper and lower bounds on (8.4), which match in terms of scaling. The upper bounds stem from physically motivated models. The main contribution of a mathematically minded analysis is to show that these models can not be substantially improved, i.e. in terms of scaling. This is done by providing ansatz–free lower bounds, which rely on suitable interpolation inequalities. In this sense the analysis of [20] is half–way between proposing (new) models and identifying ground–state modes.

Heuristic interpretation

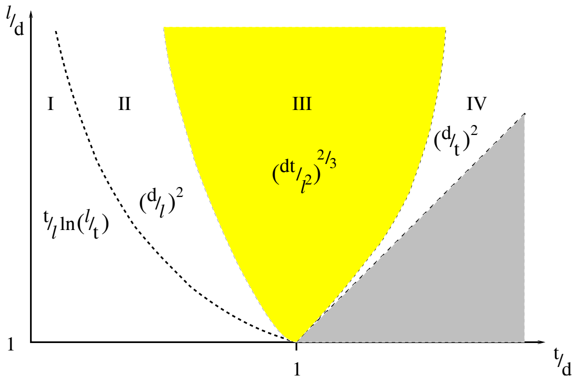

Figure 29: Phase diagram for $h_{crit}(t/d, \ell/d)$

We now interpret Theorem 8.1. This is done by a discussion of the models which lead to the (optimal) upper bounds for (8.2). We go through the four regimes in the order of increasing thickness t (hence from Regime I to Regime IV). The models are determined by a competition between the exchange energy and the magnetostatic energy. With increasing sample size the magnetostatic energy increases in relative importance: Regime I is completely dominated by exchange, Regime IV entirely by magnetostatics. The relative importance of surface charges and volume charges (which are at the origin of the magnetostatic energy) depends on size too: With increasing thickness the volume charges become more important. An interesting feature is dimensional reduction: The model in Regime I is constant, in Regime II it depends on x_2, in Regime III it depends on x_1 and x_2, whereas in Regime IV it depends on x_2 and x_3.

Regime I: Coherent rotation

This regime is driven by the avoidance of an exchange contribution. The exchange energy favors a spatially constant perturbation. But the coherent rotation necessarily creates a non–tangential magnetization at the sample edges $\partial\Omega$, which is penalized by magnetostatics. A coherent rotation in the film plane (the x_1, x_2–plane) only creates surface charges at the small lateral edges $\mathbb{R} \times \{0, \ell\} \times (0, t)$. Hence the model is of the form:

$$\delta m_2 \;\equiv\; (\ell t)^{-1/2}, \quad \delta m_3 \;\equiv\; 0,$$

where the constant $(\ell t)^{-1/2}$ is chosen such that the constraint in (8.4) is satisfied. The corresponding finite perturbation is sketched in Figure 30.

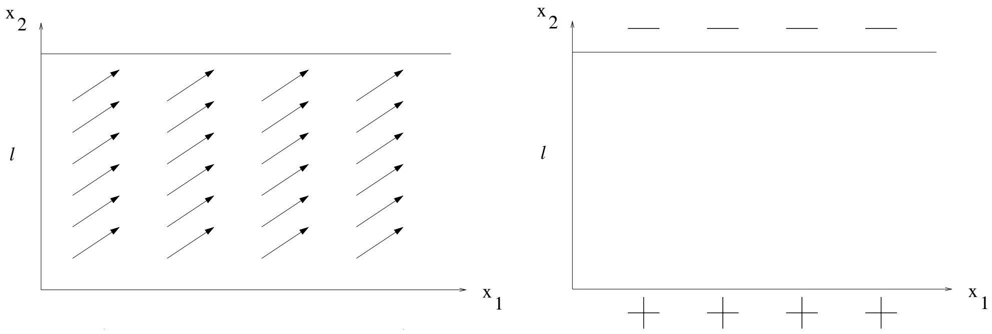

$h_{crit} \sim \frac{t}{\ell} \ln\left(\frac{\ell}{t}\right)$ Surface charges

Figure 30: Coherent rotation

Let us comment on the scaling of h_{crit}. The only contribution to $\mathrm{Hess} E^0(m^*)$ comes from the surface charges. The surface charge at the two lateral edges $\mathbb{R} \times \{0\} \times (0,t)$ and $\mathbb{R} \times \{\ell\} \times (0,t)$ has density $(\ell t)^{-1/2}$ and $-(\ell t)^{-1/2}$, respectively. On length scales larger than t, the surface charge behaves like a *line* charge on $\mathbb{R} \times \{0\} \times \{0\}$ and $\mathbb{R} \times \{\ell\} \times \{0\}$ with density $\ell^{-1/2} t^{1/2}$ and $-\ell^{-1/2} t^{1/2}$, respectively. Hence the magnetostatic contribution per unit length in x_1 scales as

$$\int_{\mathbb{R}^2} |\nabla u_{\delta m}|^2 \, dx_2 dx_3 \;\sim\; (\ln \frac{\ell}{t}) \, (\ell^{-1/2} t^{1/2})^2 \;=\; \frac{t}{\ell} \, \ln \frac{\ell}{t}.$$

The argument of the logarithm is $\frac{\ell}{t}$ since t is the small scale cut–off and ℓ is the large scale cut–off. This yields the scaling of h_{crit}.

Regime II: Nonoscillatory buckling

This regime is driven by the avoidance of surface charges: The magnetostatic influence is already strong enough to suppress any normal component at $\partial\Omega$. The exchange energy is still strong enough to suppress variations in x_1- and x_3-directions. The chosen model is

$$\delta m_2 \;=\; \sqrt{2} (\ell t)^{-1/2} \sin\left(\frac{\pi x_2}{\ell}\right) \quad \text{and} \quad \delta m_3 \;\equiv\; 0. \tag{8.8}$$

Figure 31 shows the corresponding finite perturbation, which displays "Edge–pinning".

Let us again comment on the scaling of h_{crit}. Surface charges are completely suppressed, but there are volume charges:

$$-\nabla \cdot \delta m \;=\; -\partial_2 \, \delta m_2 \;=\; -\sqrt{2} \pi \, \ell^{-3/2} t^{-1/2} \cos(\frac{\pi x_2}{\ell}).$$

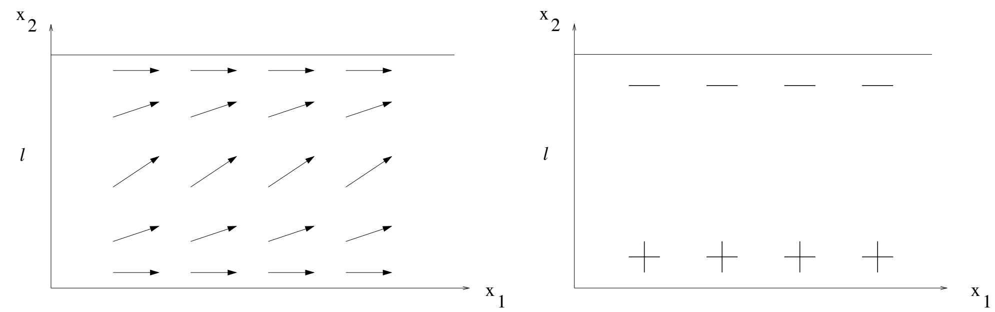

$h_{crit} \sim \left(\frac{d}{\ell}\right)^2$ Volume charges

Figure 31: Nonoscillatory buckling

We assess their contribution: The volume charge density in $\mathbb{R} \times (0, \ell) \times (0, t)$ scales as $\ell^{-3/2} t^{-1/2}$. For $t \ll \ell$, these charges behave like *surface* charges on $\mathbb{R} \times (0, \ell) \times \{0\}$ with a density scaling as $\ell^{-3/2} t^{1/2}$. The energy of a surface charge on $\mathbb{R} \times (0, \ell) \times \{0\}$ with unit density would scale as ℓ^2 (always per unit length in x_1). Hence we obtain for the magnetostatic contribution

$$\int_{\mathbb{R}^2} |\nabla u_{\delta m}|^2 \, dx_2 dx_3 \;\sim\; \ell^2 \, (t^{1/2} \ell^{-3/2})^2 \;=\; \frac{t}{\ell}.$$

On the other hand, the exchange contribution scales as

$$d^2 \int_{(0,\ell)\times(0,t)} |\nabla \delta m|^2 \, dx_2 dx_3 \;\sim\; \left(\frac{d}{\ell}\right)^2.$$

Hence in Regime II (i. e. $t \leq \frac{d^2}{\ell}$), the magnetostatic contribution is dominated by the exchange contribution which sets h_{crit}.

Regime III: Oscillatory buckling

This regime is driven by the competition of volume charges and exchange energy. As in Regime II, surface charges are suppressed at the expense of the exchange energy, which generates volume charges. As opposed to Regime II, volume charges do matter. Volume charges can be reduced by modulating the ansatz (8.8) in the x_1–direction by choosing a non–zero k_1 in (8.4), see Figure 32. If the period $w = \frac{2\pi}{|k_1|}$ of this modulation is much smaller than ℓ, volume charges cancel over a length scale of w instead of ℓ, cf. Figure 32. We choose the following model:

$$\delta m_2 \;=\; 2(\ell t)^{-1/2} \cos(\frac{2\pi x_1}{w}) \, \sin(\frac{\pi x_2}{\ell}) \quad \text{and} \quad \delta m_3 \;\equiv\; 0. \qquad (8.9)$$

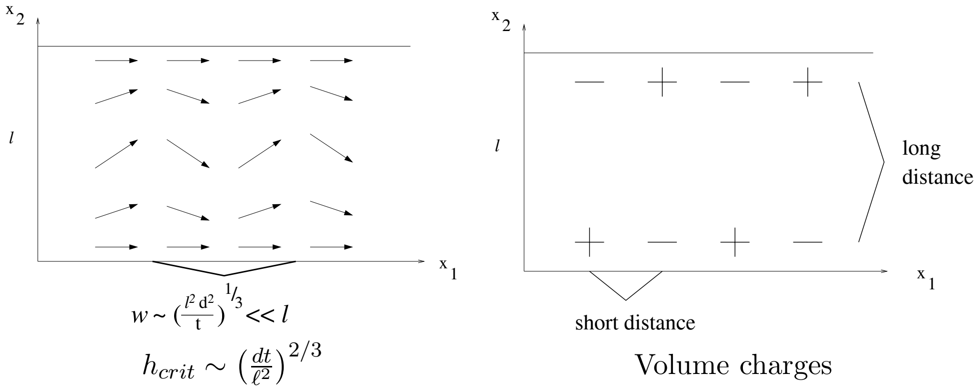

Figure 32: Oscillatory buckling

We now address the scaling of w and h_{crit}. Provided $w \ll \ell$, the dominant part of the exchange energy comes from

$$\partial_1 \delta m_2 \;=\; -4\pi\,(\ell t)^{-1/2} w^{-1}\,\sin\left(\frac{2\pi x_1}{w}\right)\,\sin\left(\frac{\pi x_2}{\ell}\right).$$

Thus the exchange contribution scales as

$$d^2 \int_{(0,\ell)\times(0,t)} |\nabla \delta m|^2\, dx_2 dx_3 \;\sim\; \left(\frac{d}{w}\right)^2. \tag{8.10}$$

The volume charge density in $\mathbb{R}\times(0,\ell)\times(0,t)$ is of the form

$$-\nabla\cdot\delta m \;=\; -\partial_2\,\delta m_2 \;=\; -2\pi\,\ell^{-3/2} t^{-1/2}\,\cos\left(\frac{2\pi x_1}{w}\right)\,\cos\left(\frac{\pi x_2}{\ell}\right).$$

Provided $w \gg t$, this behaves like a *surface* charge density on $\mathbb{R}\times(0,\ell)\times\{0\}$ of the form

$$2\pi\,\ell^{-3/2} t^{1/2}\,\cos\left(\frac{2\pi x_1}{w}\right)\,\cos\left(\frac{\pi x_2}{\ell}\right). \tag{8.11}$$

To leading order in $w \ll \ell$, the magnetostatic potential $u_{\delta m}$ generated by this surface charge density is of the form

$$u_{\delta m} \;\approx\; \frac{1}{2}\,\ell^{-3/2} t^{1/2} w\,\cos\left(\frac{2\pi x_1}{w}\right)\,\cos\left(\frac{\pi x_2}{\ell}\right)\,\exp\left(-\frac{2\pi|x_3|}{w}\right). \tag{8.12}$$

Hence the magnetostatic contribution, which can be computed as the integral of the product of (8.11) and (8.12) over $\mathbb{R}\times(0,\ell)\times\{0\}$, scales as follows:

$$\int_{\mathbb{R}^2} |\nabla u_{\delta m}|^2 \, dx_2 dx_3 \;\sim\; \frac{tw}{\ell^2}. \tag{8.13}$$

We see that the sum of exchange contribution (8.10) and magnetostatic contribution (8.13) is minimized for

$$w \;\sim\; \left(\frac{d^2 \ell^2}{t}\right)^{1/3}. \tag{8.14}$$

For this choice we indeed obtain $h_{crit} \sim \left(\frac{dt}{\ell^2}\right)^{2/3}$. Notice that the consistency condition $t \ll w \ll \ell$ precisely turns into the conditions which define Regime III.

The hypothesis that the experimentally observed period w_{exp} of the concertina pattern is the frozen–in length scale w (8.14) of the unstable mode at critical field is tempting. For a quantitative comparison we need a more quantitative version of (8.14). It will be provided in Subsection 8.1.3.

Regime IV: Curling

This regime is driven by the avoidance of both surface and volume charges. Hence the model δm should be tangential to $\partial\Omega$ and divergence–free in Ω. We make the following choice:

$$\delta m_2 \;=\; 2(\ell t)^{-1/2} \sin(\tfrac{\pi x_2}{\ell}) \cos(\tfrac{\pi x_3}{t}), \delta m_3 \;=\; 2(\ell t)^{-1/2} \, \tfrac{t}{\ell} \cos(\tfrac{\pi x_2}{\ell}) \sin(\tfrac{\pi x_3}{t}) \tag{8.15}$$

The resulting finite perturbations are helicoidal in nature, see Figure 33.

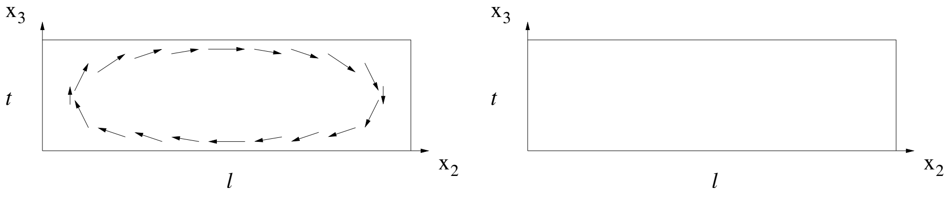

$h_{crit} \sim \left(\frac{d}{t}\right)^2$ Charge-free

Figure 33: Curling

The scaling of h_{crit} is easy to explain: There is no contribution from the magnetostatic energy. In the exchange energy, the contribution from $\partial_3 \, \delta m_2$ is dominant and scales as $(d/t)^2$, which yields the scaling of h_{crit}.

8.1.3 Asymptotic identification of the unstable mode in Regime III

Theorem 8.1 identifies all scaling regimes by determining the scaling of h_{crit}, but it does not determine the degenerate subspace. We now present a result from [21] which rigorously identifies the asymptotic degenerate subspace in the new Regime III. As we shall see, it confirms the heuristic ansatz (8.9) from above.

The scaling

The approach of [21] is to identify the asymptotic minimizers (k_1,$\delta m_2(x_2,x_3)$, $\delta m_3(x_2,x_3)$) by characterizing the Γ–limit of (8.4). For the notion of Γ–limit, see Section 10. This requires a nondimensionalization. (8.14) suggests to measure length anisotropically in the following units

$$x_1 \;=\; \left(\frac{d^2\ell^2}{t}\right)^{1/3}\hat{x}_1, \quad x_2 \;=\; \ell\,\hat{x}_2, \quad x_3 \;=\; t\,\hat{x}_3, \tag{8.16}$$

with the implicit understanding that this also means $k_1 = \left(\frac{t}{d^2\ell^2}\right)^{1/3}\hat{k}_1$, $\partial_2 = \ell^{-1}\hat{\partial}_2$, $dx_2 = \ell\,\hat{dx}_2$ and so on. In view of the constraint in (8.4) we rescale the infinitesimal perturbation as follows

$$\delta m \;=\; (\ell t)^{-1/2}\,\widehat{\delta m}.$$

In view of Theorem 8.1 and $h_{crit} = \frac{1}{2}\,min\,\mathrm{Hess}E^0$, the Hessian itself has to be rescaled as

$$\mathrm{Hess}E^0 \;=\; \left(\frac{dt}{\ell^2}\right)^{2/3}\widehat{\mathrm{Hess}E^0}.$$

We finally introduce the two nondimensional parameters

$$\epsilon \;:=\; \left(\frac{d^2}{\ell t}\right)^{2/3} \quad \text{and} \quad \delta \;:=\; \left(\frac{t^2}{d\ell}\right)^{2/3}, \tag{8.17}$$

which characterize Regime III:

$$\epsilon \;\ll\; 1 \quad \text{and} \quad \delta \;\ll\; 1. \tag{8.18}$$

The result

Theorem 8.2 *The variational problem of minimizing*

$$\tfrac{1}{2}\widehat{\mathrm{Hess}E^0}(m^*)(k_1,\delta m,\delta m) \quad \textit{subject to} \quad \int_{(0,\ell)\times(0,t)} |\delta m|^2 \, dx_2 dx_3 \;=\; 1 \tag{8.19}$$

Γ*–converges in the regime (8.18) under weak convergence of* $(\hat{k}_1, \widehat{\delta m}_2, \widehat{\delta m}_3)$ *in* $\mathbb{R}\times L^2((0,1)\times(0,1))^2$ *to the variational problem of minimizing*

$$\hat{k}_1^2 \int_0^1 (\widehat{\delta m}_2)^2 \, d\hat{x}_2 + \frac{1}{2\,|\hat{k}_1|}\int_0^1 (\hat{\partial}_2\,\widehat{\delta m}_2)^2 \, d\hat{x}_2 \quad \textit{subject to} \quad \int_0^1 |\widehat{\delta m}_2|^2 \, d\hat{x}_2 \;=\; 1 \tag{8.20}$$

if $(\widehat{\delta m}_2, \widehat{\delta m}_3)$ *is of the form* $(\widehat{\delta m}_2(\hat{x}_2), 0)$ *with* $\widehat{\delta m}_2 \in H_0^1((0,1))$*, and* $+\infty$ *if this is not the case.*

Since (8.20) can be solved explicitly, one obtains in the original variables:

Corollary 8.3 *Let* h_{crit} *and* $(k_1, \delta m_2, \delta m_3)$ *be the minimum and a minimizer of (8.4), respectively. In the regime (8.18), we have*

$$\left(\frac{\ell^2}{dt}\right)^{2/3} h_{crit} \;\approx\; 3(\frac{\pi}{2})^{4/3}, \tag{8.21}$$

$$\left(\frac{d^2\ell^2}{t}\right)^{1/3} |k_1| \;\approx\; (\frac{\pi}{2})^{2/3}, \tag{8.22}$$

$$\frac{1}{t\,\ell}\int_{(0,\ell)\times(0,t)} \left|\delta m(x_2,x_3) - \sqrt{2}\,(\sin(\pi\, x_2/\ell),0)\right|^2 dx_2 dx_3 \;\ll\; 1. \tag{8.23}$$

¿From (8.22) and (8.23) we infer that the unstable subspace asymptotically consists of all perturbations δm which are indeed of the form (8.9), where the period $w = \frac{2\pi}{|k_1|}$ of oscillation in the infinite direction x_1 is asymptotically given by

$$w \;\approx\; \left(32\pi\,\frac{d^2\,\ell^2}{t}\right)^{1/3}, \tag{8.24}$$

which specifies (8.14).

We return to the hypothesis that the observed period w_{exp} of the concertina pattern is the frozen–in length scale (8.24) of the unstable mode. We have compared w_{exp} to w for eight experiments pictured in [66]. These experiments cover a substantial range of the non–dimensional parameters t/d and ℓ/d, see Table 5. We find a deviation by a factor $0.5 - 0.7$, which warrants closer investigation in the future.

$\frac{t}{d}$	$\frac{\ell}{d}$	$\frac{w_{exp}}{d}$	$\frac{w_{theo}}{d}$	$\frac{w_{theo}}{w_{exp}}$
8	4000	1200	586	0.49
48	8000	700	512	0.73
60	3600	540	279	0.52
10	2000	500	347	0.69
8	2800	800	462	0.56
8	7000	1700	851	0.50

Table 5: Comparison of predictions and observations of the period of the concertina pattern

The somewhat bold hypothesis that the period of the concertina pattern is the frozen–in length scale of the unstable mode could be easily falsified by a weakly nonlinear analysis: If the phase transition at h_{crit} is of first order (i.e. discontinuous), there is little reason why the unstable mode at h_{crit} should have an influence on the state for $h_{ext} > h_{crit}$. If however the phase transition is of second order (i.e. continuous) this seems more plausible. In the next subsection we shall argue that the phase transition is indeed of second order.

8.1.4 Asymptotic identification of the type of bifurcation

In this section we present [22], in which the type of bifurcation is identified. The factorization (8.3) shows that the unboundedness of the sample in x_1–direction gives rise to a continuous spectrum with a bottom h_{crit} not separated by a spectral gap. In order to avoid the well–known subtleties related to such a situation without destroying the translation invariance in x_1, [22] imposes a convenient finite periodicity L in this direction:

$$m(x_1 + L, x_2, x_3) \;=\; m(x_1, x_2, x_3).$$

This also has the advantage of admitting a well–defined energy functional E (energy over the length of one period):

$$\begin{aligned} E(m) \;&=\; d^2 \int_{(0,L)\times(0,\ell)\times(0,t)} |\nabla m|^2 \, dx + \int_{(0,L)\times\mathbb{R}^2} |\nabla u_m|^2 \, dx \\ &\quad +2h_{ext} \int_{(0,L)\times(0,\ell)\times(0,t)} m_1 \, dx, \end{aligned} \tag{8.25}$$

where u_m inherits the periodicity of m in x_1. We think of the period L as being large compared with the intrinsic w, cf. (8.24).

On a coarse level, one distinguishes between a subcritical, a transcritical and a supercritical bifurcation, see Figure 34 for a sketch. In the subcritical case, there are no local minima close to m^* for $h_{ext} > h_{crit}$. In the transcritical and supercritical case, there are local minima close to m^* for $h_{ext} > h_{crit}$. But, only in the supercritical case, these local minima are "shielded" from much lower energy levels further away (we think for instance of $m = (-1, 0, 0)$) by an energy barrier in the following sense: There exists an open ball B around m^* in m–space such that

$$\begin{gathered} \inf\{\, E(m) \,|\, m \in B \,\} \;<\; \inf\{\, E(m) \,|\, m \in \partial B \,\} \\ \text{for } h_{ext} \text{ sufficiently close to } h_{crit}. \end{gathered} \tag{8.26}$$

Hence the supercritical type can be assimilated to a second–order phase transition whereas the two other types correspond to a first–order phase transition: For the supercritical type, both for conservative and dissipative dynamics, the system will stay close to m^* for a while as h_{ext} increases beyond h_{crit}, provided that the initial kinetic energy was sufficiently small. For the subcritical and the transcritical type, m will suddenly move far away from m^*, at least generically. In this sense, the supercritical type is less dependent on the specific dynamics than the two other types.

The traditional approach to find the type of bifurcation is to expand E, restricted to the degenerate subspace of Hess$E(m^*)$ at the critical field, in terms of $m - m^*$ and $h_{ext} - h_{crit}$. If there is a cubic term in $m - m^*$, the bifurcation is transcritical. If there is no cubic term but a non–degenerate quartic term, the bifurcation is super– or subcritical depending on whether the quartic term is positive or negative definite.

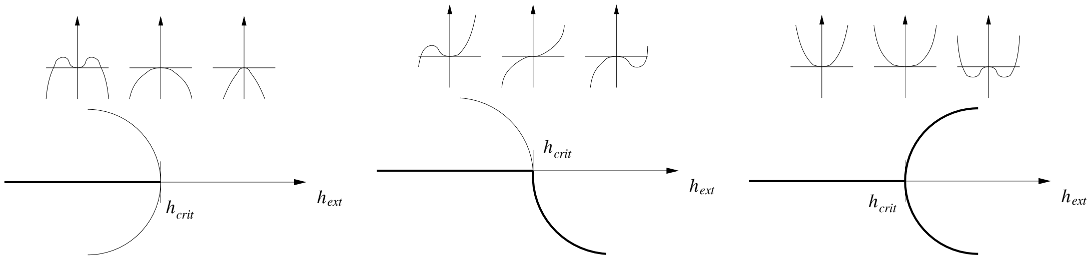

Figure 34: Sub-, trans, and supercritical bifurcation

The traditional approach seems rather delicate for our multiscale environment where one has to combine the asymptotic expansion in $m - m^*$ with the asymptotics of Regime III. [22] argues that the bifurcation is supercritical by directly establishing a quantitative version of (8.26), cf. Corollary 8.6. This is done in two steps:

- In Theorem 8.4, one zooms in on m^* in the energy landscape at the right scale. The zooming–in is combined with the asymptotic Regime III. Again, this is carried out in the framework of Γ–convergence. The Γ–limit only contains quadratic, cubic and quartic terms and can be seen as a normal form of E near m^* in Regime III.
- In Theorem 8.5 it is shown that the Γ–limit is coercive. Roughly speaking, this means that the Γ–limit goes to infinity if the rescaled $m - m^*$ goes to infinity, provided the rescaled $h_{ext} - h_{crit}$ is sufficiently small.

We view this approach as a coarser, but more robust, way of identifying the type of bifurcation. It seems better suited to multi–scale variational problems.

The scaling

Length is nondimensionalized as for Theorem 8.2, i. e. (8.16). The new element is the rescaling of the (m_2, m_3)–components of the magnetization. Notice that for $m \approx m^* = (1,0,0)$, (m_2, m_3) can be seen as the finite version of the infinitesimal perturbation $(\delta m_2, \delta m_3)$. Remark that

$$m_1 \;=\; \sqrt{1 - m_2^2 - m_3^2} \;\approx\; 1 - \tfrac{1}{2}(m_2^2 + m_3^2) \quad \text{for} \quad m \approx (1,0,0).$$

As for Theorem 8.2, we expect that in Regime III, the out–of–plane component is strongly suppressed by the penalization of surface charges so that the above turns into

$$m_1 \;\approx\; 1 - \tfrac{1}{2} m_2^2. \tag{8.27}$$

The magnetization component m_2 will be rescaled in such a way as to balance the two contributions to the volume charge distribution $\nabla \cdot m$, i. e.

$$\partial_1 m_1 \overset{(8.16),(8.27)}{\approx} -\left(\frac{t}{d^2\ell^2}\right)^{1/3} \hat\partial_1\left(\tfrac{1}{2} m_2^2\right) \qquad \text{and} \qquad \partial_2 m_2 \overset{(8.16)}{=} \frac{1}{\ell}\hat\partial_2 m_2.$$

This leads to

$$(m_2, m_3) \;=\; \epsilon^{1/2}\,(\hat m_2, \hat m_3). \tag{8.28}$$

The external field is measured in units of the critical field as identified in Theorem 8.1. As for the energy (8.25) itself, we subtract $E(m^*)$ and normalize appropriately:

$$h_{ext} \;=\; \left(\frac{dt}{\ell^2}\right)^{2/3} \hat{h}_{ext}, \qquad E - 2\,h_{ext}\,L\,\ell\,t \;=\; \left(\frac{d^8 t^2}{\ell}\right)^{1/3} \hat{E}. \tag{8.29}$$

We are now left with four nondimensional parameters, ϵ, δ from (8.17) and also $\hat{L}$ and $\hat{h}_{ext}$. We are interested in Regime III close to critical field. Also, in view of the remark on the spectral gap, we have to assume that the x_1–period L is not too large with respect to the intrinsic period w of oscillation. This translates into

$$\hat{L} \;\sim\; 1 \quad \text{and} \quad \hat{h}_{ext} \;\sim\; 1., \tag{8.30}$$

where according to (8.16), $\hat{L}$ is defined as

$$L \;=\; \left(\frac{d^2\ell^2}{t}\right)^{1/3} \hat{L}.$$

We think of $\hat{L}$ as being large, so that it does not much affect the unstable wavelength $\hat{w} = (32\pi)^{1/3}$, cf. (8.24).

The result

Theorem 8.4 *Fix an $\hat{M} \sim 1$. The variational problem of minimizing*

$$\hat{E} \quad \text{subject to} \quad |m|^2 = 1 \;\; \text{and} \;\; \int_{(0,\hat{L})\times(0,1)\times(0,1)} |m - m^*|^2\, d\hat{x} \;=\; \epsilon \hat{M}^2 \tag{8.31}$$

Γ–converges in the regime described by (8.18) & (8.30) under weak convergence for $(\hat{m}_2, \hat{m}_3)$ in $L^2((0,\hat{L})\times(0,1)\times(0,1))^2$ to the variational problem of minimizing

$$\begin{aligned} \hat{E}_0 \;:=\;& \int_{(0,\hat{L})\times(0,1)} (\hat{\partial}_1 \hat{m}_2)^2\, d\hat{x}' + \tfrac{1}{2} \int_{(0,\hat{L})\times\mathbb{R}} \big||\hat{\partial}_1|^{-1/2}\big(-\hat{\partial}_1(\tfrac{1}{2}\hat{m}_2^2) + \hat{\partial}_2 \hat{m}_2\big)\big|^2\, d\hat{x}' \\ & -\hat{h}_{ext} \int_{(0,\hat{L})\times(0,1)} \hat{m}_2^2\, d\hat{x}' \quad \text{subject to} \quad \int_{(0,\hat{L})\times(0,1)} \hat{m}_2^2\, d\hat{x}' \;=\; \hat{M}^2 \end{aligned} \tag{8.32}$$

if $(\hat{m}_2, \hat{m}_3)$ is of the form $(\hat{m}_2(\hat{x}'), 0)$ and $E_0 = +\infty$ if it is not of this form.

Here $|\hat\partial_1|^{-1/2}$ denotes the operator with Fourier symbol $|\hat k_1|^{-1/2}$. The expression $-\hat\partial_1(\frac{1}{2}\hat m_2^2)+\hat\partial_2\hat m_2$ is to be understood distributionally, where $\hat m_2$ has been extended by zero from $\mathbb{R}\times(0,\ell)$ to $\mathbb{R}\times\mathbb{R}$. As for Theorem 8.2, this imposes edge–pinning, i. e. $\hat m_2(\hat x_2{=}1) = \hat m_2(\hat x_2{=}0) = 0$ in a weak sense.

Let us point out that $\hat E_0$ interpolates between a linear regime and a wall regime, depending on which of the two terms $-\hat\partial_1(\frac{1}{2}\hat m_2^2)$ and $\hat\partial_2\hat m_2$ in the charge distribution is dominant.

- For dominant $\hat\partial_2\hat m_2$, $\hat E_0$ is close to the Γ–limit (8.20) of the Hessian integrated over frequencies $\hat k_1$:

  $$\hat E_0 \;\approx\; \int_{\frac{2\pi}{\hat L}\mathbb{Z}} \left(\hat k_1^2 \int_0^1 \hat m_2^2\, d\hat x_2 + \frac{1}{2|\hat k_1|}\int_0^1 (\hat\partial_2\hat m_2)^2\, d\hat x_2 - \hat h_{ext}\int_0^1 \hat m_2^2\, d\hat x_2 \right) d\hat k_1.$$

- For dominant $-\hat\partial_1(\frac{1}{2}\hat m_2^2)$, $\hat E_0$ is close to a 1–d model for small–angle thin–film Néel walls ("ripples") normal to $\hat x_1$, integrated over $\hat x_2$:

  $$\hat E_0 \;\approx\; \int_0^1 \left(\int_0^{\hat L} (\hat\partial_1\hat m_2)^2\, d\hat x_1 + \frac{1}{2}\int_0^{\hat L} \left||\hat\partial_1|^{1/2}(\tfrac{1}{2}\hat m_2^2)\right|^2 d\hat x_1 - \hat h_{ext}\int_0^{\hat L} \hat m_2^2\, d\hat x_1 \right) d\hat x_2. \tag{8.33}$$

  Indeed, (6.16) with the anisotropy term replaced by the Zeeman term turns into the inner integral of (8.33), when approximated and rescaled according to (8.27), (8.28) and (8.16).

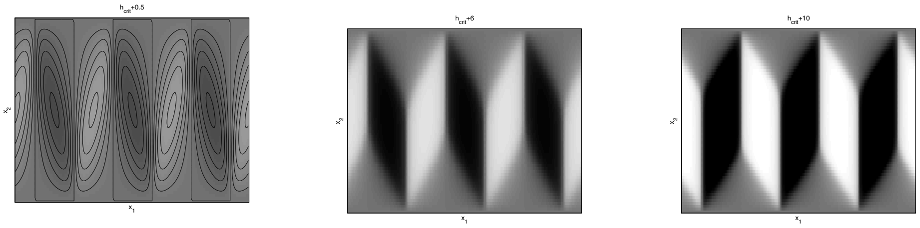

Figure 35: Homotopy between the unstable mode and the concertina pattern

Figure 35 shows the minimizer $\hat m_2$ of $\hat E_0$ for varying strength of the external field $\hat h_{ext}$ ($\hat h_{ext} = \hat h_{crit} + 0.5$, $\hat h_{ext} = \hat h_{crit} + 6$, $\hat h_{ext} = \hat h_{crit} + 10$). The function $\hat m_2$ is represented by a grayscale plot for better comparison with the experimental picture in Figure 26. The proportions correspond to a value of $\varepsilon = 0.008$. One clearly sees a homotopy between the unstable mode and the strongly nonlinear concertina pattern.

Theorem 8.5 shows that $\hat{E}_0$ is coercive for $\hat{L}, \hat{h}_{ext} \sim 1$:

Theorem 8.5 *There exists a universal constant $c > 0$ such that for any $\hat{m}_2 \in L^2((0,\hat{L}) \times (0,1))$ we have*

$$\hat{E}_0(\hat{m}_2) \quad \geq \quad c\,\hat{L}^{-5/3} \left(\int_{(0,\hat{L})\times(0,1)} \hat{m}_2^2 \, d\hat{x}' \right)^{14/9} - \hat{h}_{ext} \int_{(0,\hat{L})\times(0,1)} \hat{m}_2^2 \, d\hat{x}'.$$

It is not claimed that the exponent 14/9 is optimal; it is just important that it is larger than 1. Theorem 8.5 states that there cannot be too much cancellation between the two terms in the charge density. This is not so obvious — the normal form $\hat{E}_0$ for "buckling" in micromagnetics thus behaves quite differently from the normal form for buckling in plate theory, the von Kármán model. Corollary 8.6 draws the conclusion that the bifurcation is supercritical in the sense of (8.26):

Corollary 8.6 *There exists an $\hat{M} \sim 1$ such that in the regime (8.18) & (8.30),*

$$\begin{aligned} &\inf \left\{ E(m) \,\middle|\, \int_{(0,\hat{L})\times(0,1)\times(0,1)} |m - m^*|^2 \, d\hat{x} \leq \epsilon \hat{M}^2 \right\} \\ &\qquad < \inf \left\{ E(m) \,\middle|\, \int_{(0,\hat{L})\times(0,1)\times(0,1)} |m - m^*|^2 \, d\hat{x} = \epsilon \hat{M}^2 \right\}. \end{aligned}$$

8.2 Local minima and thermally-activated switching

The micromagnetic energy is nonconvex due to the restriction $|m| = 1$. It can have many local minima, each representing a stable magnetization pattern. As the applied field varies, a ferromagnet exhibits hysteresis, because the choice of local minimum is history-dependent.

We have discussed the limiting form of the energy in various thin-film regimes. Mathematically speaking, these limiting forms have been justified only for energy minima, i.e. for ground-state patterns. But practically speaking, we expect them to describe the accessible local minima as well. Thus, we expect stable magnetization patterns in thin films to converge to local minima of the appropriate asymptotic energy.

It is natural to seek a more global understanding of the energy landscape. One motivation is the analysis of thermally-activated switching. The Landau-Lifshitz-Gilbert equations of micromagnetic dynamics,

$$J_t = -\gamma J \times \mathbb{H} - \frac{\alpha\gamma}{J_s} J \times (J \times \mathbb{H}) \quad \text{with} \quad \mathbb{H} = -\frac{\delta \mathbb{E}}{\delta J} ,$$

can be viewed as a damped Hamiltonian system. More explicitly we have

$$\mathbb{H} = \mathbb{H}_{ext} + \mathbb{H}_{ind} + \frac{1}{J_s} \left[2A\Delta m - K_a(\nabla\varphi) \right].$$

To account for thermal fluctuations we must add a stochastic term:

$$J_t = -\gamma J \times \left(\mathbb{H} - \sqrt{\frac{2\alpha D}{1+\alpha^2}} \mathbb{W}_t \right) - \frac{\alpha\gamma}{J_s} J \times (J \times \mathbb{H}) \quad \text{with} \quad D = \frac{k_B T}{\gamma J_s} , \tag{8.34}$$

where k_B is Boltzmann's constant, T is temperature, and $\mathbb{W}_t$ is white noise in both time and space. After division by J_s we obtain the equivalent form

$$m_t = -\gamma m \times \left(\mathbb{H} - \sqrt{\frac{2\alpha D}{1+\alpha^2}} \mathbb{W}_t \right) - \alpha\gamma m \times (m \times \mathbb{H}). \tag{8.35}$$

Models of this type go back at least 40 years [17]; for numerical studies in the spatially inhomogeneous setting see e.g. [18, 54, 75].

For finite-dimensional damped Hamiltonian systems the effect of thermal noise is well understood. Micromagnetics is infinite-dimensional, so rigorous analysis is more difficult (and presently open), however we expect the situation to be like the finite-dimensional setting. The system should spend most of its time near stable states, with thermally-activated transitions between them. The transitions should moreover have Arrhenius kinetics, i.e. the transition rate between any pair a, b of local minima should have the form

$$k_{ab} = C_{ab} e^{-\Delta E / k_B T} \tag{8.36}$$

where ΔE is the height of the energy barrier and C_{ab} is a suitable prefactor. This formula is applicable when thermal effects are small and transitions rare, i.e. when $\Delta E / k_B T \gg 1$. The minimum-energy saddle separating the two stable states plays the role of a critical nucleus. Once the saddle point is known, the most likely pathway of the transition is easily determined. The prefactor can also be determined, albeit with more difficulty: it depends on the linearization of the energy near the local minimum and the saddle [55].

Rare events are important, but difficult to sample numerically. For example, we expect memory devices to be stable for years, but we can only simulate thermally-activated micromagnetics for a fraction of a second. The Arrhenius formula (8.36) is valuable because it gives access to precisely the regime we cannot sample numerically.

The bottom line is this: to understand thermally induced switching we need (i) a list of stable states, and (ii) a list, for each pair of stable states, of the lowest-energy saddle between them. For small magnetic elements – the numerically accessible regime – the list of stable states is relatively short and easy to determine: it suffices to solve the overdamped zero-temperature dynamics with a variety of initial conditions. Finding the lowest-energy saddle is, however, considerably more subtle.

Recently the problem of evaluating energy barriers and finding the associated saddles has seen considerable progress. The *nudged elastic band method* [63, 71] and the *string method* [45] can be viewed as efficient numerical implementations of the classical "mountain pass method" for finding saddle points. Recently E, Ren, and Vanden-Eijnden applied the string method to analyze the thermally-activated switching of permalloy thin films and cylinders in the absence of an applied magnetic field [46]. One of their examples is a thin film $200nm \times 200nm$ in cross-section and $10nm$ thick. The relevant local minima are C-states and S-states, each of which can be viewed as having a boundary vortex in one corner. The lowest-energy saddle point separating the C and S states turns out to be a flower state, which can be viewed as having a boundary vortex in the middle of one side (see Figure 1 of [46]). The string method is currently being applied to finite-temperature hysteresis diagrams, and to predicting the temperature-dependence of the coercive field [86].

9 Appendix on magnetostatics

We collect here a few results on magnetostatics. Existence and uniqueness of h_{ind} satisfying

$$h_{ind} = -\nabla U \tag{9.1}$$

and

$$\int_{\mathbb{R}^3} h_{ind} \cdot \nabla\varphi = -\int_\Omega m \cdot \nabla\varphi, \quad \forall \varphi \in C_0^\infty(\mathbb{R}^3), \tag{9.2}$$

follow from the Riesz representation theorem. Let

$$X = \overline{\{\nabla u : u \in C^\infty(\mathbb{R}^3), \nabla u \in L^2(\mathbb{R}^3, \mathbb{R}^3)\}}$$

denote the closure of the space of gradients of smooth functions in the L^2 topology. Then X is a closed subset of $L^2(\mathbb{R}^3,\mathbb{R}^3)$ and h_{ind} is the projection of $-m \in L^2(\mathbb{R}^3,\mathbb{R}^3)$ onto X. The main properties of the map $\mathbb{P}$ associating $h_{ind} = -\mathbb{P}m$ with each m are collected in the next proposition.

Proposition 9.1 *(i) For each $m \in L^2$, there exists a unique $h_{ind} \in X$ satisfying* (9.2)*.*

(ii) The field h_{ind} is characterized as the best approximation of $-m$ within X

$$||-m-h_{ind}||_{L^2} = \min_{h\in X}||-m-h||_{L^2}.$$

(iii) The linear map $\mathbb{P} : -m \to h_{ind}$ is an orthogonal projection. In particular

$$||h_{ind}||_{L^2} = ||\mathbb{P}m||_{L^2} \leq ||m||_{L^2}.$$

Classically the induced field may be written as $h_{ind} = -\nabla\Delta^{-1}\operatorname{div} m$. In Fourier space h_{ind} is obtained by a pointwise projection using the matrix $\xi\otimes\xi/|\xi|^2$, i.e.

$$\mathcal{F}(h_{ind})_i(\xi) = -\frac{\xi_i\xi_j}{|\xi|^2}\mathcal{F}m_j(\xi). \tag{9.3}$$

10 Appendix on Γ-convergence

10.1 Main properties

In this article we frequently study a sequence I^k of energy functionals and we are interested in their limiting behavior as $k\to\infty$. The limit we are looking for is, however, not the usual (pointwise) limit. Rather, we look for a notion of convergence which implies that

minimizers of I^k converge to minimizers of I.

Γ-convergence, introduced in 1974 by DeGiorgi and Franzoni [32, 33], is exactly this notion. We first give the formal definition and review some key properties of Γ-convergence. Then we illustrate the notion in an easy, but interesting one–dimensional problem, in fact a 1d version of the sharp interface problem discussed in Section 7.2. Two standard references for Γ-convergence are [31, 11]. An easier introduction is [14] and short overviews appear e.g in [4, 72].

We consider functionals I^k defined on a complete metric space X (e.g. the space L^2 equipped with the usual distance given by the L^2 norm $d(f,g) = ||f-g||_{L^2}$; there is another metric on L^2 which is compatible with weak convergence, when restricted to bounded sets in L^2). We say that the functional I is the Γ-limit of the sequence I^k if the following two conditions are satisfied

(i) (lower bound) For every sequence $f_k \to f$ we have

$$\liminf_{k\to\infty} I^k(f_k) \geq I(f). \tag{10.1}$$

(ii) (attainment of lower bound/recovery sequence) For every f there exists a sequence g_k such that $g_k \to f$ and

$$\lim_{k\to\infty} I^k(g_k) = I(f). \tag{10.2}$$

Remark 10.1 *We often consider Γ-convergence with respect to a continuous parameter (such as the aspect ratio t) rather than a discrete index k. Strictly speaking, we have $I^t \xrightarrow{\Gamma} I$ as $t \to 0$ if $I^{t_k} \xrightarrow{\Gamma} I$ as $k \to \infty$, for every sequence $t_k \to 0$.*

The main difference with ordinary convergence is that the definition of the limit functional I at f involves not only the values of I^k at the point f, but also in a neighborhood of f. This is crucial for the link between Γ-convergence and the convergence of minimizers. The following result (which follows essentially directly from properties (i) and (ii) above) makes this precise.

Theorem 10.2 *Suppose that I is the Γ-limit of the sequence I^k. Let f_k be minimizers of I^k.*

(i) If $f_k \to f$ then f is a minimizer of I.

(ii) If g is a minimizer of I then there exists a sequence g_k of minimizers of I^k such that g_k converges to g.

Remark 10.3 *Various refinements are possible. First, in (i) it suffices that a subsequence f_{k_j} of the sequence f_k converges to f. Convergence of a subsequence can often be assured under rather general 'soft' conditions on the functionals I^k, which does not require detailed knowledge of the minimizers. Second, it suffices that the f_k are approximate minimizers of I^k, i.e. $I^k(f_k) <$*

$I^k(h) + 1/k$ for all $h \in X$. Then the limit f of (a subsequence) is still a minimizer of I. This is particularly useful if we do not know whether I^k has a minimizer. In that case we still have a slightly weaker version of part (ii) of the theorem, stating there exists g_k converging to g which are approximate minimizers in the above sense.

In applications we are often interested in applying additional external fields. This amounts to adding an additional (usually linear) functional h to the energy functional. The operation is compatible with Γ-convergence as long as h is continuous.

Proposition 10.4 *Suppose that h is a continuous functional on X (with respect to the given metric) and*

$$I^k \xrightarrow{\Gamma} I. \tag{10.3}$$

Then

$$I^k + h \xrightarrow{\Gamma} I + h. \tag{10.4}$$

10.2 An example

To illustrate the concept of Γ-convergence consider scalar functions f defined on the unit interval $(0,1)$ and the functionals

$$I^k = \int_0^1 \frac{1}{k}|f'(x)|^2 + k\varphi(f(x))\,dx, \tag{10.5}$$

where φ is a double well potential, with $\varphi(\pm 1) = 0$ and $\varphi > 0$ otherwise. One can take e.g.

$$\varphi(s) = (s^2 - 1)^2.$$

We will see shortly that the Γ-limit functional will 'live' mostly on non-smooth functions f. For this reason it is convenient to extend I^k to a space X which is as large as possible by making it $+\infty$ outside its natural domain of definition. Note that such an extension does not change the minimizers of I^k. We may take $X = L^1(0,1)$ (with the metric given by the usual L^1 norm) and set

$$I^k(f) = \begin{cases} \int_0^1 \frac{1}{k}|f'(x)|^2 + k\varphi(f(x))\,dx, & \text{if } f \text{ is smooth,} \\ +\infty & \text{else.} \end{cases} \tag{10.6}$$

(We could also define $I^k(f)$ by the integral expression for a larger class of f, e.g. for all f whose (distributional) derivative belong to L^2. One can show that this leads to the same Γ- limit.)

What is the Γ-limit of I^k as $k \to \infty$? The second term in the integral suggests that the Γ-limit will only be finite on functions which take only the values ±1. Let f be a function which takes only values ±1 (and is not identical 1 or -1). If we approximate f (in L^1) by smooth functions then the derivatives of the approximations f_k must become very large at some points as we improve the approximation. The more jumps between -1 and 1 the function f makes, the larger we expect the energy $I^k(f_k)$ to be. The Γ-convergence result of Modica and Mortola makes this precise.

Proposition 10.5 *The functionals I^k are Γ-convergent to I where*

$$I(f) = \begin{cases} A_0 \cdot \textit{(number of jumps of } f\textit{)}, & \textit{if } f(x) = \pm 1 \textit{ for all } x \\ +\infty & \textit{else,} \end{cases} \tag{10.7}$$

where

$$A_0 = 2 \int_{-1}^{1} \varphi^{1/2}(t)\, dt.$$

This result illustrates that Γ-convergence is very different from pointwise convergence. In fact, the functionals I^k are finite on smooth functions, while I is $+\infty$ on smooth functions (except for the function which is identically 1 or identically -1). On the other hand, I is finite on functions which take only the values ±1, while I^k is $+\infty$ on those functions (again with the trivial exceptions).

It is instructive to verify Proposition 10.5 using the definition of Γ-convergence. To keep things simple we only consider a function f which has exactly one jump, say $f(x) = -1$ for $x < x_0$, while $f(x) = 1$ for $x > x_0$. To establish the lower bound in the definition of Γ-convergence we follow Modica and Mortola and apply the arithmetic-geometric mean inequality to the integrand of I^k

$$\frac{1}{k}|f'(x)|^2 + k\varphi(f(x)) \geq 2|\varphi^{1/2}(f(x))f'(x)| \tag{10.8}$$

and we observe that the expression inside the absolute value can be written as a total derivative $\frac{d}{dx}H(f(x))$, where

$$H(s) = \int_0^s \varphi^{1/2}(\sigma)\, d\sigma$$

is the anti derivative of $\varphi^{1/2}$.

Now consider a sequence f_k which converges to f in L^1. Then for almost all values of x we have $f^k(x) \to f(x)$ (more precisely this is true for a subsequence, and this is enough to verify (10.1)). Choose $a < x_0 < b$ such that convergence holds at a and b. Then

$$\begin{aligned} I^k(f_k) &\geq \int_a^b 2\left|\frac{d}{dx}H(f_k(x))\right| dx \geq 2\left[H(f_k(b)) - H(f_k(a))\right] \\ &\to 2\left[H(1) - H(-1)\right] = 2A = I(f). \end{aligned}$$

This finishes the verification of condition (i) of Γ-convergence.

To check condition (ii) we need to construct a sequence g_k which approximates the jump function f and does not 'waste' energy. In particular, we should choose g_k such that the geometric-arithmetic inequality (10.8) becomes sharp. This is the case if $g_k'(x) = k\varphi^{1/2}g_k(x)$. We define an optimal profile h as the solution of

$$h'(\xi) = \varphi^{1/2}(h(\xi)), \quad \lim_{\xi \to \pm\infty} h(\xi) = \pm 1, \quad h(0) = 0.$$

Then we can take $g_k(x) = h(k(x - x_0))$ and we see easily that $I^k(g_k) \to 2A = I(f)$. This finishes the proof of Proposition 10.5 for the case that f makes a single jump. If f has multiple jumps at $x_1, x_2, \ldots$ then for the lower bound one simply applies the previous argument with points $a_1 < x_1 < b_1$, $a_2 = b_1 < x_2 < b_2$, etc. For the upper bound one first constructs good local approximations near each x_i as above and then interpolates between these approximations (see e.g [4, 72] for further details).

What can we learn about the minimizers of I^k from the Γ-convergence result ? The (global) minimizers of I^k are actually quite boring, they are given by the two functions f which are identically 1 or identically -1. Already a slight modification of I^k, however, leads to a rather interesting situation. We simply prescribe the average value of f to prevent the trivial solution and to force f to switch from one well to the other. Specifically fix λ (strictly) between -1 and 1 and set

$$J^k(f) = \begin{cases} I^k(f) & \text{if } \int_0^1 f = \lambda, \\ +\infty & \text{else.} \end{cases} \tag{10.9}$$

Then, by the same arguments as above, one can show that the functionals J^k have a Γ-limit J, which agrees with I if the constraint is satisfied and is $+\infty$ otherwise. The minimization problem for J is very easy to solve. We need to have at least one jump to satisfy the constraint. More jumps cost additional energy. Hence J has exactly two minimizers, f_+ and f_-, each of which have exactly one jump (at $1/2 \pm \lambda/2$, respectively).

The Γ-convergence result and Theorem 10.2 imply that all minimizers of J^k must converge to either f_+ or f_- (after choosing a subsequence).

10.3 Hierarchies of Γ-limits

Γ-convergence reveals limiting features of a family of functionals at a certain energy scale. By using different rescalings one can extract different features of the family of functionals (we have seen that, e.g. in Section 4.3). This fact can also be easily illustrated using the example discussed in the last subsection. If we considered the differently scaled functionals

$$\tilde{I}^k = \int_0^1 \frac{1}{k^2}|f'(x)|^2 + \varphi(f(x))\,dx, \tag{10.10}$$

then it is not difficult to show that $\tilde{I}^k \xrightarrow{\Gamma} \tilde{I}$ where

$$\tilde{I}(f) = \int_0^1 \varphi^{**}(f(x))\,dx, \tag{10.11}$$

where φ^{**} is the convex envelope of φ and where we consider Γ-convergence with respect to weak convergence in L^2. As long as φ grows super linearly at ∞ its convex envelope vanishes exactly on the convex hull of the energy wells, i.e. the set $[-1, 1]$. The set of minimizers of $\tilde{I}$ is very degenerate. Every function taking values in $[-1, 1]$ is a minimizer. The Γ-limit of the rescaled functionals $I^k = k\tilde{I}^k$ helps to break this degeneracy. Only functions that take only the values ± 1 have finite energy and the limit functional distinguishes among these by the number of jumps.

Acknowledgments

We would like to thank Rudi Schäfer for the very fruitful collaboration over the last six years. Much of ADS' work was carried out at the Max Planck Institute for Mathematics in the Sciences, Leipzig, where he was leader of a junior research group between 1998 and 2003. ADS and SM were supported by the DFG priority programme SPP 1095 "Analysis, modelling and simulation of multiscale problems". RVK was supported by NSF through grants DMS-0101439 and DMS-0313744. FO was supported by the DFG research center SFB 611 "Singular phenomena and scaling in mathematical models" at the University of Bonn. We thank Rubén Cantero-Álvarez, Jörg

Drwenski, Hans Knüpfer, Thomas Roessler and Jutta Steiner for their most valuable help.

Appendix: Frequently used symbols

Symbol	Meaning	First appearance
$\mathbb{E}$	micromagnetic energy (in J)	(2.1)
J	magnetization (in Tesla)	(2.1)
J_s	saturation magnetization	(2.2)
m	normalized magnetization J/J_s	(2.3)
A	exchange stiffness (in J/m)	(2.1)
K_a	crystalline anisotropy constant (in J/m^3)	(2.1)
φ	anisotropy function	(2.1)
$\mathbb{H}_{ind}$	magnetic field induced by J (in A/m)	(2.1)
$\mathbb{U}$	potential of $\mathbb{H}_{ind}$	(2.6)
μ_0	vacuum permeability $4\pi \times 10^{-7}$ Vs/Am	(2.5)
Ω	region occupied by ferromagnetic body	(2.1)
$C_0^\infty(\mathbb{R}^3)$	space of smooth functions	
	which vanish outside a compact set	(2.9)
$\mathcal{K}$	easy magnetization directions	(2.10)
K_d	magnetostatic energy density $J_s^2/2\mu_0$	(2.13)
E	normalized energy $\mathbb{E}/K_d$ (units of volume)	(2.14)
H_{ext}	normalized applied field $\mu_0\mathbb{H}_{ext}/J_s$	(2.15)
H_{ind}	normalized induced field	(2.16)
U	potential of H_{ind}	(2.15)
Q	quality factor K_a/K_d	(2.18)
$d = d_{BL}$	Bloch–line width $\sqrt{A/K_d}$	(2.19)
I	$\mathbb{E}/K_a = E/Q$	(2.22)
d_{BW}	Bloch–wall width $\sqrt{A/K_a} = d/\sqrt{Q}$	(2.24)

Symbol	Meaning	First appearance
t	thickness of a prism–shaped film	Section 3
t	time	Section 8.2 only
l	typical lateral dimension of a film	Section 3
τ	aspect ratio t/l	(3.1)
Ω'	two–dimensional base of a film	(3.2)
e	fully nondimensional energy $e = E/(l^2t)$	(3.4)
ω	rescaled (nondimensional) three–dimensional domain	(3.3)
ω'	rescaled two–dimensional domain	(3.3)
κ	rescaled Bloch–line length $\kappa = d/l$	(3.5)
u	rescaled potential	(3.6)
h_{ind}, h_{ext}	rescaled fields	(3.7), (3.8)
D_ω	demagnetizing tensor	(3.11)
φ^{**}	convex envelope of φ	(3.13)
x'	tangential coordinates $x' = (x_1, x_2)$	(4.3)
∇'	in–plane gradient (∂_1, ∂_2)	(4.3)
$\mathcal{F}$	Fourier transform	(4.4), (6.14)
m'	in–plane magnetization $m' = (m_1, m_2)$	(4.5)
V	single layer potential	(4.7)
e^τ	nondimensionsonal two–dimensional energy as	
	a function of the aspect ratio τ	Section 4.2
$\tilde{h}'$	scaled applied field	(5.5)
v	rescaled single layer potential	(5.9)
$\nabla'^{\perp}$	rotated gradient $(-\partial_2, \partial_1)$	(5.22)
$C_0^\infty(\Omega; \mathbb{R}^3)$	space of smooth vectorfields	
	vanishing outside a compact subset of Ω	(7.3)
$i_{\varepsilon,Q}, i_\varepsilon$	rescaled energy functionals	(7.12), (7.15)
$\mathrm{Per}_\Omega E$	perimeter of a set E	Proposition 7.4
$\mathrm{BV}(\Omega)$	functions of bounded variation	Proposition 7.4
T	absolute temperature	Section 8.2
γ	gyromagnetic ratio	Section 8.2
α	damping factor in LLG equations	Section 8.2
$\mathbb{W}$	white noise	Section 8.2
k_B	Boltzmann's constant	Section 8.2

References

[1] A. Aharoni, *Introduction to the Theory of Ferromagnetism*, Oxford Univ. Press, 2nd ed. 2000.

[2] A. Aharoni, Magnetization curling, *Phys. stat. sol.* **16** (1966), 1–42.

[3] A. Aharoni and S. Shtrikman, Magnetization curve of the infinite cylinder, *Phys. Rev.* **109** (1958), 1522–1528.

[4] G. Alberti, Variational models for phase transitions, an approach via Γ-convergence, in : *Calculus of variations and partial differential equations (Pisa, 1996)* (eds. G. Buttazzo et al.), Springer, 2000, pp. 95–114.

[5] G. Alberti and S. Müller, Two-scale Young measures for variational problems with multiple scales, *Comm. Pure Appl. Math* **54** (2001), 761–825.

[6] F. Alouges, S. Conti, A. DeSimone, and Y. Pokern, Energetics and switching of quasi-uniform states in small ferromagnetic particles, *M^2AN Math. Model. Numer. Anal.* **38** (2004), 235–248.

[7] F. Alouges, T. Rivière, S. Serfaty, Néel and cross-tie wall energies for planar magnetic configurations, *ESAIM Control Optim. Calc. Var.* **8** (2002), 31–68.

[8] L. Ambrosio, C. De Lellis and C. Mantegazza, Line energies for gradient vector fields in the plane. *Calc. Var. PDE*, **9** (1999), 327–355.

[9] L. Ambrosio, N. Fusco and D. Pallara, *Functions of bounded variation and free discontinuity problems*, Oxford Univ. Press, 2000.

[10] G. Anzellotti, S. Baldo and A. Visintin, Asymptotic behavior of the Landau-Lifshitz model of ferromagnetism, *Appl. Math. Optim.* **23** (1991), 171–192.

[11] H. Attouch, *Variational convergence for functions and operators*, Pitman, 1984.

[12] J.M. Ball, A. Taheri and M. Winter, Local minimizers in micromagnetics and related problems, *Calc. Var.* **14** (2002), 1–27.

[13] F. Bethuel, H. Brezis and F. Hélein, *Ginzburg-Landau Vortices*, Birkhäuser, Basel 1994.

[14] A. Braides, Γ-*convergence for beginners*, Oxford Univ. Press, 2002.

[15] H. Brezis, J.M. Coron, E.H. Lieb, Harmonic maps with defects, *Comm. Math. Phys.* **107** (1986), 649–705.

[16] W.F. Brown, Criterion for uniform micromagnetization, *Phys. Rev.* **105** (1957), 1479–1482.

[17] W.F. Brown, Thermal fluctuations of a single-domain particle, *Phys. Rev.* **130** (1963), 1677–1686.

[18] G. Brown, M.A. Novotny, and P.A. Rikvold, Langevin simulation of thermally activated magnetization reversal in nanoscale pillars, *Phys. Rev. B* **64** (2001), 134422.

[19] P. Bryant and H. Suhl, Thin–film magnetic patterns in an external field, *Appl. Phys. Lett.*, **54** (22) (1989), 2224–2226.

[20] R. Cantero-Álvarez and F. Otto, Critical Fields in Ferromagnetic Thin Films: Identification of Four Regimes, *SFB 611 Preprint* **128** (2004), see http://www-mathphys.iam.uni-bonn.de, *J. Nonlinear Science*, in press

[21] R. Cantero-Álvarez and F. Otto, Oscillatory buckling mode in thin-film nucleation, *SFB 611 Preprint* **148** (2004), see http://www-mathphys.iam.uni-bonn.de, *J. Nonlinear Science*, in press

[22] R. Cantero-Álvarez and F. Otto, The concertina pattern in ferromagnetic thin-film elements: A supercritical bifurcation, *SFB 611 Preprint* **227**, (2005), see http://www-mathphys.iam.uni-bonn.de

[23] G. Carbou, Regularity for critical points of a nonlocal energy, *Calc. Var.* **5** (1997), 409–433.

[24] G. Carbou, Thin layers in micromagnetism, *Math. Models Methods Appl. Sci.* **11** (2001), 1529–1546.

[25] G. Carbou, P. Fabrie, Regular solutions for Landau-Lifshitz equation in a bounded domain, *Diff. Int. Eqns.* **14** (2001), 213–229.

[26] G. Carbou, P. Fabrie and O. Guès, Couche limites dans un modèle de ferromagnétisme, *Comm. Partial Differential Equations* **27** (2002), 1467–1495.

[27] C. Carstensen, D. Praetorius, Effective simulation of a macroscopic model for stationary micromagnetics, *Comput. Methods Appl. Mech. Engrg.* **194** (2005), no. 2-5, 531–548

[28] Choksi, R., Kohn, R. V., Bounds on the micromagnetic energy of a uniaxial ferromagnet, *Comm. Pure Appl. Math* **51** (1998), 259–289

[29] R. Choksi, R.V. Kohn and F. Otto, Domain branching in uniaxial ferromagnets: a scaling law for the minimum energy, *Comm. Math. Phys.* **201** (1999), 61–79.

[30] S. Conti, Branched microstructures: scaling and asymptotic self-similarity, *Comm. Pure Appl. Math.* **53 (11)** (2000), pp. 1448–1474

[31] G. Dal Maso, *An introduction to* Γ*-convergence*, Birkhäuser, 1993.

[32] E. De Giorgi, Sulla convergenza di alcune successioni di integrali del tipo dell'area, *Rend. Mat.* **8** (1975), 277–294.

[33] E. De Giorgi and T. Franzoni, Su un tipo di convergenza variazionale, *Atti Accad. Naz. Lincei Rend. Cl. Sci. Fis. Mat. Natur.* **82** (1975), 842–850.

[34] A. DeSimone, Energy minimizers for large ferromagnetic bodies, *Arch. Ration. Mech. Anal.* **125** (1993), 99–143.

[35] A. DeSimone, Hysteresis and imperfection sensitivity in small ferromagnetic particles, *Meccanica* **30** (1995), 591–603.

[36] A. DeSimone, J. McCord, F. Otto, R. Schäfer, *in preparation*

[37] A. DeSimone, R.V. Kohn, S. Müller and F. Otto, A compactness result in the gradient theory of phase transitions. *Proc. Roy. Soc. Edinburgh* **131A** (2001), 833–844.

[38] A. DeSimone, R.V. Kohn, S. Müller and F. Otto and R. Schäfer, A reduced theory for thin film micromagnetics, *Comm. Pure Appl. Math.* **55** (2002), 1408–1460.

[39] A. DeSimone, R.V. Kohn, S. Müller and F. Otto, Repulsive interaction of Néel walls, and the internal length scale of the cross–tie wall, *Multiscale Model. Simul.* **1** (2003), 57–104.

[40] A. DeSimone, R.V. Kohn, S. Müller, F. Otto and R. Schäfer, Two-dimesional modelling of soft ferromagnetic films, *Proc. Roy. Soc. A* **457** (2001), 2983–2991.

[41] A. DeSimone, R.V. Kohn, S. Müller, F. Otto and R. Schäfer, Low energy domain patterns in soft ferromagnetic films, *J. Magnetism Magn. Mat.* **242-245** (2002), 1047–1051.

[42] A. DeSimone, H. Knüpfer and F. Otto, 2-d stability of the Néel wall, *SFB 611 Preprint* **224** (2005)

[43] W. Döring, Mikromagnetismus, in: *Handbook of Physics* (ed. S. Flügge) *Vol. 18/2, Ferromagnetism*, Springer, 1966, pp. 341–437.

[44] J. Drwenski, F. Otto, $\mathcal{H}^2$–matrix methods vs. FFT in thin–film stray–field computations, *SFB Preprint* **161** (2004), see http://www-mathphys.iam.uni-bonn.de

[45] W. E, W. Ren and E. Vanden-Eijnden, String method for the study of rare events, *Phys. Rev. B* **66** (2002), 052301.

[46] W. E, W. Ren and E. Vanden-Eijnden, Energy landscape and thermally activated switching of submicron-size ferromagnetic elements, *J. Appl. Phys.* **93** (2003), 2275–2282.

[47] L.C. Evans, Partial regularity of stationary harmonic maps, *Arch. Ration. Mech. Anal.* **116** (1991), 101–113.

[48] L.C. Evans and R.F. Gariepy, *Measure theory and fine properties of functions*, CRC Press, 1992.

[49] I. Fonseca and G. Leoni, Relaxation results in micromagnetics, *Ricerche di Matematica* **XLIX** (2000), 269–304.

[50] H. Forster, T. Schrefl, R. Dittrich, W.Scholz and H. Fidler, Fast Boundary Methods for Computing Demagnetizing Fields, *IEEE Trans. Magn.* **39** (5) (2003), 2513–2515.

[51] E.H. Frei, S. Shtrikman and D. Treves, Critical size and nucleation field of ideal ferromagnetic particles, *Phys. Rev.* **107** (1957), 446–455.

[52] C.J. Garcia–Cervera, *Magnetic domains and magnetic domain walls*, PhD thesis, New York University, 1999.

[53] C.J. Garcia–Cervera, One–dimensional magnetic domain walls, *Europ. J. Appl. Math.* **15** (2004), 451–486.

[54] J.L. Garcia-Palacios and F.J. Lazaro, Langevin-dynamics study of the dynamical properties of small magnetic particles, *Phys. Rev. B* **58** (1998), 14937–14958.

[55] C.W. Gardiner, *Handbook of Stochastic Methods for Physics, Chemistry, and the Natural Sciences*, Springer, 3rd edition, 2004.

[56] G. Gioia and R.D. James, Micromagnetics of very thin films, *Proc. Roy. Soc. London Ser. A* **453** (1997), 213–223.

[57] E. Giusti, *Minimal surfaces and functions of bounded variations*, Birkhäuser, 1984.

[58] W. Hackbusch, A sparse matrix arithmetic based on $\mathcal{H}$–matrices, I, Introduction to $\mathcal{H}$-matrices, *Computing*, **62(2)** (1999), 89–108.

[59] W. Hackbusch, S. Börm, $\mathcal{H}^2$–matrix approximation of integral operators by interpolation, *Appl. Numer. Math.*, **43(1-2)** (2002), 129–143, 19th Dundee Biennial Conference on Numerical Analysis (2001).

[60] R. Hardt and D. Kinderlehrer, Some regularity results in ferromagnetism, *Comm. Partial Differential Equations* **25** (2000), 1235–1258.

[61] F. Hélein, Régularité des applications faiblement harmoniques entre une surface et une sphère, *C.R. Acad. Sci. Paris Ser. I* **311** (1990), 519–524.

[62] F. Hélein, *Harmonic maps, conservation laws and moving frames*, Diderot, 1997.

[63] G. Henkelman and H. Jonsson, Improved tangent estimate in the nudged elastic band method for finding minimum energy paths and saddle points, *J. Chem. Phys.* **113** (2000), 9978–9985.

[64] A. Hubert, Zur Theorie der zweiphasigen Domänenstrukturen in Supraleitern und Ferromagneten. *Phys. Stat. Solidi* **24** (1967), 669–682 (*On the theory of two-phase domain structures in superconductors and ferromagnets*).

[65] A. Hubert, Stray–field–free magnetization configurations, *Phys. Status Solidi* **32** (1969), 519–534.

[66] A. Hubert and R. Schäfer, *Magnetic domains*, Springer, 1998.

[67] P.E. Jabin and B. Perthame, Compactness in Ginzburg–Landau energy by kinetic averaging, *Comm. Pure Appl. Math.* **54** (2001), 1096–1109.

[68] P.E. Jabin, B. Perthame and F. Otto, Line–energy Ginzburg–Landau models: zero–energy states, *Ann. Sc. Norm. Super. Pisa Cl. Sci. (5)* **1** (2002), 187–202.

[69] R.D. James and D. Kinderlehrer, Frustration in ferromagnetic materials, *Continuum Mech. Thermodyn.* **2** (1991), 215–239.

[70] W. Jin and R. V. Kohn, Singular perturbation and the energy of folds *J. Nonlinear Sci.* **10** (2000), 355–390.

[71] H. Jonsson, G. Mills and K.W. Jacobsen, Nudged elastic band method for finding minimum energy paths of transitions, in: *Classical and Quantum Dynamics in Condensed Phase Simulations* (eds. B.J. Berne, G. Ciccotti, and D.F. Coker), World Scientific, 1998.

[72] J. Jost and X. Li-Jost, *Calculus of variations*, Cambridge Univ. Press, 1998.

[73] M. Kléman, Soft ferromagnets revisited, *Phase Transitions* **30** (1991), 217–232.

[74] J. Ko, *The construction of a partially regular solution to the Landau-Lifshitz-Gilbert equation in* $\mathbb{R}^2$, submitted to *Nonlinearity*

[75] R.H. Koch, G. Grinstein, G.A. Keefe, Y. Lu, P.L. Trouilloud, W.J. Gallagher and S.S.P. Parkin, Thermally assisted magnetization reversal in submicron-sized magnetic thin films, *Phys. Rev. Lett.* **84** (2000), 5419–5422.

[76] R.V. Kohn, S. Müller, Branching of twins near an austenite twinned–martensite interface, *Phil. Mag. A* **66** (1992), pp. 697–715.

[77] R.V. Kohn, S. Müller, Surface energy and microstructure in coherent phase transitions, *Comm. Pure Appl. Math.* **47** (1994), pp. 405–435.

[78] R.V. Kohn, F. Otto, M.G. Reznikoff and E. Vanden-Eijnden, Action minimization and sharp interface limits for the stochastic Allen Cahn equation, submitted to *Comm. Pure Appl. Math.*

[79] R.V. Kohn, M.G. Reznikoff and E. Vanden-Eijnden, Micromagnetics at finite temperature and large deviation theory, *J. Nonlinear Science*, in press.

[80] R.V. Kohn and V. Slastikov, Another thin film limit of micromagnetics, *Arch. Ration. Mech. Anal.*, in press.

[81] M. Kurzke, Boundary vortices in thin magnetic films, *Calc. Var. PDE*, in press.

[82] A.E. LaBonte, Two–dimensional Bloch–type domain walls in ferromagnetic films, *J. Appl. Phys* **40** (1969), 2450–2458.

[83] L.D. Landau and E. Lifshitz, On the theory of the dispersion of magnetic permeability in ferromagnetic bodies, *Phys. Z. Sowjetunion* **8** (1935), 153–169.

[84] E. Lifshitz, On the magnetic structure of iron, *J. Phys. USSR* **8** (1944), 337–346.

[85] F.H. Lin, A remark on the map $x/|x|$, *C.R. Acad. Sci. Paris Ser. I* **305** (1987), 529–531.

[86] D. Liu, C. J. Garcia–Cervera and W. E, Magnetic switching of thin films under thermal perturbation, *J. Appl. Phys.*, in press

[87] H. McGahagan, An approximation scheme for Schrödinger maps, preprint.

[88] C. Melcher, *Néel walls and regularity in thin film micromagnetics*, PhD thesis, University of Leipzig, 2002.

[89] C. Melcher, The logarithmic tail of Néel walls in thin films, *Arch. Ration. Mech. Anal.* **168** (2003), 83–113.

[90] C.Melcher, Logarithmic lower bounds for Néel walls, *Calc. Var.* **21** (2004), 209–219.

[91] S. Middelhoek, Domain walls in thin Ni–Fe films, *J. Applied Phys.* **34** **(4)** (1963), pp. 1054–1059.

[92] L. Modica, The gradient theory of phase transitions and the minimal interface criterion, *Arch. Ration. Mech. Anal.* **98** (1987), 123–142.

[93] L. Modica and S. Mortola, Un esempio di Γ-convergenza, *Boll. Un. Mat. Ital.* **14** (1977), 285–299.

[94] R. Moser, Ginzburg-Landau vortices for thin magnetic films, *AMRX Appl. Math. Res. Express* **1** (2003), 1–32.

[95] R. Moser, Boundary vortices for thin ferromagnetic films, *Arch. Ration. Mech. Anal.* **174** (2004), 267–300

[96] L. Néel, Les lois de l'aimantation et de la subdivision en domaines elementaires d'un monocristal de fer I–III, *J. Phys. Rad.* **5** (1944), 241–251 and 265–276.

[97] A.J. Newell and R.T. Merrill, Single-domain critical sizes for coercivity and remanence, *J. Geophys. Res.-Sol. Ea.* **104** (B1) (1999), 617–628.

[98] F. Otto, Cross-over in scaling laws: a simple example from micromagnetics. *Proceedings of the International Congress of Mathematicians, Vol. III (Beijing, 2002)*, 829–838, Beijing, 2002. Higher Ed. Press.

[99] P. Pedregal, Relaxation in ferromagnetism: the rigid case, *J. Nonlinear Sci.* **4** (1994), 105–125.

[100] L.A. Privorotskii, *Thermodynamics of domain structures*, Wiley, 1976.

[101] R. Riedel and A. Seeger, Micromagnetic treatment of Néel walls, *Phys. Stat. Sol. (B)* **46** (1971), 377–384.

[102] T. Rivière, Everywhere discontinuous harmonic maps into spheres, *Acta Math.* **175** (1995), 197–226.

[103] T. Rivière and S. Serfaty, Limiting domain wall energy for a problem related to micromagnetics, *Comm. Pure Appl. Math.* **54** (3) (2001), 294–338.

[104] T. Rivière and S. Serfaty, Compactness, kinetic formulation, and entropies for a problem related to micromagnetics, *Comm. Partial Differential Equations* **28** (2003), 249–269.

[105] R. Schoen and K. Uhlenbeck, A regularity theory for harmonic maps, *J. Diff. Geom.* **17** (1982), 307–355.

[106] L. Simon, *Theorems on regularity and singularity of energy minimizing maps*, Lecture Notes in Mathematics ETH Zürich, Birkhäuser, 1996.

[107] J.A. Sethian, *Level Set Methods*, Cambridge University Press, 1996.

[108] E.C. Stoner and E.P. Wohlfarth, A mechanism of magnetic hysteresis in heterogeneous alloys, *Phil. Trans. Roy. Soc. London* **A240** (1948), 599–642.

[109] M. Struwe, On the asymptotic behaviour of the Ginzburg-Landau model in two dimensions, *Diff. Int. Eqns* **7** (1994), 1613–1624.

[110] M. Struwe, Erratum: On the asymptotic behaviour of the Ginzburg-Landau model in two dimensions, *Diff. Int. Eqns* **8** (1995), 224.

[111] L.Tartar, On mathematical tools for studying partial differential equations of continuum physics: H-measures and Young measures, in: *Developments in Partial Differential Equations and Applications to Mathematical Physics* (eds. G. Buttazzo, G.P. Galdi and L. Zanghirati), Plenum Press, 1992.

[112] L. Tartar, Beyond Young measures, *Meccanica* **30** (1995), 505–526.

[113] H.A.M. van den Berg, Self–consistent domain theory in soft–ferromagnetic media. II, Basic domain structures in thin film objects, *J. Appl. Phys.* **60** (1986), 1104–1113.

[114] R.J. Vanderbei, *Linear programming: foundations and extensions*, Kluwer, 1996.

[115] A. Visintin, On Landau–Lifshitz' equations for ferromagnetism, *Jap. J. Appl. Math.* **2** (1985), 69–84.